REFRACTIVE INDEX ENHANCEMENT AND
ATOMIC STATE LOCALIZATION IN RUBIDIUM

BY

NICHOLAS A. PROITE

A DISSERTATION SUBMITTED IN PARTIAL FULFILLMENT OF

THE REQUIREMENTS FOR THE DEGREE OF

DOCTOR OF PHILOSOPHY

(PHYSICS)

AT THE

UNIVERSITY OF WISCONSIN–MADISON

2011

ACKNOWLEDGMENTS

These last several years at UW-Madison have been phenomenal and much of that is due to my advisor Deniz Yavuz. He has been an inspiring teacher and scientist to work with throughout my graduate career and his research skill is remarkable both in and out of the lab. His amazing ability to break down even the most difficult problems into simple equations governed by basic concepts has taught me a new way to look at scientific problems. Additionally, at times when others (like me) would find it easy to be cynical, such as after a research setback that demands a change in direction, he is guided by the simple mantra to "do the best physics possible." This type of leadership and enthusiasm has set up an environment that I looked forward to working and learning in everyday. Just as important is the impact that Deniz has had on me that goes far beyond physics, through our many conversations on literature and philosophy and more throughout the years.

I would also like to thank Mark Saffman and Thad Walker for taking me on as an undergraduate assistant in their lab many years ago. Much of what made me a successful graduate student I learned in the basement of Sterling Hall working for them on the rubidium quantum computing project. I consider it a privilege to have worked there with graduate students Todd Johnson and Erich Urban, who are two of the most capable scientists I have ever seen. Todd in particular exemplified that pretty much any single problem can be solved in less time than it takes to walk to Chipotle, with nothing more than a wallet-sized card of fundamental constants and a few choice guesses. It was equally a privilege to work with Pasad Kulatunga who taught me an huge amount of physics, along with some lessons about life that can't be repeated here.

ii

As a graduate student, many people helped us expediently set up a lab and begin taking results within our first year together. Brett Unks, Tyler Green, and J. P. Sheehan all put in huge amounts of time and effort to get our lab and experiments set up. Much of what is found in this thesis would not have been possible were it not for them. And even though Tyler beat me to the finish line by a few weeks, it has been an honor being his colleague all these years. His aptitude for electronics, lasers and colorful language has made it a pleasure to work together. Additionally, Daniel Sikes has had a big impact on our lab by helping to uncover the rich set of physics that stems from our refractive index enhancement scheme. It's humbling to know that the experiments described here may just be the cornerstone for much greater things.

Thanks also to Zach Simmons and Josh Weber for showing a huge amount of dedication to our labs. Zach was instrumental in our work on atom localization. Their hard work leaves me no doubt that Tyler and I are leaving the labs in good hands.

I also thank everyone in Mark Saffman's and Thad Walker's labs for exchanging equipment and advice over the years. It's these types of interactions that make a linear expansion of the UW AMO group, such as the start of the Yavuz lab, into an exponential growth in the quality of the program. I hope we were able to contribute to everyone else's research in kind. In particular I thank Bob Wyllie for the many times he helped me with various research problems.

Overall, graduate school at Wisconsin has been a wonderful experience. I've come to know everyone in my class well and it will be difficult to see them head their separate ways. In particular, I thank Mike Anderson, Ryan Gavin and Christie Simmons for making much of graduate school, from classes to quals, from research to teaching, much more fulfilling and enjoyable.

Lastly, I thank my family for their patience in the long hours I spent as a child taking apart electronic toys or reprogramming our family computer. To some extent, not much has changed except that I now get paid to do these things. Throughout college and graduate school, my parents along with my wife Sarah's parents have never been anything less than 100% supportive of my seemingly endless pursuit of more education. I am extremely grateful to be surrounded by such people. Sarah's encouragement never faltered, even when I had to work odd hours throughout the years to finish problem sets or take data. Not only did she brew coffee in the morning and cook

countless dinners at night for the both of us, she somehow found time to earn an MD all the while. She's the most amazing person I know.

DISCARD THIS PAGE

TABLE OF CONTENTS

vi

Appendix

LIST OF FIGURES

Appendix
Figure   Page

ABSTRACT

It is well known that the resolution of a traditional optical imaging system is limited by the wavelength of light. This is the co-called diffraction limit and overcoming this barrier has been the subject of intense theoretical and experimental research. At its basis, the diffraction limit stipulates that light cannot be focused to a waist narrower than half its wavelength. In this thesis, we explore two approaches to overcoming this barrier in the context of resolving an object. First, we describe a scheme which enhances the index of refraction of a medium to a very large value. This effectively reduces the wavelength of a laser beam inside the medium. The essential idea is to excite two Raman resonances with appropriately chosen strong control lasers. We experimentally demonstrate this idea with a set of lasers propagating through a hot vapor cell of rubidium. Additionally, we report an experimental demonstration of Raman self-focusing and self-defocusing in a far-off resonant scheme. The key idea is to drive the hyperfine transition rubidium to a maximally coherent state with two laser beams. In this regime, the two-photon detuning from the Raman resonance controls the nonlinear index of the medium. We find good agreement between numerical simulations and experimental results. Next, we outline and demonstrate the basic concepts of a type of scanning fluorescence microscope that is capable of resolving nanometer-size objects in the far field. The key idea is to use a spatially varying laser beam to set up an atomic dark state with sensitive position dependence. This localizes the atomic excitation of a gas to a spot much smaller

than a diffraction limited optical waist. We experimentally demonstrate the first steps towards subwavelength resolution in an ultracold cloud of rubidium.

Chapter 1

Introduction

Arguably, the imaging problem is one of the most important problems in the physical sciences. How can we optically image a very small object? It is well known that the resolution of a traditional optical imaging system is limited by the wavelength of light. This is the so-called diffraction limit and overcoming this barrier has been the subject of intense theoretical and experimental research. Discovered in the 19th century as a result of Maxwell's equations, the limit simply states that light of wavelength λ is unable to resolve spatial features smaller than $\lambda/2$. Recently, it was found that one can beat this resolution limit by utilizing the nonlinear response of a medium. In this thesis, we explore two such approaches to solving this problem. One approach involves enhancing the index of refraction of a medium to a very large value. This reduces the effective wavelength of the probing laser, $\lambda = \lambda_0/n$, where λ_0 is the free-space wavelength and n is the refractive index. A large refractive index, therefore, corresponds to a reduced wavelength inside the medium and enhanced imaging resolution. A second approach involves preparing a medium such that its response depends nonlinearly on the spatial distribution of the intensity of a laser beam. We predict and demonstrate that the entire spatial extent of an atomic excitation can then occur on a sub-diffraction-limit scale.

Before describing these approaches in detail, we take a broader look at the field of nonlinear optics. Both approaches described here take their inspiration from the recent explosion of nonlinear optics experiments. This growth can mostly be connected to new and exciting discoveries in the way atoms interact with light. Two decades ago, it was found that the absorption profile of an atom can be completely eliminated inside a narrow frequency band simply by driving the atom at two cleverly chosen frequencies. This technique, known as electromagnetically induced transparency (EIT), occurs when the excited state probability amplitudes from the two lasers destructively interfere [1, 2]. The advent of EIT brought with it a completely new array optical phenomena, such as slow light [3–5], fast and backward light [6, 7], and enhanced nonlinearities [8–10] to name just a few. While some of these effects had been studied earlier, never were they so dramatic or readily accessible. Moreover, a new generation of scientists was inspired to think about novel ways to engineer the dispersive and absorptive properties of a gas using quantum interference, with and without EIT. One example of this is manipulating the dispersion of a gas to provide an enhanced index of refraction without absorbing laser light of a particular frequency.

In chapters 2 - 6, we ask, what is the highest index of refraction that can be achieved in a vapor? A laser beam tuned close to an atomic resonance can experience a large refractive index. As an example, the refractive index for a gas at a pressure of 1 torr can reach values as high as 10. However, such a large index is usually accompanied by large absorption and the effect is not useful. This is because, near an optical resonance, the real and imaginary parts of the optical susceptibility are of the same order. In these chapters, we suggest a new scheme that will enhance the index of refraction while maintaining vanishing absorption. It has been predicted [11] and demonstrated [12] that by using EIT, it is possible to obtain a large index of refraction, ideally with vanishing absorption. However, this interference is obtained very close to an atomic resonance and with substantial excited state fraction as a result. In this thesis, we extend this idea to a far-off resonant atomic system [13]. We experimentally demonstrate that the refractive index of a probe beam, which is very far detuned from an optical resonance, can be enhanced while maintaining vanishing absorption. We describe this effect in more detail in chapter 2 and then we present a proof-of-principle demonstration.

In chapters 7 and 8 we outline and demonstrate the basic concepts of a type of scanning fluorescence microscope that is capable of resolving nanometer-size objects in the far field. It has been suggested and experimentally demonstrated that sub-wavelength position localization of atoms can be obtained by using spatially varying energy shifts [14–16]. If a very small object is embedded into an atomic medium, sub-wavelength atom localization can be used to obtain a shadow image of the object. In chapter 7 we suggest a new approach that utilizes the intensity dependent excitation of EIT. The key idea is to localize the atomic excitation of atoms to a spot much smaller than a diffraction limited optical waist by using a laser beam with a particular spatial pattern. In chapter 8, we experimentally demonstrate the principles behind this idea and observe an improvement in imaging resolution.

Both of these unique approaches contribute to a growing body of research that aims to attack the imaging problem. As we will discuss later, the approaches described here also bring with them a broad array of potential applications and interesting physics that goes far and beyond the imaging problem. Not only do they add new tools to the field of nonlinear optics, but they also serve as the foundation for a rich set of applications such as subwavelength qubit addressing, all-optical mirrors, and forming negative index materials

$\sim\!\sim\!\sim\!\sim$

The structure of this thesis is as follows:

Chapter 2 introduces the idea of refractive index enhancement in both the weak and strong fields. We describe how, using two-photon resonances, a system can be set up which enhances the refractive index at a particular frequency while maintaining unity transmission. We outline the formalism and highlight key theoretical results, such as how this scheme can be optimized to achieve the maximum 2-level, resonantly-enhanced index of refraction.

Chapter 3 describes our experimental apparatus and provides technical results. We set up an optical apparatus which provides 1 Watt of light in each of two beams that are separated in frequency by several gigahertz. The mutual stability of these beams is better than one part in a billion, making this scheme ideal for the experiments described in this thesis.

Chapter 4 presents our experimental demonstration of the basic principle behind the index enhancement scheme. Here, we use a hot vapor cell containing rubidium and run the experiment simultaneously using both common isotopes. We observe an enhanced index in the vapor cell with vanishing absorption.

Chapter 5 discusses various improvements to the index enhancement experiment. We start by improving the optical pumping scheme and also describing how we simplify the overall scheme to a single isotope of rubidium. We then make technical changes which allow us to run the experiment at a higher density. These changes result in a much higher refractive index enhancement. We conclude with preliminary results that show hyperfine-level optical pumping at extremely high densities, the first steps towards achieving even better refractive index enhancement.

Chapter 6 presents experimental results of Raman self-focusing and self-defocusing. Using two strong laser beams tuned 100 Doppler linewidths from the excited state, we show preparation of rubidium in maximal coherence (equal populations of the ground states). The result is an intensity-dependent index of refraction. We observe self-focusing and de-focusing, the first steps towards observing optical solitons in a vapor.

Chapter 7 proposes a new type of nanoscale resolution microscope that can beat the diffraction limit. The key idea is to use the dark state of EIT with a spatially-varying coupling beam to access atoms at the nanoscale. We numerically simulate idea in a alkali-metal system and find that its preparation is robust against typical experimental perturbations. We predict that this scheme should be scalable to the subwavelength spatial scales.

Chapter 8 experimentally demonstrates the key idea of the microscope chapter proposed in the previous chapter. We start with a rubidium magneto-optical trap and a standing-wave EIT coupling beam. We then localize an atomic state to the coupling beam nodes. The localization due to the spatial nonlinearity of EIT enhances the resolution by a factor of two.

Chapter 9 suggests a new type of all-optical switch. This chapter can be seen as an independent idea from the rest of the thesis. In our suggestion, a probe beam propagating alone travels through

an atomic vapor with minimal interaction. When in the presence of a "switch beam," the probe-atom interaction is modified such that the probe phase is inverted. The suggestion is among the simplest possible switches, and requires a merely 1000 photons in the switch beam.

Chapter 2

An overview of refractive index enhancement

2.1 Introduction and background

Since the birth of quantum and nonlinear optics, one of the key challenges has been if one can achieve a very large refractive index for a laser beam [17]. As already mentioned, a key application of a large refractive index is to optical imaging science. Another important application of a large refractive index is to optical lithography where the smallest feature size of a lithographic mask is determined by the wavelength of light. A simple and an efficient way to achieve a large refractive index is likely to have significant practical implications since lithographic resolution currently determines the size and the processing power of every semiconductor integrated circuit.

It was first pointed out by Scully that, by using interference in a three state atomic system, it is possible to obtain a large refractive index with negligible absorption [11, 18]. The pioneering work of Scully was extended to different configurations by Fleischhauer and colleagues [19–21]. Although these ideas were experimentally demonstrated in a Rb vapor cell by Zibrov *et al.* [22], it has not yet been possible to achieve a refractive index in a vapor that is large enough to be of practical importance. This chapter describes a new approach to this long-standing problem [13]. By utilizing the interference of two Raman resonances, we show that the refractive index of a laser

beam that is very far detuned from an electronic resonance can be enhanced while maintaining vanishing absorption.

In recent years, a number of counter-intuitive effects in driven atomic systems have been predicted and demonstrated [1–10, 23–25]. Broadly, most of these effects can be thought as engineering the variation (the slope) of the refractive index as a function of frequency. In contrast, our technique allows us to engineer the actual value of the refractive index while maintaining vanishing absorption to the beam. In this sense, our approach complements the existing techniques in modifying the optical response of an atomic medium.

Before describing in detail our main idea, we first would like to summarize the well known results for a usual two level system. When a laser beam is tuned close to an optical resonance of a two level atom, the real and imaginary parts of the linear susceptibility take the following usual form:

$$\chi'(\omega) = \frac{\mu^2 N}{\hbar \epsilon_0} \frac{\Delta \omega}{\Delta \omega^2 + \Gamma^2}, \tag{2.1}$$

$$\chi''(\omega) = \frac{\mu^2 N}{\hbar \epsilon_0} \frac{\Gamma}{\Delta \omega^2 + \Gamma^2}. \tag{2.2}$$

Here $\Delta \omega$ is the detuning of the laser beam from the transition, μ is the matrix element and Γ is the decay rate. The index of refraction is related to the real part of the susceptibility through the relation $n = \sqrt{1 + \chi'}$. The real part of the susceptibility and hence the index of refraction, obtains its maximum value for $\Delta \omega = \Gamma$. This maximum value is

$$\chi'_{max} = \frac{\mu^2 N}{\hbar \epsilon_0} \frac{1}{2\Gamma}. \tag{2.3}$$

Although χ'_{max} can be quite large for an atomic vapor cell, this effect is not useful since the imaginary part of the susceptibility is just as large. Remarkably, as will be detailed in the following paragraphs, by using our scheme, one can obtain the maximum susceptibility of Eq. 2.3 with vanishing imaginary part of the susceptibility, i. e. absorption.

Figure 2.1 The interference of an absorptive resonance and an amplifying resonance can lead to an enhanced refractive index with vanishing absorption. (a) shows the most straightforward way to achieve such an interference. Due to various difficulties, the scheme in (a) is not practical (see text for details). (b) shows an equivalent scheme that we experimentally demonstrate in this work. With an atom starting in the ground state $|g\rangle$, a Raman transition involves absorption of one photon and emission of another photon of different frequency such that the two-photon resonance condition is satisfied. By changing the order at which the probe laser, E_p, is involved in the process, such a Raman resonance can be made absorptive or amplifying. (c) shows the real part, χ', and the imaginary part of the susceptibility, χ'', as a function of frequency. Here, we take the two resonances to be of equal strength with a width of 0.1 MHz and assume the spacing between resonances to be 0.2 MHz.

2.2 Refractive index enhancement scheme

The refractive index enhancement scheme we use here was first suggested by Yavuz [13] and was recently extended to high alkali densities by Kocharovskaya and colleagues [26]. The essential features of this idea are presented in Fig. 2.1. It is well-known that, the interference of the dipole moments of an absorptive resonance and an amplifying resonance can lead to an enhanced
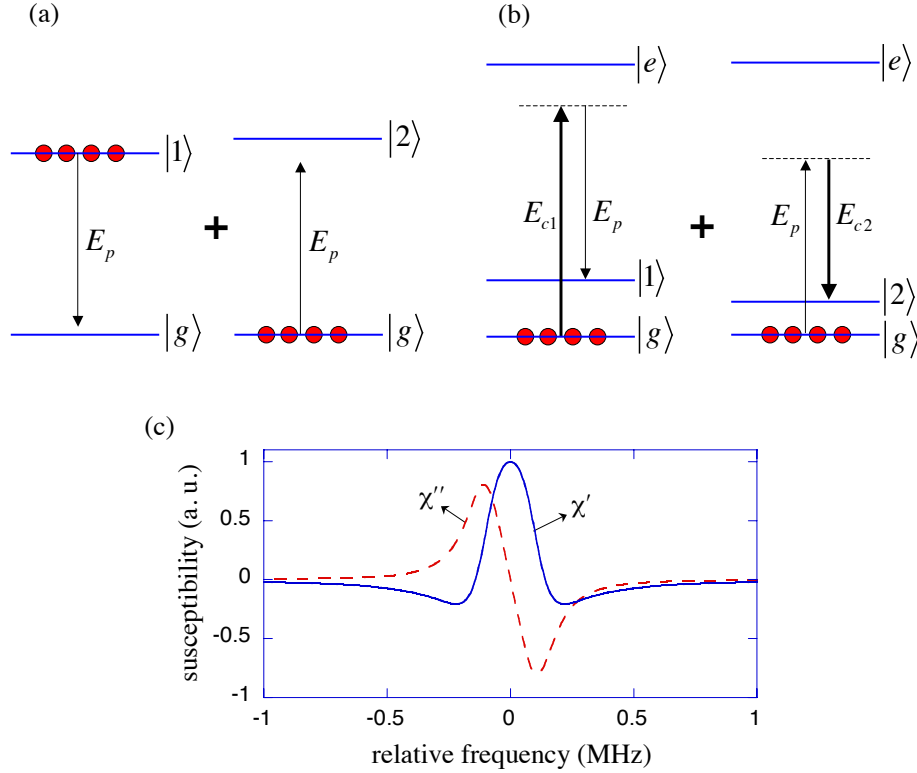
refractive index with vanishing absorption [19]. As shown in Fig. 2.1(a), the most straightforward way to realize such an interference would be to have two different two-level atomic species. In practice, such a multiple two-level atom scheme has not yet been realized since it is difficult to find two different atomic species with very close and easily tunable resonance frequencies. The key idea that we suggest here is that such a multiple two-level scheme can be realized by using Raman resonances in far-off resonant atomic systems. As shown in Fig. 2.1(b), with an atom starting in the ground state $|g\rangle$, a Raman transition involves absorption of one photon and emission of another photon of different frequency such that the two-photon resonance condition is satisfied. By changing the order at which the probe laser, E_p, is involved in the process, such a Raman resonance can be made absorptive or amplifying. This approach circumvents the difficulties of the scheme of Fig. 2.1(a). The two Raman transition frequencies can be arbitrarily different since we have the freedom to choose the frequencies of the control lasers, E_{c1} and E_{c2}.

Figure 2.2 demonstrates the result of arbitrarily setting the frequency of the control lasers. The real part of the susceptibility, χ', and therefore the refractive index, peaks at the point of vanishing imaginary part, χ''. Figures 2.2(a) and 2.2(b) demonstrate that the resonances positioned too far apart in frequency provide only slightly enhanced index at the point of vanishing absorption. In Fig. 2.2(c), the resonances are situated one linewidth from each other and the index enhancement is maximized.

We proceed with a detailed description of the scheme, closely following the suggestion by Yavuz [13]. Using the formalism of Harris and colleagues [27–29] we take the two-photon detunings from the Raman resonances as $\delta\omega_1 = (\omega_1 - \omega_g) - (\omega_{c1} - \omega_p)$ and $\delta\omega_2 = (\omega_2 - \omega_g) - (\omega_p - \omega_{c2})$. The quantities Γ_e, γ_1, and γ_2 denote the (amplitude) decay rates of states $|e\rangle$, $|1\rangle$, and $|2\rangle$ respectively. The perturbative solution of this atomic evolution with the assumption that most of the population stays in the ground state gives the following steady-state susceptibility for the probe wave [13]:

$$\chi = \frac{2\hbar N}{\epsilon_0}\left(a \quad + \quad \frac{|b_1|^2}{2[\delta\omega_1 - j(\gamma_1 + \mathfrak{J}(d_1)|E_{c1}|^2)]}|E_{c1}|^2 \right.$$
$$\left. + \quad \frac{|b_2|^2}{2[\delta\omega_2 + j(\gamma_2 + \mathfrak{J}(d_2)|E_{c2}|^2)]}|E_{c2}|^2 \right) \tag{2.4}$$
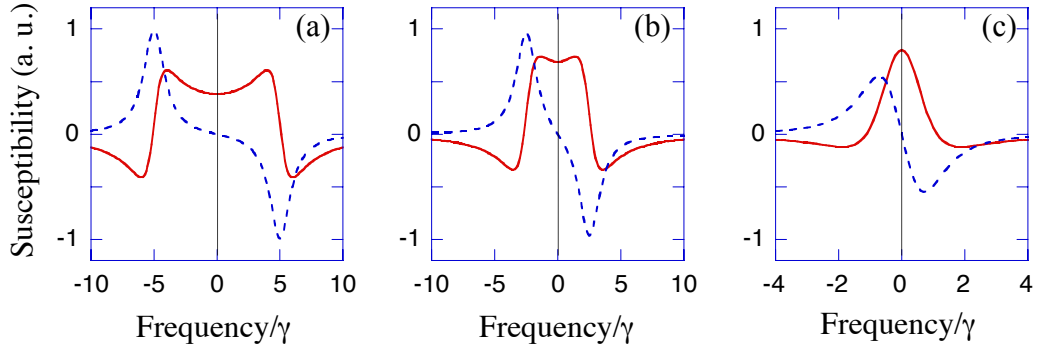
Figure 2.2 The real part, χ' (solid line) and the imaginary part, χ'' (dashed line) of the susceptibility of the probe laser for $\Delta = 10\gamma$, 5γ, and γ, for (a), (b), and (c) respectively. At the midpoint between the resonances, there is destructive interference in the imaginary part of the susceptibility. Conversely, the real part of the susceptibility obtains a large value due to constructive interference. As a result, the beam experiences an enhanced refractive index with vanishing absorption.

Eq. 2.4 is motivated in more detail in appendix chapter B. The constants a, b_1, and b_2 involve the matrix elements between respective states and also detunings of the laser beams from the excited state $|e\rangle$. The quantities $\mathfrak{J}(d_1)|E_{c1}|^2$ and $\mathfrak{J}(d_2)|E_{c2}|^2$ are the optical pumping rates of the states due to the strong control lasers. The first term on the right hand side of Eq. 2.4 is the background Lorentzian susceptibility that would be present even in the absence of the strong control fields. Since we are in the far-detuned regime, we will neglect this term. The second term is due to the two-photon resonance with the upper Raman state $|1\rangle$ and causes probe gain. The third term is due to the to-photon resonance with state $|2\rangle$ and causes probe absorption. The two resonances occur when the probe laser wavelength is chosen such that $\omega_p = \omega_g + \omega_{c1} - \omega_1$ ($\delta\omega_1 = 0$) or $\omega_p = \omega_2 + \omega_{c2} - \omega_g$ ($\delta\omega_2 = 0$) respectively. We define the quantity $\Delta \equiv (\omega_1 + \omega_2 - 2\omega_g) - (\omega_{c1} - \omega_{c2})$ that determines the separation of these two resonances in frequency space. This equation can also be rewritten in terms of the two-photon detunings, $\Delta = \delta\omega_1 + \delta\omega_2$.

We now ask, what is the maximum index that may be achieved while maintaining vanishing absorption? We assume the Raman resonances have an optimal separation of $\Delta = \gamma$. The index can then be enhanced by turning up the control beam intensities until the beams are strong enough that they simply broaden the resonances. Setting $E_{c1} = E_{c2}$, and also setting all of the isotopes'

strengths, detunings, and linewidths equal to each other, we find the real part of Eq. 2.4 to be

$$\chi' = \frac{2\hbar N}{\epsilon_0} \frac{|b_1|^2(\Delta/2)}{\{(\Delta/2)^2 + [\gamma_1 + \mathfrak{J}(d_1)|E_{c1}|^2]^2\}} |E_{c1}|^2. \tag{2.5}$$

The maximum attainable refractive index can be found by differentiating Eq. 2.5 with respect to $|E_c|^2$ and finding what value of $|E_c|^2$ maximizes χ'. The result is that the control beam intensities should be set to $|E_c|^2 = \gamma_1^2 + (\Delta/2)^2$. Plugging this in, and setting $\Delta = \gamma_1$, we find [13]

$$\chi' \simeq \frac{N}{\hbar\epsilon_0} \frac{|\mu_{ge}|^2}{2\Gamma_e}. \tag{2.6}$$

This key result is nearly identical to Eq. 2.1. We find that the maximum index experienced by a probe beam in the Raman scheme is the same as a probe tuned to the resonance of a two-level system. The key difference here is, of course, that absorption is eliminated.

Plugging in numbers for the experiment to be presented in the following chapters, we can find how much power we need for maximal index. We use Raman resonances of width $\gamma = 2\pi \times 200$ kHz, single-photon detuning of $2\pi \times 16$ GHz, excited state linewidth of $\Gamma = 2\pi \times 300$ MHz, and beam waist W = 1.2 mm, we require 0.5 Watts of optical power in the control beams to achieve the maximum attainable index of refraction. As will be discussed shortly, this power requirement is more or less met with our optical apparatus.

While the refractive index corresponds linearly with density, there are practical limits that place an upper limit on the achievable index. In a warm vapor, the maximum refractive index occurs at a density of about 10^{15} atoms/cm^3 is ≈ 2. The collisional broadening of the excited state prevents the refractive index to be increased further [26]. This is discussed in more detail in chapter 5.

2.3   Strong field limit: self-focusing and spatial Raman solitons

We now consider a situation where the refractive index of two lasers is modified in the strong-field limit. As mentioned earlier, using an appropriately phased Raman coherence, one can render a medium transparent to a resonant laser beam with the technique of EIT. For nonlinear mixing processes, the concept of maximum atomic coherence is particularly important [30, 31]. In resonant, EIT-like systems, a maximally coherent state is adiabatically prepared using a counter-intuitive

pulse timing sequence. In far-off resonant atomic systems, which is the case here, preparation is achieved with two laser beams whose frequency difference is slightly detuned from the frequency of the two-photon Raman transition. One important application of Raman self-focusing is to the field of spatial optical solitons. It has recently been predicted that, under appropriate conditions, diffraction may be balanced by Raman self-focusing and as a result two-frequency optical solitons are formed [32–34]. In alkali vapor cells, the formation of these solitons, termed spatial Raman solitons, require low optical power (≈ 100 mW) that is readily achievable with continuous-wave (CW) lasers. Due to operating near maximum coherence, $\rho \approx 1/2$, these solitons are stable in full three spatial dimensions. Numerical simulations of these solitons predict well-defined soliton-soliton collision properties and reveal many rich nonlinear dynamics [34]. Spatial Raman solitons in alkali vapor cells may also find possible practical applications in areas such as all-optical information processing [35, 36].

Prior work in self-focusing generally uses high-peak power, Q-switched pulsed lasers. The Harris group at Stanford has recently demonstrated Raman self-focusing in molecular hydrogen (H_2) [37]. Self-focusing in a resonant, three level Λ scheme under the conditions of EIT was observed by Moseley and colleagues [38, 39]. Optical wave-guiding in a V scheme by using strong optical pumping was demonstrated by Truscott et $al.$ [40]. There has been substantial theoretical work on Electromagnetically Induced Focusing in a variety of near-resonance, multi-frequency systems [40–44]. Raman gain and slow light propagation in far-off resonant ^{85}Rb alkali atoms were recently demonstrated by Deng and colleagues [45]. We also note that, since the pioneering work of Ashkin and colleagues [46], a large number of experiments have demonstrated self-trapping and pattern formation of laser beams in atomic vapor cells utilizing inherently-dissipative one-photon resonances [47–49].

2.4 Summary

The refractive index of a substance closely corresponds to its absorption, but we propose a scheme here that eliminates absorption while supplying a huge refractive index. The key idea is

tune a probe far from the atomic resonance, and then set up a scheme of absorptive and amplifying Raman resonances near the probe frequency, closely following the suggestion of Ref. [13].

In the following four chapters, we walk through our proof-of-principle demonstration of this concept. We begin by describing our optical apparatus, and then describe refractive index enhancement in the weak-field and strong field limit.

Chapter 3

Generation of High-Power Laser Light with GHz Splitting[1]

3.1 Introduction

The index enhancement scheme suggested in the previous chapter requires a relatively large amount of laser light split into different frequency components. This is because the transitions between the two hyperfine ground states is dipole forbidden. These transitions are accessed by laser beams whose frequency difference equals the transition frequency in a two-photon Raman configuration. In this chapter we demonstrate the generation of laser beams whose frequencies are separated by the ground state hyperfine transition frequency in ^{87}Rb. The system uses a single master diode laser appropriately shifted by high frequency acousto-optic modulators and amplied by semiconductor tapered ampliers. This produces two 1 W laser beams with a frequency spacing of 6.834 GHz and a relative frequency stability of 1 Hz. Variants of this optical system will be at the heart of all subsequent experimental chapters in this thesis.

The apparatus described here could also be found useful for several other common atomic physics experiments that utilize the alkali-metal hyperfine ground states. Traditionally, these states have been used in atomic clocks that are accurate at the 10^{-15} level [51]. When isolated from the

---

[1]A variation on this chapter can be found at Ref. [50]. See appendix chapter A for additional details.

environment, these states have extremely long decoherence times and therefore are ideal candidates for storing quantum information [52–55].

3.2 Apparatus

Noting Fig. 1, we utilize a configuration of high-frequency acousto-optic modulators (AOMs) and semiconductor tapered amplifiers. We start with a master oscillator, an external cavity diode laser, whose frequency can be precisely tuned and locked via saturated absorption spectroscopy. The output beam of the master oscillator is coupled into a semiconductor tapered amplifier which generates optical power in excess of 1 Watt at the master frequency. This light is then divided between two high frequency AOMs which shift the relative frequencies by 6.834 GHz. The diffracted orders are then coupled into two additional tapered amplifiers. In addition to an order of magnitude power increase, this system has the added benefit of requiring no additional locking mechanisms such as a phased-locked loop (PLL) based approach.

Before proceeding with a detailed description of our scheme, we would like to summarize existing experimental designs for generating laser light with gigahertz frequency separations. Microwave modulation of the laser current [54–56] and electro-optic modulation [57, 58] put sidebands on the laser and filter out the center frequency with a cavity. The PLL approach synchronizes the output of a low noise local oscillator laser and an inexpensive diode laser [59, 60]. Previously low frequency AOMs have been used to achieve gigahertz shifts in a sextuple pass configuration [61]. Optical powers of up to 40 mW have been achieved by seeding the shifted output beams of the above processes into a diode laser in a slave configuration [56, 61]. Alternatively, several Ti:sapphire based PLL designs have several hundred milliwatts of power in the local oscillator beam, but low power in the phase locked beam [59, 60].
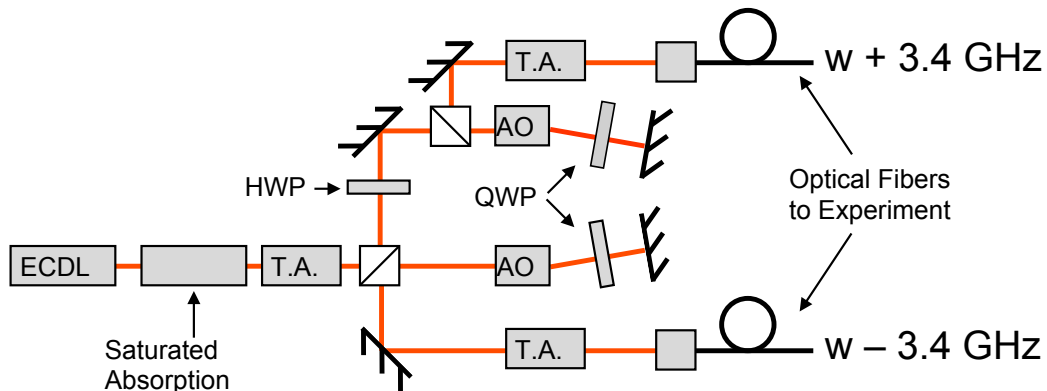
Figure 3.1 Block diagram of the apparatus. Light generated by a single MO is amplified by an TA up to 1 W of optical power. This light is divided between two AOMs that shift the laser frequencies by a total of 6.834 GHz and have a diffraction efficiency of 1.3%. The shifted beams are then re-amplified by two additional TAs, giving 1 W of optical power in each frequency component. This light is then coupled into a single mode fiber. Abbreviations: MO (Master Oscillator), TA (Tapered Amplifier), AOM (Acousto Optic Modulator), QWP (Quarter Wave Plate), HWP (Half Wave Plate)

3.3   Component Design and Performance

Master Oscillator

The design of our external cavity diode laser (ECDL) closely follows the design of Arnold et al. [62] with modifications by Hawthorn *et. al.*[63]. We use a Sharp laser diode (GH0781JA2C) which provides high output power and low cost, but sacrifices tunability. Temperature and current control are provided via commercial Newport 325B and 505B drivers. An extensive review of this design can be found in previous publications [62–64]. Here, we report a mode hop free tuning of 5 GHz, a sub-MHz linewidth, and an output power of 50 mW at 105 mA of operating current. We find this design to be exceptionally stable over months of operation, as it has maintained its absolute frequency with no mechanical adjustments.

Tapered Amplifiers

Our optical system employs three identical tapered amplifiers (TAs). The TAs are based on the Eagleyard EYP-TPA-0780-01000 semiconductor tapered amplifier. The housing is based on the

design of Nyman [64] with modifications made to the lens handling system and the base plate. The amplifier chip is positioned in a three piece Oxygen-free high conductivity (OFHC) copper block assembly which acts as the TA anode connection and provides structural stability and thermal dissipation. The copper blocks are threaded to accept custom designed lens mounts which allow positioning of the collimating optics to a few microns precision. This amplifier housing is mounted on a thermo-electric cooler (TEC) which is in turn mounted on an aluminum base. The base houses the electrical connections, provides mechanical stability and raises the output beam to the required height. A plexiglas enclosure fitted with optical windows isolates the amplifier from the environment, protecting the chip from dust and humidity. We find the mechanical stability of this design to be excellent, requiring minimal realignment over several months of use.

The diode current and temperature stabilization are provided by off the shelf drivers (Newport 325B and 525B). The temperature is PID feedback stabilized with a monitor thermistor positioned as close to the amplifier chip as possible. We find that the heat generated by the amplifier does not exceed 3 Watts and can be handled with a single TEC and no water cooling, provided the system is in good thermal contact with the base and table.

Performance of tapered amplifiers in TA configurations has been covered in great detail in the literature [64, 65]. We note that the devices are strongly dependent on the polarization of the source light, and recommend positioning a half-wave plate immediately upstream to maximize the output. We report that given careful alignment, 2 mW of source light is sufficient to attain 1.0 W of output, +27dB gain. Of this, 80 mW is broadband amplified spontaneous emission (ASE). Even after subtracting the ASE, our recorded gain greatly exceeds the +13 dB of gain specified by the manufacturer. Beam shaping of the output is accomplished using a single 50 mm cylindrical lens positioned after a collimating lens. This gives a 3:2 mm elliptical beam. The input power is well below the saturation limit for these devices, so no top hat structure is seen in the output (Fig. 2). After the cylindrical lens, the beam is passed through an optical isolator. We find that the amplifiers are very sensitive to back reflections as the waveguide structure at the input facet is very fragile. With mode matching, greater than 60% of the amplified light can be coupled into a single mode, polarization maintaining fiber.
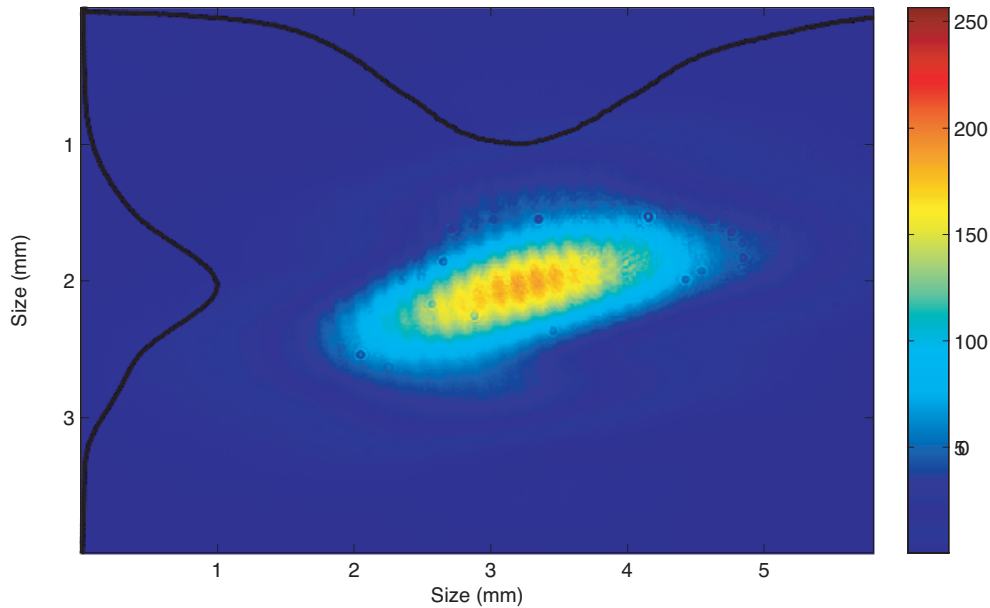
Figure 3.2 Intensity profile of the TA output beam after correction with a single cylindrical lens and a 2:1 telescope. Greater than 600 mW of this 1 W beam can be coupled into a single mode fiber. The striped pattern is a result of interference on the profiling CCD, and the small speckles are dust particles.

Frequency Shifters

Once the master oscillator beam is amplified, it is then split into three beams (Fig. 1). Two of these are sent to the frequency shifters, while the third can be fiber coupled and used in experiments which require an additional beam [54].

The required frequency shift, 6.834 GHz, is accomplished by shifting each of the two beams with high speed AOMs. These devices have a center frequency of 1.7 GHz, a bandwidth of 150 MHz, and high power optical coatings (Brimrose TEF-1700-150-780). The AOMs work in a parallel, double passed, configuration. One beam is shifted up 3.4 GHz using the $+1^{st}$ order and the other beam is shifted down 3.4 GHz using the -1st order. The 1 Watt of input RF for each AOM are provided by independently operating HP 6593 function generators supported by a Miteq AMF series amplifier.

At each AOM, the input beam is focused down to a 60 μm waist with a 125 mm lens. Alignment into the AOM crystal is controlled with a five axis translation stage and optimized by maximizing the diffracted power. The diffracted beam then passes through a collimating lens and a quarter wave plate before being retro-reflected back into the crystal. The final, doubly shifted beam is separated from the input via a polarizing beam cube. It should be noted that, given the large Bragg angle associated with the high frequency of these devices, a portion of the beam will reflect off the transducer. Care must be taken during alignment to disentangle this unshifted portion from the shifted light. A series of razor blades reduces this contamination to below 0.1% of the final amplified beam.

Low diffraction efficiency of the frequency shifter is the primary motivation for initially amplifying the MO. We achieve maximum single pass efficiencies of 13% with the polarization parallel to the transducer. When the polarization is perpendicular to the transducer, the maximum attained efficiency drops to 10%. In a double pass configuration, this implies a total efficiency of 1.3%. Thus, supplying 200 mW of optical power to each AOM provides enough light to sufficiently seed the TA.

This system is designed to be flexible. For example, if we wish to attain the required frequency splitting for ^{85}Rb experiments, light from the $+1^{st}$ order high frequency AOM provides one beam as above. The second beam is passed through a separate, low frequency, AOM to achieve the required net splitting of 3.035 GHz.

The optical heterodyne spectrum between the two output beams is shown in Figure 3. We perform this beam beating experiment by combining the two beams with a polarizing beam cube, passing the resultant beam through a polarizer and then fiber coupling the light to a high speed detector (Advanced Optical Components HFD6180-413). The microwave signal is then mixed down to 30 MHz to permit Hertz level analysis. The main figure shows the beat note with a 1 kHz span. The inset figure shows the same signal on a 11 Hz span. We measure a FWHM of 1 Hz from the inset data and posit that this is an upper limit defined by the resolution of our spectrum analyzer (HP 8560E).
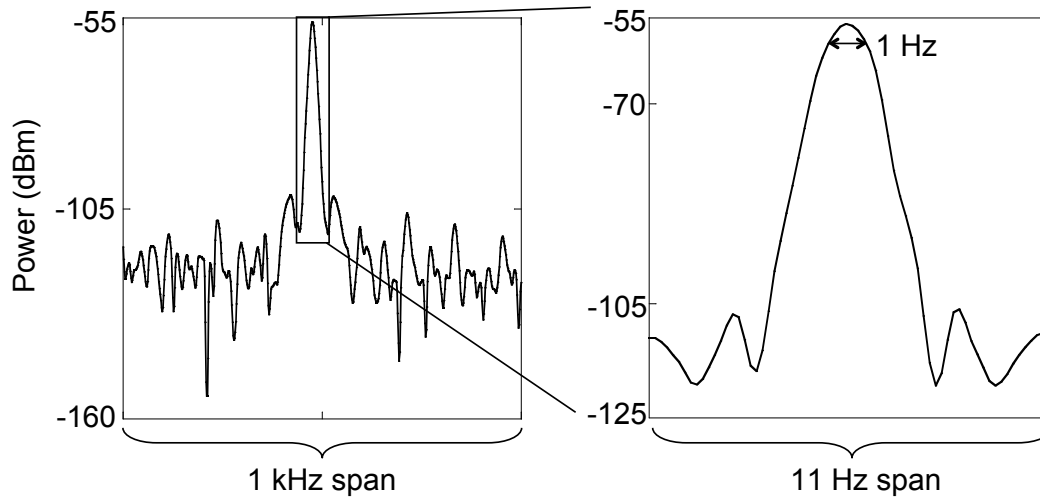
Figure 3.3 Beam beating experiment. The two output beams from the apparatus are combined via a beam cube and polarizer. The resultant beam is then incident on a high speed photodiode, through an optical fiber. The displayed center frequency is 6.834 GHz, mixed down to 30 MHz. The span in the main image 1 kHz, while the inset span is 11 Hz. The measured FWHM of the center peak in the inset is 1 Hz, and is limited by the instrument resolution.

3.4   Conclusion

The apparatus presented here is capable of generating high power laser light with GHz splitting. It provides better than an order of magnitude improvement in the available optical power over existing systems. In the following chapters, we will use this system to address ^{87}Rb (6.834 GHz) and ^{85}Rb (3.035 GHz).

In many experiments, the two photon detuning from resonance is scanned to determine the frequency dependence. While the AOMs have a scanning bandwidth of 150 MHz, in a double pass configuration this is reduced by a factor of $\sqrt{2}$. Also, slight shifts in the angle of the output beams from the AOMs reduce coupling into the TAs, further reducing the bandwidth of our overall system. We measure a 3 dB point of 53 MHz. This narrowed bandwidth may be an issue for experiments where large scans of the frequency difference are required.

It is important to note that in situations where the atomic system is very susceptible to small amounts of resonant light (i. e. in a dipole trap), cavity filtering may be required to thoroughly

remove background ASE. We find that, because the ASE is in a different spatial mode, 1% of light coupled into a single mode fiber consists of unwanted frequencies.

Chapter 4

Refractive Index Enhancement with Vanishing Absorption in an Atomic Vapor[1]

4.1   Introduction

In this chapter, we report an experiment where the refractive index of a vapor is enhanced while maintaining vanishing absorption of the beam. This can be seen as a proof-of-concept experiment of the suggestion described in chapter 2. We demonstrate the scheme in two isotopes of atomic rubidium, ^{87}Rb and ^{85}Rb, for the two required Raman resonances.

4.2   Experimental setup

Figure 4.1 shows the simplified experimental set up and the relevant energy level diagrams. We work with a triple layer magnetically shielded and temperature controlled natural abundance Rb (28% ^{87}Rb, 72% ^{85}Rb) vapor cell. The vapor cell is $L = 7.5$ cm long and contains 10 torr of Neon (Ne) as a buffer gas. The temperature of the vapor cell is kept at $T = 90$ degrees Celsius which gives a total atomic density of $N \approx 2.4 \times 10^{12}$ / cm^3. We use $|F = 2\rangle \rightarrow |F = 1\rangle$ and $|F = 2\rangle \rightarrow |F = 3\rangle$ hyperfine transitions in ^{87}Rb and ^{85}Rb respectively (in ground electronic state 5S$_{1/2}$). For Raman transition between the hyperfine states, we utilize far-off resonant excitation

---

[1]A variation of this chapter can be found at Ref. [66]. See appendix chapter B for additional details.

(a)

Rb vapor cell

E_{c1}

E_{c2} E_p

^{87}Rb optical pumping laser

probe beam detection

^{85}Rb optical pumping laser

(b)

$F'{=}0,1,2,\overline{3}$

16 GHz

optical pumping laser

E_p E_{c1}

$F{=}2$

$F{=}1$

^{87}Rb

$F'{=}1,2,\overline{3},4$

optical pumping laser

E_p E_{c2}

$F{=}3$

$F{=}2$

^{85}Rb
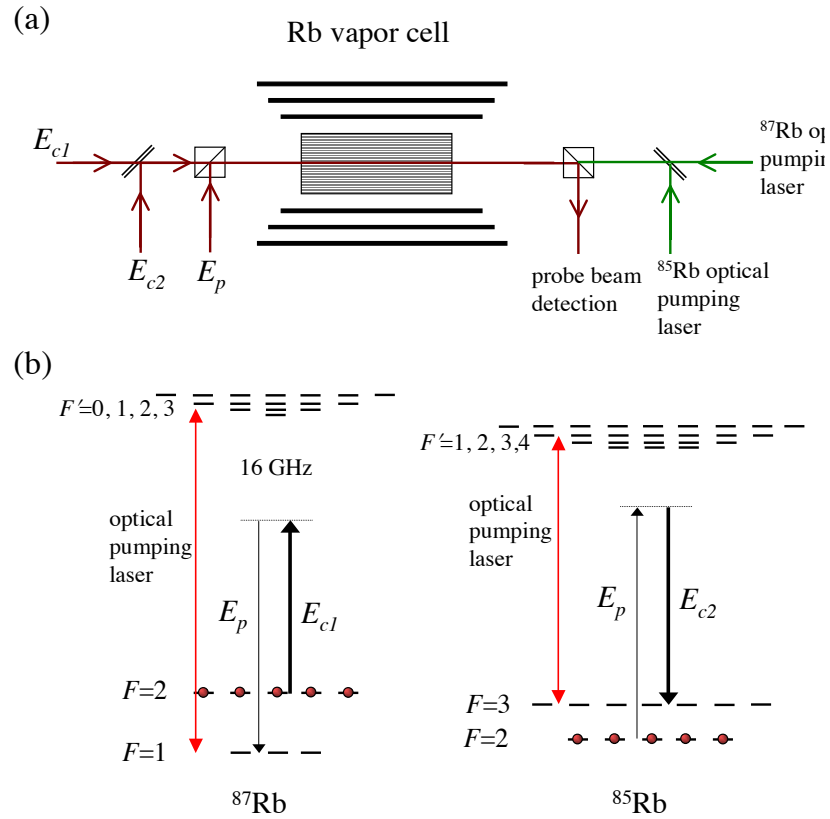
Figure 4.1 Simplified experimental set-up and the energy level diagram (not to scale) for the two isotopes. The experiment is performed in a magnetically shielded, natural abundance Rb vapor cell. Two optical pumping lasers optically pump the two species to the $|F = 2\rangle$ hyperfine state in the ground electronic state. With the atoms optically pumped, three experimental laser beams, E_p, E_{c1}, and E_{c2} drive two Raman transitions, one in each isotope. The interference of these two resonances lead to enhanced refractive index with vanishing absorption. All three laser beams are far-detuned from the single-photon electronic resonance.

through the excited electronic state $5P_{3/2}$ (D2 line) near a wavelength of $\lambda = 780.2$ nm. We drive the two Raman transitions with a weak probe beam, E_p, and two strong control lasers, E_{c1} and E_{c2}. The frequency differences between respective beams are tuned close to hyperfine transition frequencies, $\omega_p - \omega_{c1} \approx 6.834$ GHz and $\omega_p - \omega_{c2} \approx 3.035$ GHz. The frequency of the probe laser beam, ω_p, is detuned ≈ 16 GHz from the D2 line in ^{87}Rb.

We start the experiment by optically pumping both of the atomic species to the $F = 2$ hyperfine state manifold. This is achieved by two optical pumping lasers locked to $|F = 1\rangle \rightarrow |F' = 2\rangle$ transition in ^{87}Rb and $|F = 3\rangle \rightarrow |F' = 3\rangle$ transition in ^{85}Rb respectively. Each optical pumping beam has a power of about 0.5 W and is obtained by seeding a semiconductor tapered amplifier with an external cavity diode laser. The optical pumping beams have a collimated beam radius of ≈ 3 mm and counter-propagate the three experimental beams as shown in Fig. 4.1(a).

The three experimental beams, E_p, E_{c1}, and E_{c2}, are derived from a single external cavity master diode laser, using a setup very similar to that of Fig. 3.1 of the previous chapter. The key difference is that here a third high-frequency AOM is needed to get the required frequency separation between beams. After the AOMs, the control beams are amplified by tapered amplifiers to achieve the required power levels. The frequency of each of the three laser beams can be tuned by changing the modulation frequency of the AOMs. This set-up gives us complete control over the position of the two Raman resonances when we scan the frequency of the probe laser beam. The polarization of the probe beam is linear and orthogonal to the polarization of the two control laser beams. The three beams have a collimated beam waist of $W_0 = 1.2$ mm at the vapor cell. The probe laser has an optical power of about 1 mW and is much weaker when compared with the control lasers (≈ 100 mW each).

We run the experiment in a timing cycle where we optically pump the atoms for about 500 μs. We then turn-off the optical pumping beams and turn-on the probe and the control lasers. To avoid undesired time-dynamics due to sharp edges, we turn-on the three beams smoothly over about 10 μs and perform our measurements at the peak of the pulses. After the beams exit the vapor cell, we separate the weak probe beam with a high-extinction polarizer. To determine the gain or the loss on the probe beam, we measure the intensity of the beam at the peak of its spatial profile right after it leaves the vapor cell.

4.3 Experimental results

Figure 4.2 shows the electromagnetically induced gain and absorption resonances on the probe beam and our ability to control these resonances. Here, we measure the peak intensity of the
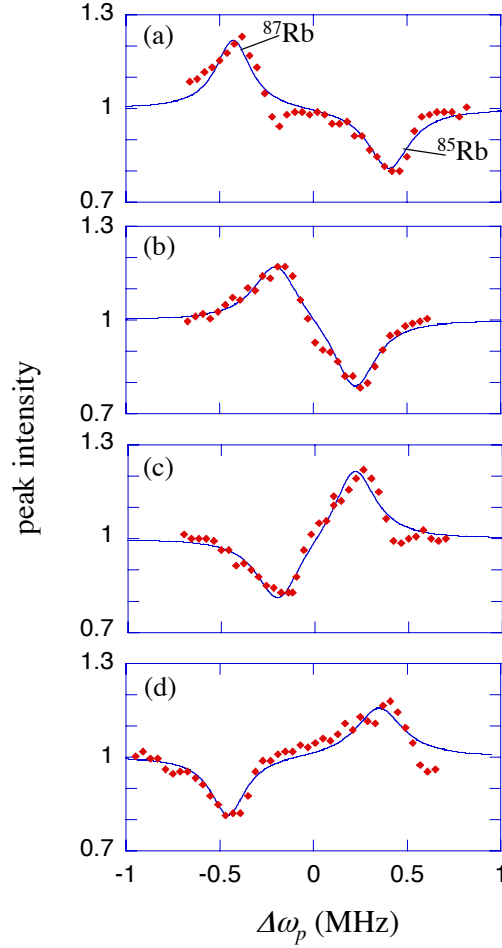
Figure 4.2 The peak intensity of the probe laser measured after the cell as a function of the frequency of the probe laser. With the control lasers, we induce a gain resonance and an absorption resonance on the probe laser. When the probe laser is resonant with the $|F = 2\rangle \to |F = 1\rangle$ Raman transition in ^{87}Rb, the beam experiences gain. When it is resonant with $|F = 2\rangle \to |F = 3\rangle$ Raman transition in ^{85}Rb, the beam experiences loss. By changing the frequencies of the control lasers, we can tune each of the Raman resonances. In plots (a), (b), (c), and (d), the two resonances are spaced by 0.8 MHz, 0.4 MHz, -0.4 MHz, and -0.8 MHz respectively.

probe beam as a function of the probe laser frequency. The solid line in each plot is a fit to the data that assumes each resonance to be a Lorentzian. When the probe laser is resonant with the $|F = 2\rangle \to |F = 1\rangle$ transition in ^{87}Rb, there is gain on the beam. When it is resonant with $|F = 2\rangle \to |F = 3\rangle$ transition in ^{85}Rb, there is loss. By changing the frequencies of the control

lasers, we can control the position of these resonances as we scan the frequency of the probe laser beam. In Figs. 4.2(a) and 4.2(b), the gain resonance happens before the loss resonance whereas in Figs. 4.2(c) and 4.2(d), the situation is reversed.

We proceed with a discussion of the measurement of the refractive index. Due to the spatial profile of the control lasers, the refractive index enhancement is larger at the center of the probe beam when compared with the wings of the beam. As a result, the probe beam acquires a spatially dependent phase as it propagates through the atomic medium. In essence, the medium acts as a thin lens causing the probe beam to focus or defocus after the cell [67]. To measure the electro-magnetically induced focusing effect, we measure the transmission of the probe beam through a 150 μm wide pinhole placed 2.5 m away from the cell. If the beam focuses (de-focuses), the beam size decreases (increases) and the transmission through the pinhole increases (decreases).

In Figure 4.3, we measure the peak intensity of the probe beam simultaneously with the transmission through the pinhole. The pinhole transmission is appropriately normalized to take into account the gain or absorption of the beam. In essence, the intensity measurement of Fig. 4.3(a) probes the imaginary part of the susceptibility (χ'') whereas the pinhole transmission measurement of Fig. 4.3(b) probes the real part of the susceptibility (χ'). For this data, we adjust the control laser frequencies such that the two resonances are separated by 0.2 MHz which is roughly twice the width of each resonance. The pinhole transmission, and therefore the refractive index, is maximized at the point of vanishing gain or loss on the beam. The solid line in Fig. 4.3(a) is a fit to the data that assumes each resonance to be Lorentzian. The solid line in Fig. 4.3(b) is the calculated refractive index based on the fit to the data of Fig. 4.3(a). We see good qualitative agreement between the refractive index calculation and the pinhole transmission data.

4.4 Conclusion

We demonstrate an experiment in which we enhance the refractive index of a 7.5 cm long vapor cell to a level of $\Delta n \approx 10^{-6}$. This result represents is the first experimental observation of an enhanced refractive index using two Raman resonances. A number of experimental improvements will be discussed in the following chapter in order to further increase the observed index. First, the
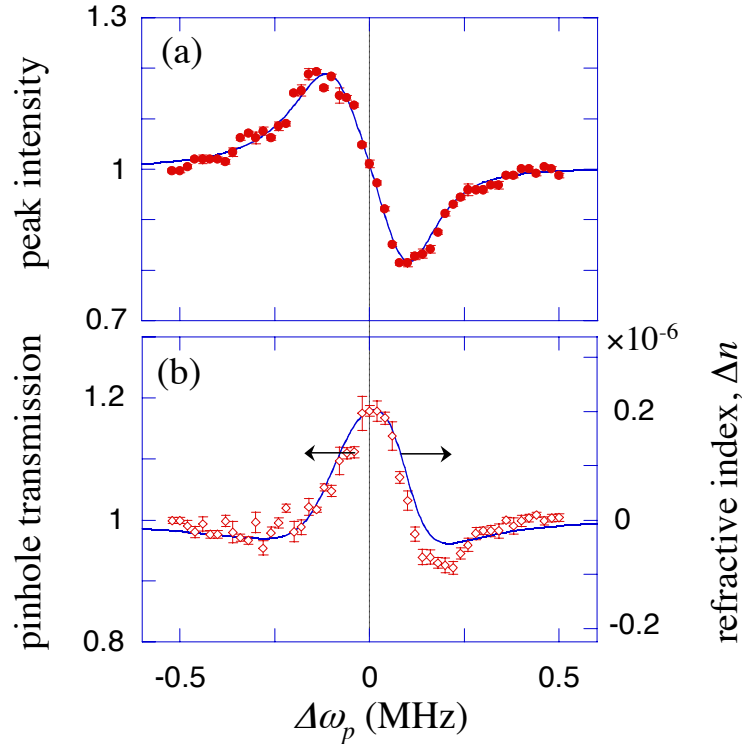
Figure 4.3 Experimental demonstration of the refractive index enhancement at the point of vanishing absorption. (a) The peak intensity of the probe beam and (b) the transmission through a pinhole as a function of probe laser frequency. The transmission through the pinhole changes as a result of focusing or defocusing of the beam due to spatial dependence of the refractive index. The pinhole transmission and therefore the refractive index is maximized at the point of vanishing absorption. The solid line in (a) is a fit that assumes the two resonances to be Lorentzian. The solid line in (b) is the calculated refractive index change at the peak of the spatial profile based on the fit of (a). We see good qualitative agreement between pinhole transmission data and our calculation.

experiment described here suffers from an undesired cross-coupling of the two optical pumping processes. The ^{87}Rb optical pumping laser tries to pump the ^{85}Rb atoms to the wrong state and vice versa. Due to this cross coupling, our optical pumping efficiency is low and the observed refractive index in our experiment is about two orders of magnitude lower than the ideal limit for our experimental parameters. Second, the length of the vapor cell makes for difficult optical

pumping at high densities. In the following chapter, we investigate vapor cells between 100 and 1000 times shorter in length.

Chapter 5

Refractive Index Enhancement in Short Vapor Cells

5.1 Introduction

In the previous chapter, a significant disparity exists between the experimentally observed refractive index enhancement and the theoretical predictions. Here, we discuss possible sources for this disparity and provide recent experimental results. We demonstrate that a careful modifications of the scheme presented in the previous chapter provide a 100-fold improvement in the refractive index enhancement. This requires the use of a 10-times shorter vapor cell, heated to 10-times higher vapor density. Finally, we provide preliminary results very high vapor densities, 100-times higher than that used in the previous chapter.

5.2 Refractive index enhancement in a single isotope

The scheme of chapter 4 calls for a straightforward use of the Raman lasers in both the amplification and absorption scheme. The oppositely-signed imaginary susceptibilities are achieved by initializing the ground Raman level in one isotope, and the excited Raman level in the other isotope. When implementing this protocol, though, a cross-coupling problem is introduced where optical pump laser for each isotope also pumps a small fraction the other isotope, as shown in
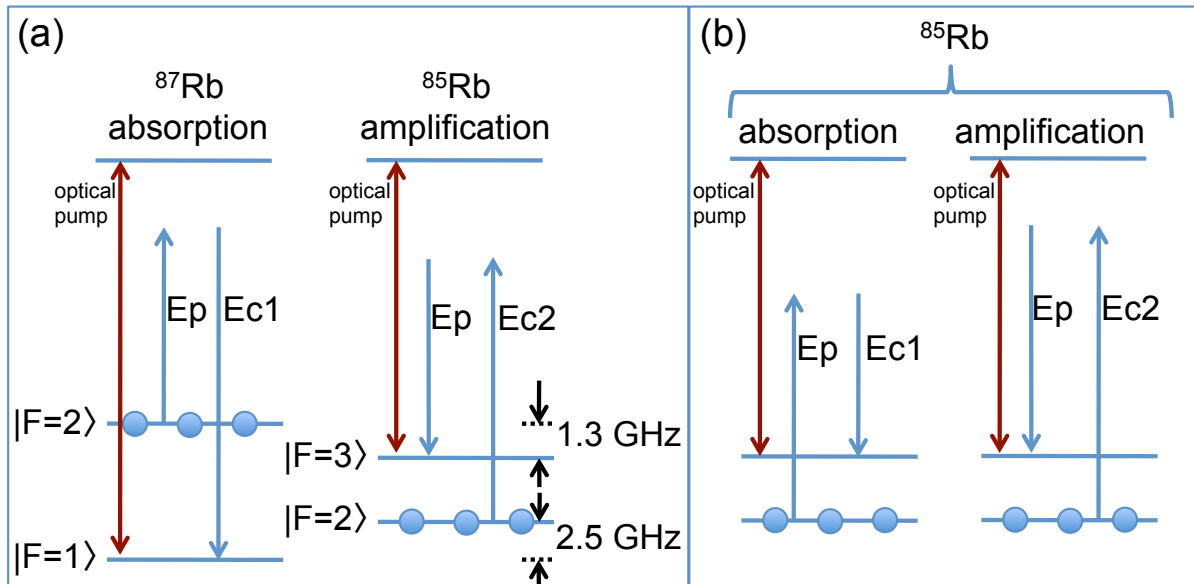
Figure 5.1 Refractive index enhancement energy level schemes. Scheme (a) resulted in undesired optical pump cross-coupling. Specifically, the ^{85}Rb optical pump is detuned from the populated ^{87} level by only 1.3 GHz. Scheme (b) helped solve this problem.

Fig. 5.1(a). This problem stems from the relatively close proximities of the transition frequencies in the different isotopes. For example, the laser that is optically pumping atoms out of ^{85}Rb $|F = 3\rangle$ also causes significant pumping on ^{87}Rb $|F = 2\rangle$. Even though we are using lasers with MHz linewidths, and the levels in the different isotopes are separated by a few Doppler linewidths (hundreds of MHz), the effect is dramatic enough to cause major experimental difficulties. Some of this may be attributed to the significant optical depth of the medium. Successfully taking experimental data with this particular implementation of the refractive index enhancement scheme requires extremely careful balancing of the optical pump powers and frequencies, such that the cross-coupled pumping rates are balanced with each other.

We correct this issue by changing our index enhancement scheme to that of Fig. 5.1(b). The new scheme calls for running the entire experiment in a single isotope. Here, we use ^{85}Rb since its smaller hyperfine spacing in the ground state requires fewer high-frequency AOMs. Additionally, only one optical pump laser is required. Similar to the previous set up, two control beams are required, and one causes probe loss while the other causes probe gain. Fig. 5.1(b) shows that the
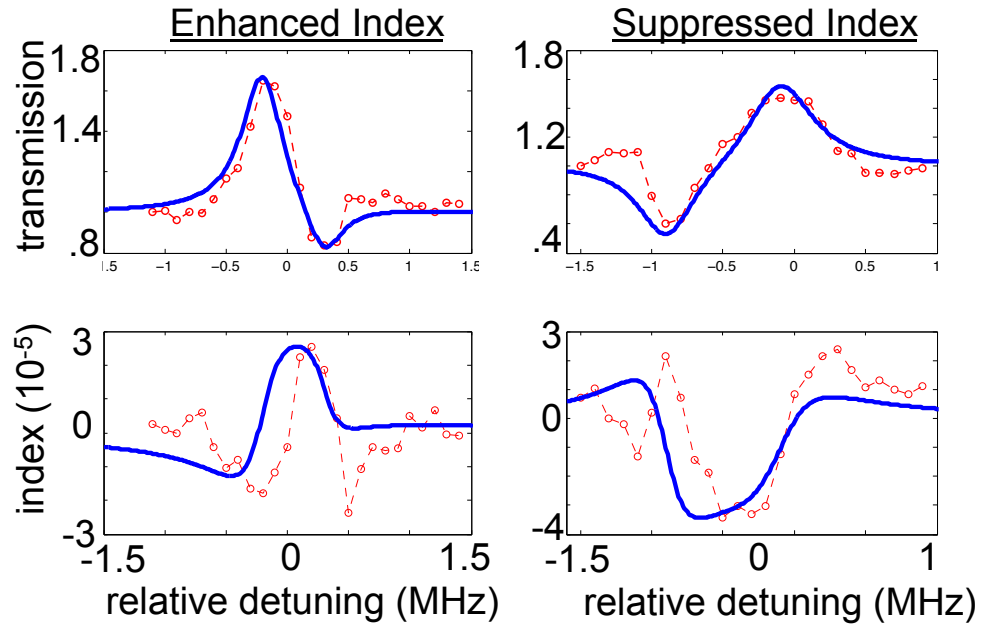
Figure 5.2 We repeat the index enhancement experiment of Chapter 4 using a 1 mm cell. For a 10-fold increase in density, we obtain a 100-fold increase in refractive index.

two-photon resonance set up with the probe and E_{c1} will cause the probe to be absorbed, while the two-photon resonance between the probe and E_{c2} causes gain on the probe. Therefore, this system is synonomous with the scheme of the previous chapter. By setting the beam frequencies such that the probe is tuned to a frequency between the two resonances, the gain and absorption will cancel. As explained earlier, this leaves an enhanced refractive index with no absorptive effects. These modifications to our experiment improved the overall results by about 50% while dramatically simplifying the technical aspects.

The index of refraction of a medium increases with its density. In the case of our vapor cells, a higher gas density requires an exponentially stronger optical pump in order to initialize atoms uniformly over length. For this reason, in order to explore higher densities we move to much shorter cells, one millimeter in length (from 7.5 cm in length, as used earlier).
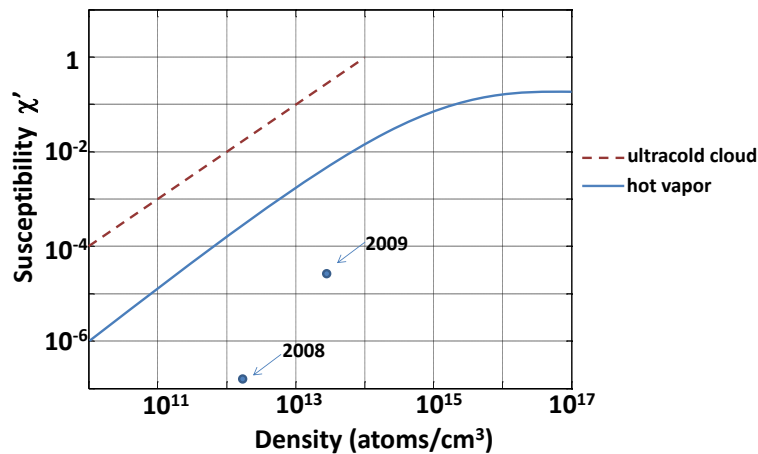
Figure 5.3 Theoretical maximum refractive index enhancement as a function of density. We have made several dramatic improvements to our experiment from the years 2008 to 2009, but still achieve index enhancement about two orders of magnitude below theory.

5.3   Index enhancement in short cells (L = 1mm)

Using the single-isotope technique described above, we explore refractive index enhancement at higher densities. In order to ensure even optical pumping throughout the length of the vapor, we move our experiment from the 7.5 cm cell of the previous chapter, to a 1 mm cell. After setting up the experiment, we slowly heat the vapor cell and monitor the amount of index enhancement. We find that the experiment obtains its best results at a density of 3×10^{13} / cm^3, with a refractive index of n = 3×10^{-5}. The experimentally observed response of the vapor is shown in Fig. 5.2. It is important to note that, for a density only 10 times that of the earlier setup (Fig. 4.3), we obtain a 100-fold increase in refractive index. We understand this counterintuitive observation by assuming that, in the earlier experiment, the optical pump was not effective over the full length of the 7.5 cm vapor cell.

Remarkably, as we further heat the 1 mm cell, the amplitude of the Raman resonances (and the magnitude of the probe phase accumulation) remains roughly the same over about an order of magnitude of density. We see a similar leveling-off of the experimental results in the longer 7.5 cm vapor cell. This leads us to believe that a saturation effect not apparent in simulations is limiting our experimental results. In both the 2008 experiment (N = 10^{12} / cm^3, L = 7.5 cm) and the 2009
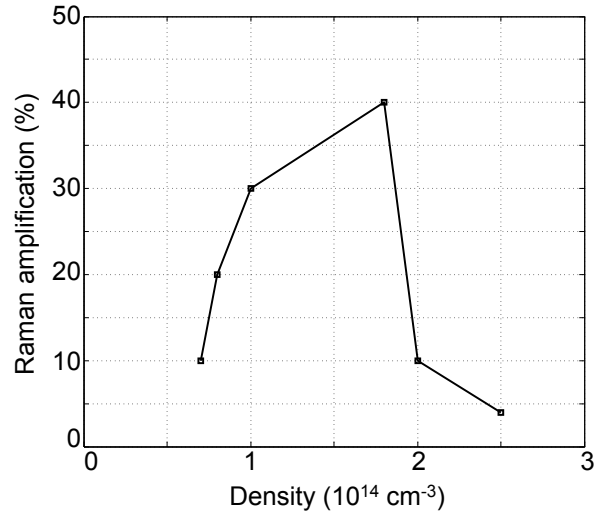
Figure 5.4 Raman amplification of a weak probe beam vs. density. For a probe tuned a few GHz to the blue of the excited state manifold ($\omega_p = 384241$ GHz) and propagating through a 1 mm vapor cell, we observe Raman amplification over only a narrow band of densities.

experiment (N = 10^{13} / cm^3, L = 1 mm), our measurements place us about 100 times below the calculated refractive index value (see Fig. 5.3).

When we measure Raman amplifcation alone, we find that . For a probe tuned a few GHz to the blue of the excited state manifold ($\omega_p = 384241$ GHz) and propagating through the 1 millimeter vapor cell, we detect Raman gain over a narrow band of densities before it drops off. This assumes 130 mW of control power and about 1 Watt of optical pump at the vapor cell.

5.4   Investigations in ultrashort cells (L = 30 μm)

We want to investigate still higher densities while ensuring uniform optical pumping, and to do so we proceed to explore vapor cells shorter than one millimeter. As noted earlier, we infer from our experimental results that the optical pump beam was effective over only a fraction of our longer vapor cells. For this reason, we move to a vapor cell only 30 μm in length. In this regime we are prone to destructive wall collisions at rates of around 10 MHz (see appendix chapter C), setting a bound on our experimental time scale. Using a very weak probe (and no optical pumping or control beams), we scan across the excited state manifold for the D2 line of [85]Rb and [87]Rb. Comparing

the absorption curve to a computer model with appropriate homogeneous and inhomogeneous broadenings taken into account, we ensure that our temperature (density) is correctly measured. This model adds in the pressure broadening due to the buffer gas, and then convolves the modified excited state susceptibility with the Doppler broadening. The results are depicted in Fig. 5.5.

After finding that the density and linewidth broadening of the vapor cell are accurate, we then attempt to optically pump one of the ground states of rubidium. We do this by turning on a strong laser beam tuned to the appropriate transition, in this case $|F = 1\rangle$ of ^{87}Rb. We run this beam for about one millisecond, and then turn it off and begin probing. Using this method, we measure about 90% of ^{87}Rb optical pumping at N = 8.5×10^{13} cm^{-3}, and about 75% optical pumping at N = 4×10^{14} cm^{-3}. The optical pumping efficiency is calculated by fitting the density-length product of our computer model to the absorption data.

We extend the experiment to a density of N = 10^{15} cm^{-3} but we do not observe a measurable amount of optical pumping. Instead we find that all transitions are made optically thinner when the optical pump beam illuminates the sample. These plots are also shown in Fig. 5.5.

5.5   Conclusion

In summary, we improve our experimental results by two orders of magnitude and show an enhanced index of refraction with unity probe transmission, in a single isotope of rubidium. The results leave us with a number of intriguing open problems, such as finding the source of the discrepancy between experiment and theory. Future investigations into this question could involve constructing a variable-length optical cell with real-time control over buffer gas pressures, as well as moving the experiment to the ultracold regime in order to limit the broadening mechanisms. We also plan to build optical filtering cavities to rid the experiment of amplified spontaneous emission (ASE) from our tapered amplifiers (optical power amplifiers).

Finally, we note that our experiment is robust against imperfect optical pumping even at high densities for two key reasons: 1) index enhancement is sensitive to density and not optical depth, meaning we can run our experiment in a dense but optically thin sample, and 2) the experiment runs in the far-off resonance regime so that single-photon effects are minimal. In these two key
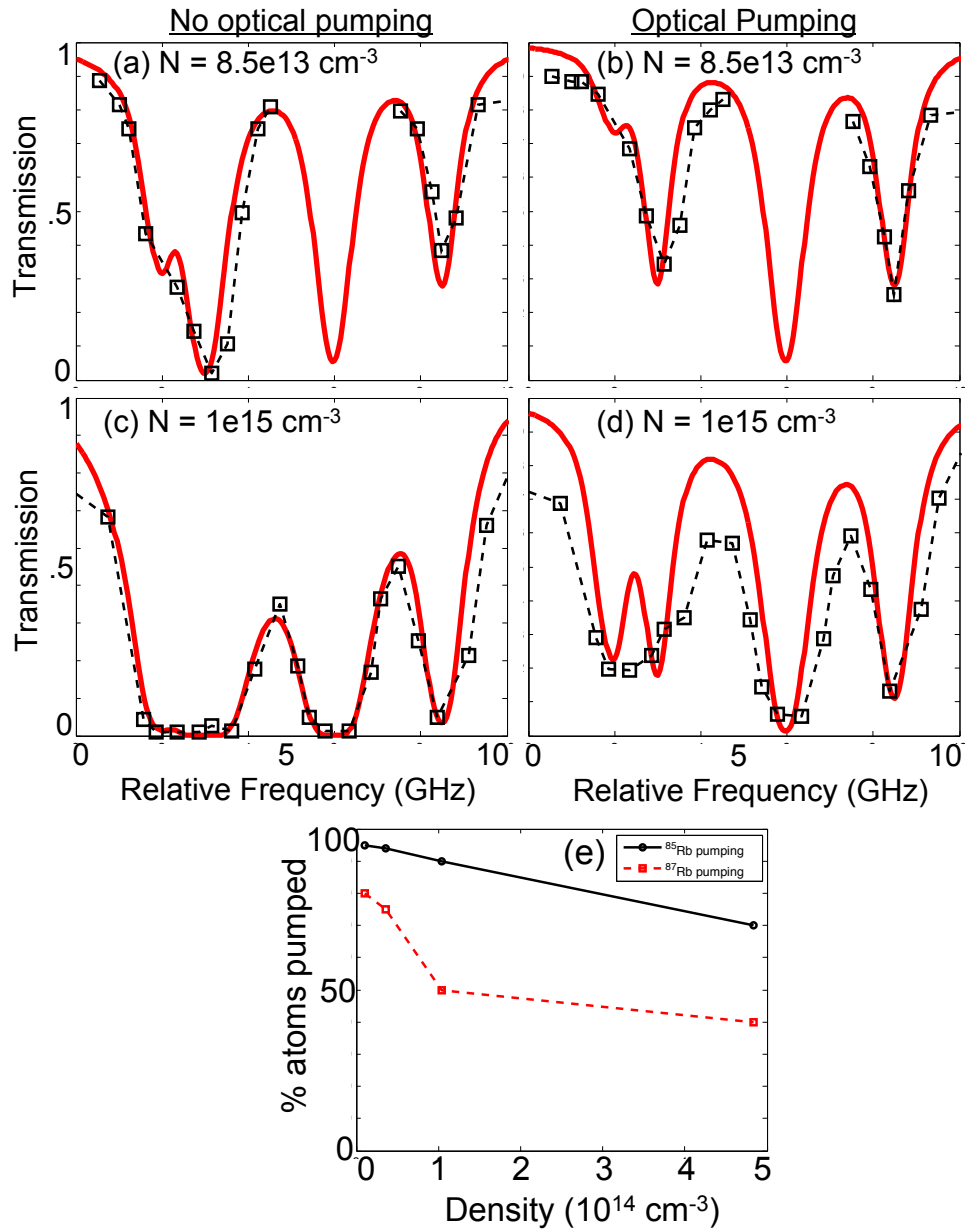
Figure 5.5 Absorption curves taken at N=8.5×10^13/cm^3. (a) clearly shows four peaks total, each one depicting ground state in one of the isotopes. The outer pair of peaks result from ^{87}Rb, and are separated by 6.8 GHz. The inner pair of peaks result from ^{85}Rb and are separated by 3 GHz. In profiles (b) and (d) we use an optical pump laser to pump out the $|F = 1\rangle$ ^{87}Rb ground state.

ways, this experiment differs from experiments with similar schemes, such as those using EIT to modify the group index.

Chapter 6

Observation of Raman Self-Focusing in an Alkali Vapor Cell[1]

6.1 Introduction

In the last several chapters, we presented a system to enhance the refractive index that a very weak probe beam experiences propagating through a gas. There, the frequency of the probe is tuned between a pair of resonances such that the absorptive response of each resonance adds destructively, leaving only the refractive response. We now consider the strong-field regime, where the probe is turned up to an intensity comparable to the strong control beams. When illuminated by two strong laser beams, a dipole-forbidden Raman transition is driven to a maximally coherent state. The population is almost equally split between the two Raman states and the off-diagonal density matrix element of the transition approaches its maximum value, $\rho \approx 1/2$. Unlike previous chapters, here the refractive index of both lasers is modified as a consequence of maximum coherence between ground states [28, 68]. Noting Fig. 6.1, depending on the sign of the two-photon detuning, $\Delta\omega$, the established atomic coherence is either in-phase or π out-of-phase with the strong two-photon drive. As a result, the refractive indices of the two driving lasers, E_p and E_s, are either enhanced ($\Delta\omega > 0$) or reduced ($\Delta\omega < 0$). The modification of the refractive indices is intensity

---

[1]A variation of this chapter can be found at Ref. [67]
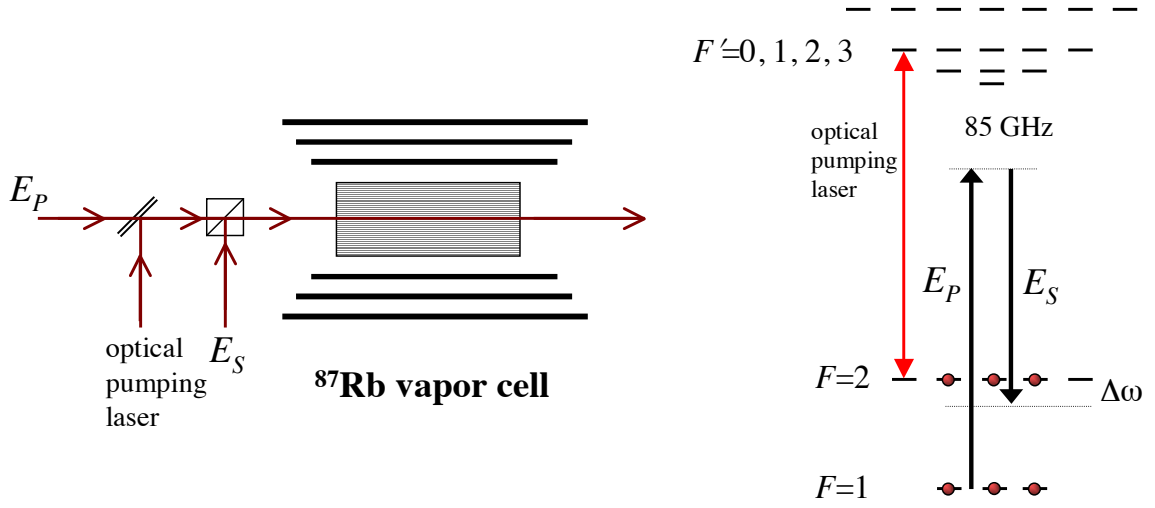
Figure 6.1 Simplified schematic of our experiment and the energy level diagram (not to scale) for ^{87}Rb. The experiment is performed in a temperature controlled triple layer magnetically shielded quartz vapor cell at an atomic density of $N \approx 1.66 \times 10^{13}$ atoms/cm^3. An optical pumping laser tuned to $F = 2 \rightarrow F' = 2$ transition of the D2 line optically pumps the atoms to the $F = 1$ manifold. The two intense laser beams, E_p and E_s drive the atoms to a near maximally coherent state. The two driving laser beams have orthogonal polarizations and they are detuned by 85 GHz from the D2 line (see text for details). The experiment works in three parallel channels with three Raman coherences prepared between the same m-states of the $F = 1$ and $F = 2$ levels (the quantization axis is chosen parallel to the beam propagation direction). Depending on the sign of the detuning from the Raman transition, $\Delta\omega$, the beams either self-focus or self-defocus. To observe the effect, we measure the size of the beams after they exit the cell.

dependent and varies across the spatial profile of the beams. As a result, the medium acts as a lens causing self-focusing or self-defocusing of the driving lasers.

In this chapter, we utilize the hyperfine transition between $|F = 1\rangle$ and $|F = 2\rangle$ levels and demonstrate Raman self-focusing and self-defocusing of the two driving laser beams, E_p and E_s, in a ^{87}Rb vapor cell.

6.2   Experimental Setup

Figure 6.1 shows the relevant energy level diagram and the experimental set up, which is similar to that of previous chapters. We install an isotopically pure ^{87}Rb vapor cell, magnetically shielded

and temperature controlled as described earlier. The vapor cell is again $L = 7.5$ cm long and contains 10 torr of Nitrogen (N_2) as a buffer gas. The temperature of the vapor cell is kept at $T = 120$ degrees Celsius. Using the vapor pressure model of Ref. [69], we calculate the atomic density to be roughly $N \approx 1.66 \times 10^{13}$ atoms/cm^3. We use $F = 1$ and $F = 2$ hyperfine levels of ^{87}Rb in the ground electronic state $5S_{1/2}$ as our Raman states. The Raman transition frequency is the hyperfine splitting which is 6.834 GHz and the two photon detuning from the Raman resonance is defined as $\Delta\omega = 2\pi \times 6.834$ GHz $-(\omega_p - \omega_s)$. For Raman transition between these two levels we utilize far-off resonant excitation through the excited electronic state $5P_{3/2}$ (D2 line) near a wavelength of $\lambda = 780.2$ nm.

The experiment starts with optical pumping of the ^{87}Rb atoms to the $F = 1$ ground state manifold. This is achieved with an optical pumping laser that is saturation absorption locked to $F = 2 \rightarrow F' = 2$ transition of the D2 line. To obtain the necessary amount of power, we use an external cavity diode laser amplified by a semiconductor tapered amplifier. The use of N_2 as a buffer gas greatly alleviates problems due to radiation trapping during the optical pumping process. We find that, with an optical power of about 300 mW in a beam size of $W_0 = 0.57$ mm, we can optically pump a large fraction of the atoms to the $F = 1$ ground state manifold. Once the optical pumping beam is switched-off, the atoms relax back to the $F = 2$ level due to spin exchange collisions. We measure this relaxation time to be about 50 μs which is also the time window to perform the experiment.

Once the optical pumping laser is switched-off, we turn on the two driving laser beams (termed the pump beam, E_p, and the Stokes beam, E_s). The optical power in each beam is 250 mW and the beams have a collimated beam waist of $W_0 = 0.57$ mm at the vapor cell. Since we are working in a hot vapor cell, collinear propagation of the two beams is critical in order to avoid two-photon Doppler broadening. We guarantee perfect overlap by coupling all the laser beams into a single mode, polarization maintaining fiber before the vapor cell (not shown in Fig. 6.1). The two laser beams have orthogonal linear polarizations at the vapor cell with a polarization purity at the 1 % level.

As described in detail in previous chapters, the two driving laser beams, E_p and E_s, are obtained from the same external cavity diode laser, and are then frequency-shifted and amplified. The one-photon detuning of the two lasers from the excited electronic state $5P_{3/2}$ is 85 GHz, which is large when compared with the Doppler linewidth of this state (650 MHz). The system is, therefore, a far-off resonant system and the Raman interaction is the dominant interaction of the two lasers with the atomic vapor.

The optical pumping process does not pump to a specific m-state in the ground $F = 1$ manifold. As a result, after the optical pumping process, the atoms are distributed to all three m-states at the $F = 1$ level. The experiment, therefore, works in three parallel channels and three Raman coherences $\rho_{-1,-1}$ ($|F = 1, m_F = -1\rangle \rightarrow |F = 2, m_F = -1\rangle$), $\rho_{0,0}$ ($|F = 1, m_F = 0\rangle \rightarrow |F = 2, m_F = 0\rangle$), and $\rho_{1,1}$ ($|F = 1, m_F = 1\rangle \rightarrow |F = 2, m_F = 1\rangle$), are driven with the two laser beams. To allow adiabatic preparation of the Raman coherences, we turn-on the two lasers smoothly over about 4 μs. In this regime, depending on the sign of the Raman detuning, $\Delta\omega$, the established Raman coherences are either in-phase ($\Delta\omega > 0$) or π out-of-phase ($\Delta\omega < 0$) with the two-photon driving force [28, 68]. As a result, the refractive indices of the driving lasers are either enhanced or reduced. For the parameters of our experiment, the medium acts like a thin lens producing a curved phase front on the beams at the end of the vapor cell. There is not a significant change in the spatial profile of the beams inside the medium. After the beams exit the vapor cell, their beam size is measured 75 cm away from the cell by monitoring the amount of transmitted power through a 150 μm pinhole.

6.3 Self-focusing results and comparison to theory

Figure 6.2 shows the normalized transmitted power of the two laser beams through the pinhole. The dashed line is the transmission in the absence of the Raman interaction (freely propagating beam). The transmission, and therefore the size of the beams, reaches its maximum and minimum values off-resonance demonstrating the Raman self-focusing and defocusing effect. We see an abrupt transition from beam maximum to beam minimum while scanning through the Raman resonance. For large values of the detuning $\Delta\omega$, the atomic coherence decreases and the beam
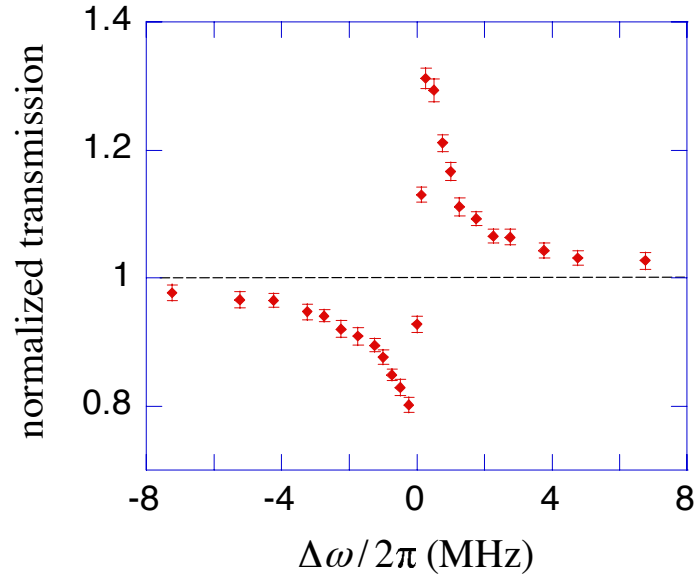
Figure 6.2 Transmission of the two laser beams through a 150 μm pinhole as a function of the two-photon detuning, $\Delta\omega$. The dashed line is the transmission in the absence of the Raman interaction (freely propagating beam). The beam width reaches its maximum and minimum values off-resonance demonstrating the Raman self-focusing and defocusing effect. We see an abrupt transition from beam maximum to minimum while scanning through the Raman resonance. For large values of the detuning $\Delta\omega$, the atomic coherence decreases and the beam width approaches the value of a freely propagating beam (dashed line).

width approaches the value of a freely propagating beam (dashed line). The beam size reaches its maximum and minimum values at $\Delta\omega = 2\pi \times -0.25$ MHz, and $\Delta\omega = 2\pi \times 0.25$ MHz respectively. We calculate the value of the coherence of the Raman transitions at the intensity peak of the lasers to be $\rho = -0.46$ (for $\Delta\omega = 2\pi \times -0.25$ MHz) and $\rho = 0.49$ (for $\Delta\omega = 2\pi \times 0.25$ MHz) respectively (for all three channels). The established atomic coherence is slightly larger for the positive detuning due to the Stark shift of the Raman resonance. For $\Delta\omega > 0$, the Stark shift tunes the driving lasers closer to Raman resonance as the laser intensities are increased. This is also the reason for the slight asymmetry between the two sides of the resonance in the transmission data of Fig. 6.2.
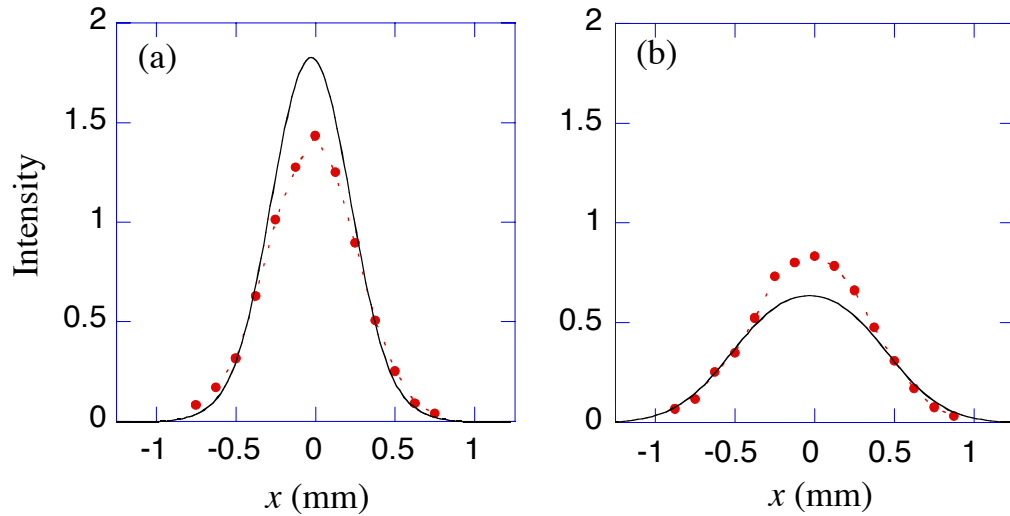
Figure 6.3 The data points are the spatial profiles of the two driving laser beams (a) for the focused ($\Delta\omega = 2\pi \times 0.25$ MHz) and (b) for the defocused ($\Delta\omega = 2\pi \times -0.25$ MHz) cases. The measured FWHM size of the beams is 0.64 mm [part (a)] and 0.88 mm [part (b)] respectively. The solid curve in each plot is the result of a numerical simulation for each experiment without any adjustable parameters. The agreement between the experimental results and the numerical simulations is reasonably good for both cases.

Figure 6.3 shows the experimentally measured spatial profiles of the two driving laser beams for the focused ($\Delta\omega = 2\pi \times 0.25$ MHz) and defocused ($\Delta\omega = 2\pi \times -0.25$ MHz) cases. These profiles are recorded 75 cm away from the cell by moving the pinhole with a translation stage. Similar to Fig. 6.2, the intensities are normalized such that 1 unit in the plots corresponds to the peak intensity of a freely propagating beam (in the absence of Raman interaction). When the beams are focused and defocused their measured full width at half maximum (FWHM) sizes are 0.64 mm and 0.88 mm respectively. The solid curves in each plot are the results of numerical calculations for our experiment without any fitting parameters. The assumptions that we make in these numerical calculations are: (1) We neglect the residual two-photon Doppler broadening due to the finite size of the beams. (2) We ignore atomic motion since the diffusion of atoms during the time scales of interest is much smaller when compared with the size of the beams. (3) We ignore relaxation processes since our pulse-widths are much shorter when compared with the relevant relaxation

before the cell

after the cell

(a)

(b)
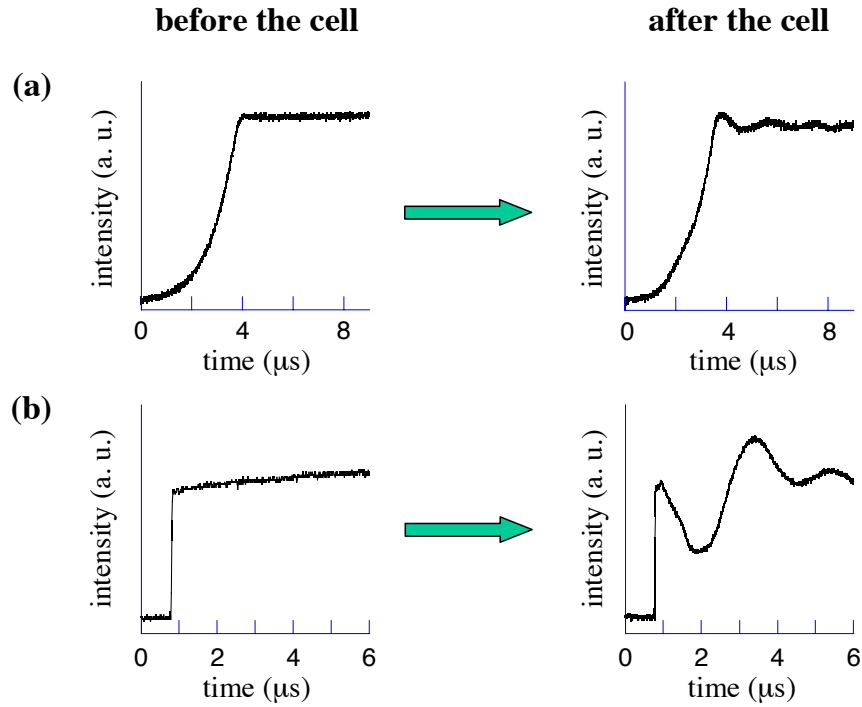
Figure 6.4 The temporal profiles for the pump laser beam, E_p, measured before and after the vapor cell. In part (a), the pump laser smoothly turns-on to its peak value in about 4 μs. Here, the atomic evolution is adiabatic and the pump laser largely preserves its smooth nature as it propagates through the vapor cell. In part (b), we turn on the pump laser sharply. As a result, the evolution is non-adiabatic, and the atomic population Rabi flops between the two levels. This flopping results in large variations in the amplitude of the pump laser as it leaves the vapor cell. To allow adiabatic preparation of an appropriately phased Raman coherence, all the measurements of Figs. 6.2 and 6.3 were performed with the smooth profiles of part (a).

times. With these assumptions, we solve the slowly varying envelope propagation equations for the two laser beams in full three spatial dimensions (two transverse dimension and one propagation dimension) simultaneously with the adiabatic solution for the atomic system. The propagation of the two laser beams is coupled to each other through the established hyperfine coherences in three parallel channels. Further details with regard to the numerical simulations can be found in Ref. [34]. The agreement between our numerical calculations and the experimental results is reasonably good for both cases.

6.4 Pulse shaping and Rabi Flopping

We next discuss the adiabatic preparation of the medium. As shown in Fig. 6.4(a), to adiabatically prepare a maximally coherent state, we turn-on the two driving laser pulses smoothly in about 4 μs. We then make our measurements at the peak of the pulses. Fig. 6.4 contrasts adiabatic and non-adiabatic evolution of the atomic system. Here we plot the total power (measured without the pinhole) of the pump beam E_p, before and after the vapor cell for a two-photon detuning of $\Delta\omega = 2\pi \times 0.25$ MHz. In part (a), the evolution is adiabatic, and the temporal profile of the pump beam largely retains its smooth nature after propagating through the vapor cell. In part (b), we turn on the laser beams sharply, and as a result, the atomic population two-photon Rabi flops between the two hyperfine levels. This flopping is reflected in periodic absorption and amplification of the pump beam measured after the cell. Due to the Gaussian intensity distribution in the vapor cell, atoms at different positions along the spatial profile of the laser beams Rabi flop at different rates. As a result, the Rabi-flopping time dynamics are complicated and can not be explained with a single two-photon Rabi frequency. We do observe the general characteristics of a Rabi-oscillation behavior. As an example, as we detune further from the resonance, Rabi oscillation frequency increases and oscillation amplitude decreases. All the measurements of Figs. 6.2 and 6.3 were performed with the smooth profiles of Fig. 6.4(a).

6.5 Conclusion

We have now presented observation of refractive index modification in both the weak- and strong-field regimes. Unlike earlier chapters, the key idea in the strong-field regime is to adiabatically prepare the hyperfine transitions in a maximally coherent state. This approach achieves very large nonlinearities in a far-off resonant system and does not suffer from dissipation due to excited state spontaneous emission. If we ignore the saturation of the nonlinearity due to operating near maximum coherence, the Raman self-focusing effect can be modeled as an intensity dependent refractive index. For $\Delta\omega = 2\pi \times 0.25$ MHz, the value of the nonlinear index achieved in our experiment is $n_2 = 1.6 \times 10^{-7}$ cm^2/W. The parameters of our experiment are similar to the numerical

simulations where formation and collisions of spatial Raman solitons are predicted [34]. In order to observe these solitons, we would need to to use higher density and focus our beams to spot sizes of about $W_0 = 100$ μm and demonstrate diffraction free propagation for distances much larger than the Rayleigh length of the beam.

Chapter 7

Nanoscale Resolution Fluorescence Microscopy Using Electromagnetically Induced Transparency[1]

7.1   Introduction

The previous chapters described how to modify the index of refraction of a vapor. As already noted, these methods could be utilized to enhance the imaging resolution of a microscope by reducing the effective wavelength of the probing light.

Now we turn our attention to a type of scanning fluorescence microscope that is capable of resolving nanometer-size objects in the far field. The key idea is to localize the atomic excitation of atoms to a spot much smaller than a diffraction limited optical waist by using a laser beam with a particular spatial pattern. Using this idea, we begin by considering a nanoscale sample embedded in a gas of atoms. We scan a pair of focused beams throughout the gas, putting each region into a spatially-sensitive EIT dark state. In each scanned area, only atoms tightly localized to the center of the optical waists are excited to a different energy level. In this chapter, we predict that the shadow of the sample can be imaged with subwavelength resolution. In the following chapter we

---

[1]A variation of this chapter can be found at Ref. [70].

demonstrate the key idea of this suggestion by preparing a cloud of atoms in a spatially-sensitive dark state.

7.2 Background

It is well-known that by using the nonlinear interaction between atoms and laser beams, one can localize atoms to a spot much smaller than the wavelength of light. As noted earlier, in their pioneering work, Thomas and colleagues have suggested and experimentally demonstrated sub-wavelength position localization of atoms using spatially varying energy shifts [14–16]. If a very small object is embedded into an atomic medium, sub-wavelength atom localization can be used to obtain a shadow image of the object [16]. Recently, there has been a growing interest in various techniques of manipulation of atoms at the sub-wavelength scale. Zubairy and colleagues have discussed atom localization using resonance fluorescence and phase and amplitude control of the absorption spectrum [71–73]. Knight and colleagues discussed localization via quantum interference at the probability amplitude of the excited state [74]. There is also substantial literature on sub-wavelength localization of atoms utilizing excitation in a standing wave [75, 76]. Although these are very exciting developments, a practical optical microscope utilizing nano-scale localization of atoms has not yet been demonstrated. If constructed, such a microscope may provide a unique way to image small objects including large biological molecules at the nanometer scale. Although significant advances have been made in recent years such as the invention of Stimulated Emission Depletion Microscopy (STED) [77], it is still a big challenge to map and understand the structure of single molecules.

In addition to imaging, these schemes can also be used manipulating individual atoms in a quantum computing architecture. A simple example is initializing qubits in a lattice to a particular set of states. While an optical lattice with spacing $\lambda/2$ can be formed with an optical standing wave, addressing single atoms or qubits is difficult without cross-talk. The scheme described here allows for a reduction in these types of errors, as discussed in detail in Ref. [78].

We note that there has also been remarkable experimental progress in utilizing the position dependent stimulated emission to achieve nanoscale resolution [77, 79, 80]. This approach, also

known as stimulated-emission depletion microscopy, is now a widely used technique in biological imaging. We note that our approach of using the dark state for atomic localization has the following key advantages: 1) For the ideal case of sufficiently slowly varying driving laser pulses, the dark-state technique has no population at the excited electronic state. As a result, the atomic localization can, in principle, be achieved without suffering from the detrimental effects of spontaneous emission. This is especially important for quantum computing applications [78] where coherent manipulation with little decoherence is essential. 2) The dark state can be prepared adiabatically by using a counter-intuitive pulse sequence. As a result, as discussed in detail later on, the scheme is insensitive to many experimental fluctuations such as the intensity and the timing jitter of the driving laser pulses. 3) Since the scheme is coherent, localization can be achieved at faster time-scales at the expense of requiring more intense laser beams. Although in this work we use ≈ 100 ns-long laser pulses, dark-state-based localization can easily be achieved at sub-ns time-scales by using more powerful laser beams.

7.3   Nanoscale microscopy using EIT

The scheme presented in this chapter is the extension of the suggestion of Agarwal and colleagues to tightly focused beams and utilizes adiabatic evolution instead of optical pumping [76]. Noting Fig. 7.1, we consider a nm-scale object embedded in an ultracold atomic medium with four atomic states. As an example, the atomic medium can be μK temperature alkali atoms trapped in a magneto-optical trap (MOT) or in a far-off resonant dipole trap. Two laser beams couple the two hyperfine states of the atom (states $|1\rangle$ and $|2\rangle$) to an excited electronic state (state $|3\rangle$) and form a traditional Λ scheme. With an atom starting in the ground state $|1\rangle$, using a counterintuitive pulse timing sequence, the atomic system can be prepared in the dark state. When this is the case, the probability amplitudes of states $|1\rangle$ and $|2\rangle$ depend very sensitively on the ratio of the Rabi frequencies of the two laser beams, Ω_p and Ω_c. The nonlinearity of this dependence can be used to spatially localize the population of state $|2\rangle$ to a very tight spot. The fluorescence laser between states $|2\rangle$ and $|4\rangle$ then causes fluorescence from the localized excitation. As a result, by scanning
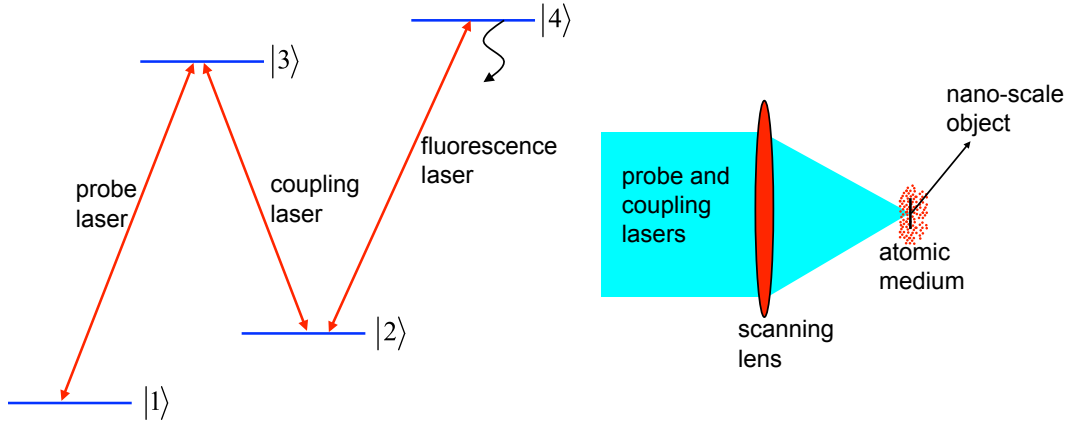
Figure 7.1 Energy level diagram and simplified schematic of the suggested technique. The probe and the coupling laser beams form a traditional Λ scheme and drive the atoms into the dark state. The sensitive spatial dependence of the dark state on the intensities of the two laser beams can be used to localize the population of state $|2\rangle$ to a spot much smaller than the diffraction limit. The fluorescence laser that scatters photons only when the atom is in state $|2\rangle$ may then be used to detect the tightly localized population. By scanning the focusing lens, a fluorescence shadow image of the embedded object at the nanometer scale is obtained.

the focusing lens, it becomes possible to obtain a fluorescence shadow image of the embedded object at the nanometer scale.

We proceed with a detailed description of our scheme. Noting Fig. 7.1, with the fluorescence laser turned-off, the dark state of the atom is [1, 17]:

$$|\psi_{dark}\rangle = \frac{\Omega_c^*}{\sqrt{|\Omega_p|^2 + |\Omega_c|^2}}|1\rangle - \frac{\Omega_p^*}{\sqrt{|\Omega_p|^2 + |\Omega_c|^2}}|2\rangle \quad . \tag{7.1}$$

From Eq. (7.1), the population of state $|2\rangle$ is $|\langle 2|\psi_{dark}\rangle|^2 = |\Omega_p|^2/(|\Omega_p|^2 + |\Omega_c|^2)$ and gets larger as the ratio $|\Omega_c/\Omega_p|$ is decreased. This suggests that in a region where the coupling laser goes through an intensity minimum and the probe laser goes through an intensity maximum, the population in state $|2\rangle$ can be localized very tightly. If we assume Gaussian focusing and take the spatial profiles of the two Rabi frequencies at the focus as $\Omega_p(x, y) = \Omega_{p,peak} \exp\left[-(x^2 + y^2)/W_0^2\right]$, $\Omega_c(x, y) = \Omega_{c,peak} - \Omega_{c,peak} \exp\left[-(x^2 + y^2)/W_0^2\right]$ where W_0 is the Gaussian spot size, it can be shown that in the limit $\Omega_{p,peak} << \Omega_{c,peak}$, the population of state $|2\rangle$, $|\langle 2|\psi_{dark}\rangle|^2$, will be localized

to an approximate spot size of:

$$W_{excitation} \approx W_0 \sqrt{\frac{\Omega_{p,peak}}{\Omega_{c,peak}}} \quad . \tag{7.2}$$

Here, we take the atoms to be cold enough such that their motion can be neglected during excitation with the probe and coupling lasers. From Eq. (7.2), it follows that the resolution of such a microscope is $(\lambda/2)\sqrt{\Omega_{p,peak}/\Omega_{c,peak}}$ and for $\Omega_{p,peak} << \Omega_{c,peak}$ the resolution is significantly smaller than the wavelength of light. Use of more complicated focusing schemes where the coupling field goes through a phase change around its minimum provides better scaling of the resolution, $(\lambda/2)\Omega_{p,peak}/\Omega_{c,peak}$, at the expense of significant complications at the excitation structure.

Before describing a possible specific implementation of this nanoscale microscope, we note that the following chapter experimentally demonstrates the fundamental principle behind this microscope. We show the localization of atomic excitation due to the spatial dependence of the dark state. The spatial dependence is achieved using a standing-wave coupling beam, rather than an optical bottle beam as described in this chapter, for the purpose of experimental simplicity. This particular coupling beam spatial structure as a more favorable excitation scaling, going like $\Omega_{p,peak}/\Omega_{c,peak}$.

We now proceed with a numerical example of the optical bottle beam in a real atomic system. We take our atomic medium to be ^{87}Rb and choose $|1\rangle \equiv |F = 2, m_F = -2\rangle$ and $|2\rangle \equiv |F = 1, m_F = 0\rangle$ of the ground electronic state $5S_{1/2}$. We take the excited state to be $|3\rangle \equiv |F' = 2, m_F = -1\rangle$ of the electronic state $5P_{1/2}$ (D_1 line with a transition wavelength of 795 nm). The decay rate of the excited state is $\Gamma = 2\pi \times 5.7$ MHz. We take the probe and coupling laser beams to be of opposite circular polarization (σ^+ for the probe and σ^- for the coupling). For this choice of state selection and polarization selection for the laser beams, the effect of the intense coupling laser on the ground state $|1\rangle$ (such as Stark shift and optical pumping) is negligible due to angular momentum selection rules. Since the two laser beams are focused tightly into the cloud, we need to consider vectorial properties of light to get an accurate distribution of the Rabi frequencies near the focus, $\Omega_p(x,y,z)$ and $\Omega_c(x,y,z)$. For this purpose, we use the formalism of Richards and Wolf [81]. We assume a semi-aperture angle of $\alpha = 60$ degrees for focusing
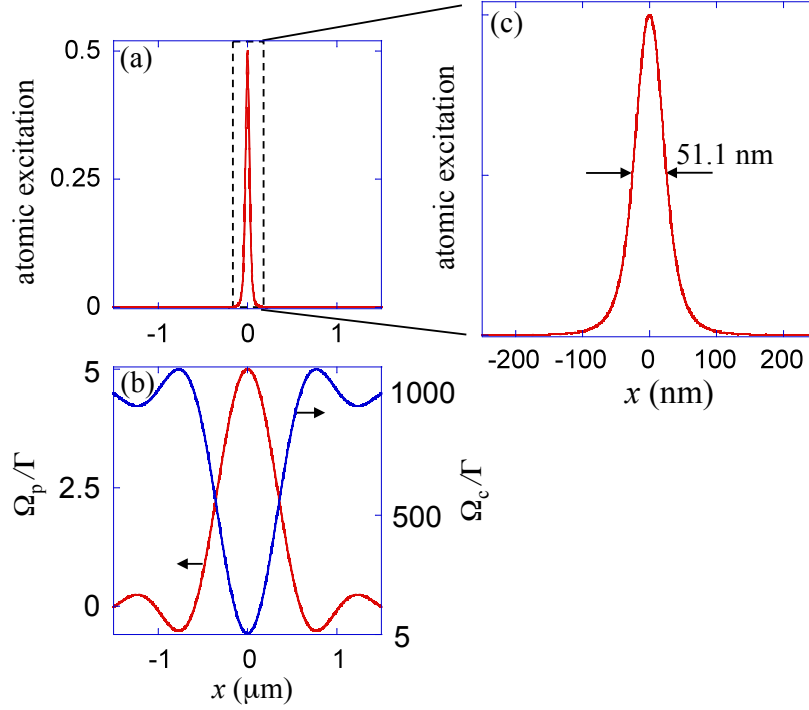
Figure 7.2 Localization of atomic excitation to a spot much smaller than the diffraction limit. Plot (a) shows the atomic excitation, $|\langle 2|\psi_{dark}\rangle|^2$, assuming that the atomic system is in the dark state given by Eq. (7.1). Plot (b) shows the spatial distribution of the Rabi frequencies for the probe laser, Ω_p, and the coupling laser, Ω_c, which results in the localization of plot (a). These distributions are calculated numerically by taking into account vectorial properties of light near a tight focus. Plot (c) is a zoom in on plot (a) detailing the spatial structure of the excitation. The excitation has a FWHM of 51.1 nm which is about 15 times smaller than the wavelength of light.

and calculate the three dimensional distribution of the electric field numerically. To obtain an intensity minimum in the profile of the coupling laser beam, we use the approach of Saffman and colleagues [82]. For this purpose we use two co-propagating coupling laser beams, one tightly focused (with $\alpha = 60$ degrees) and one plane wave, and adjust their phases such that there is destructive interference at the focus. We note that one may use other methods for generating beams with an intensity minimum at the center [83]. A one-dimensional cross section along one of the transverse coordinates is shown in Fig. 7.2(b). We take the peak values for the Rabi frequencies of the two laser beams as $\Omega_{p,peak} = 5\Gamma$ and $\Omega_{c,peak} = 1000\Gamma$. When the coupling laser intensity vanishes, the dark state solution of Eq. (7.1) is no longer valid. To avoid this, we adjust the focusing

parameters such that the coupling laser Rabi frequency doesn't vanish at $x = y = 0$ but instead drops to a low value of 5Γ. The system is, therefore, at the maximally coherent state at $x = y = 0$.

With the spatial profiles for the Rabi frequencies known, we can calculate the fractional populations of the dark state as per Eq. (7.1). In Fig. 7.2(a), we plot the population fraction, $|\langle 2|\psi_{dark}\rangle|^2$, as a function of one of the transverse coordinates. For comparison, Fig. 7.2(b) shows the spatial profiles of the Rabi frequencies of the two laser beams. Fig 7.2(c), is a zoom in on the spatial profile of part (a). The population transfer to state $|2\rangle$ has a FWHM of 51.1 nm which is about 15 times smaller than wavelength of the laser beams, in rough agreement with the qualitative estimate of Eq. (2).

7.4   Adiabatic preparation

In Fig. 7.2, we assumed the ideal case and considered an atomic system in an exact dark state as given by Eq. (7.1). We next discuss temporal evolution of the atomic system. For this purpose we numerically solve the Schrodinger's equation for the probability amplitudes of the three states [84]. To prepare the atomic system in the dark state, we follow the well-known approach and use a counter-intuitive pulse sequence [1, 17]. As shown in the inset of Fig. 7.3, the coupling laser beam (dashed line) is turned on before the probe laser beam (solid line). For this type of preparation, the dark state is smoothly connected to the ground state and the atomic system is adiabatically prepared into the dark state. Once the laser beams are turned on, they can be turned-off simultaneously preserving the ratio of the Rabi frequencies. As a result, even after the laser pulses are gone, the atomic system is left in the state as determined by the probe and coupling laser Rabi frequencies at the temporal-peak of the pulses.

Figure 7.3 shows an exact numerical simulation that confirms the predictions of the results of Fig. 7.2. Here, we solve the Schrodinger's equation at each point in the spatial profiles of the probe and coupling laser beams of Fig. 7.2(b). The inset shows the assumed (normalized) temporal profiles for the intensities of the probe (solid) and coupling (dashed) laser beams. The probe laser is assumed to be a Gaussian pulse with a Gaussian width of $\tau = 0.1~\mu s$. The coupling laser turns-on before but turns-off simultaneously with the probe laser. In the main plot, the data
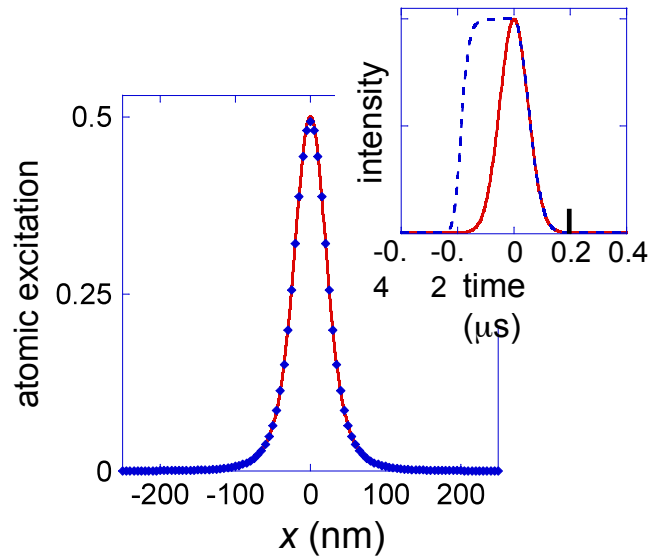
Figure 7.3 A numerical calculation that demonstrates localization with pulsed excitation. The inset shows the assumed temporal profiles for the intensities of the probe (solid) and coupling (dashed) laser beams. Starting from the ground state $|1\rangle$, we numerically integrate Schrodinger's equation at each spatial point along the profiles of the probe and coupling laser beams of Fig. 7.2(b). The data points are the fractional population, $|\langle 2|\psi\rangle|^2$, at $t = 0.2 \ \mu s$ (shown with a tick-mark at the inset), at each spatial point. The solid line is a re-plot of Fig. 7.2(c). There is good agreement between the results of the exact numerical simulation and the idealized calculation of Fig. 7.2.

points are the fractional population, $|\langle 2|\psi\rangle|^2$, at $t = 0.2 \ \mu s$ (shown with a tick-mark at the inset), at each spatial point. The solid line is a re-plot of Fig. 7.2(c). We observe very good agreement between the exact numerical simulation and the idealized calculation of Fig. 7.2. Once the probe and the coupling lasers are switched-off ($t > 0.2 \ \mu$s), the fluorescence laser is switched on. The fluorescence laser does not need to be spatially selective and it can have a large spot size. The motion of the atoms during the fluorescence process is not of importance. By scanning the focusing lens and by repeating the pulsed excitation-fluorescence detection cycle at each scanning point, the fluorescence image of the embedded object is obtained.
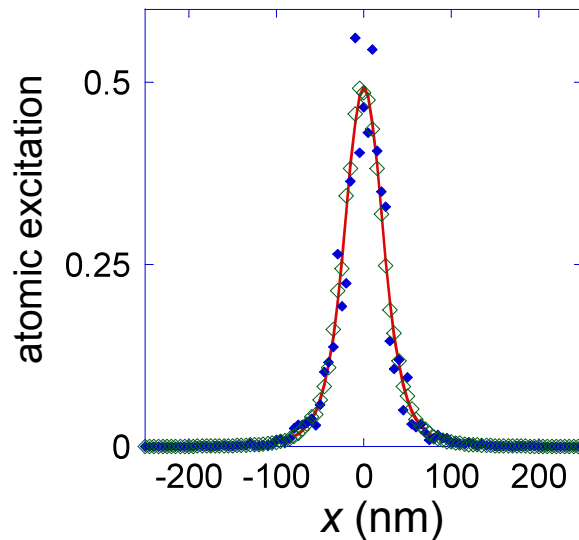
Figure 7.4 Numerical simulations that demonstrate the robust nature of our scheme. For the open squares, the intensity of the coupling laser beam fluctuates by ± 10 % at each scanning point. For the solid squares, a timing jitter of ± 0.01 μs is assumed between the probe and coupling laser pulses. All the other parameters are identical to those of Fig. 7.3. The solid line is a replot of the numerical simulation of Fig. 7.3 .

7.5   Sensitivity to experimental error

A significant advantage of our approach is its insensitivity to fluctuations in many experimental parameters. This is due to the robust nature of adiabatic preparation and is also the key reason for the success of the technique of stimulated Raman adiabatic passage (STIRAP) [85]. Figure 7.4 demonstrates this result. Here, the solid line is a replot of the numerical simulation of Fig. 7.3. For the open squares, with all other parameters identical to those of Fig. 7.3, the intensity of the coupling laser beam fluctuates by ± 10 % at each scanning point. For the solid squares, a timing jitter of ± 0.01 μs is assumed between the probe and coupling laser pulses. For both cases, the numerical results are very close to the profile when there is no fluctuation (solid line) proving the insensitivity of the resolution.

A significant limitation of atom localization based microscopes is the scanning speed. For the numerical example considered, the atomic excitation at each scanning point will be localized to a

volume of 2×10^{-16} cm^3. Current laser cooling and trapping techniques allow ultracold atomic densities exceeding $N = 10^{14}$ atoms/cm^3 [86]. For such densities, a guaranteed excitation of at least one atom requires about $1/(NV) \approx 50$ pulsed excitation-fluorescence detection cycle at each scanning point. Since detection of a single atom with a good signal-to-noise requires about 10 ms integration time [52–54], this means that each scanning point with a resolution of Fig. 7.2 would require about 0.5 second of integration time. This limitation can be overcome by using faster state selective detection techniques. One approach could be to use state selective ionization followed by ion detection. Such approaches can reduce the required integration time for each scanning point to below 1 ms.

Throughout this chapter, we have assumed the atoms to be cold enough such that their motion can be neglected during the adiabatic excitation with the probe and the coupling laser beams. For an excitation time of $\tau = 0.1$ μs this assumption is satisfied for alkali atoms that are cooled to about 50 μK which is readily achievable with sub-Doppler cooling in optical molasses. For the numerical results of Fig. 7.3, we calculate the heating of the atoms during the pulsed excitation with the probe and coupling lasers to be negligible. The required laser power for the experimental observation of the results of Figs. 7.2 and 7.3 are low ($<$1 mW), and are readily achievable with available diode lasers. Throughout this chapter, we have also neglected the interaction of the object with the atomic cloud. The dominant force between the neutral atoms and the embedded object at short separations ($r < 1$ μm) is the van der Waals force. The strength of the van der Waals interaction between alkali-metal atoms and surfaces is well studied [87–89]. If we assume that the surface is an infinite planar surface, we estimate the frequency shift of the ground and the excited states to be at the MHz level for atom-surface separation of $r = 50$ nm. Since this shift is much smaller than the Rabi frequencies of the probe and the coupling laser beams, we do not expect significant corrections to the results presented in this chapter due to atom-surface interactions. However, for $r = 10$ nm, the transition shifts and the heating of the atoms become significant. These effects need to be carefully taken into account, for resolutions below 10 nm. In principle, these effects can be overcome by using larger Rabi frequencies for the probe and the coupling laser beams and using shorter excitation pulses [50].

7.6 Conclusion

In order to utilize this scheme for microscopy, we envision that an experimental demonstration that uses a nanoscale object such as a carbon nanowire inside the Rb cloud. These experiments will be very much in the spirit of recent experiments by Hakuta and colleagues where a nanofiber was placed inside a magneto optical trap of ultracold atoms and the optical properties of atoms near the nanofiber was studied [90]. In these experiments, no significant heating of the ultracold atomic cloud was observed. Another exciting direction is if such a microscope can be used to image large biological molecules at the nanometer scale. We envision to grab a biological molecule of interest with an optical tweezer and overlap it with the atomic cloud. Our approach may also provide a unique way to atomic lithography with resolution well into the nanometer scale [91].

In the following chapter, we demonstrate the key idea behind this scheme. We observe the spatial localization of an atomic excitation through a spatially-varying atomic dark state.

Chapter 8

Demonstration of atom localization using Electromagnetically Induced Transparency[1]

8.1 Introduction

In chapter 7, we suggested an optical microscope that utilizes the nonlinear response of an atomic medium to achieve spatial localization not possible with tightly focused light alone. Considering again a Λ-scheme, if a standing-wave coupling laser is used to achieve spatially-dependent EIT throughout the atom cloud, the population of the excited Raman level can be very tightly localized near the intensity nodes. In this chapter, we present a proof-of-principle experiment that demonstrates the key ideas of this approach. By using ultracold rubidium (Rb) atoms in a magneto-optical trap (MOT) and pulsed coherent transfer, we demonstrate atomic localization to spots much smaller than the spatial period of the coupling-laser intensity profile. Although due to imaging limitations we have used a large spatial period in this work ($\approx 600~\mu$m), our results will likely scale to the sub-wavelength regime in the future. Li *et. al.* have experimentally demonstrated probe narrowing beyond the diffraction limit using a spatially-varying coupling laser profile in a vapor cell [93]. We observe similar amount of spatial localization while providing direct experimental evidence of the localization mechanism for the first time.

---

[1]A variation of this chapter can be found at Ref. [92]. Additional details are given in appendix chapter D.

8.2   Magneto-optical trap

Before outlining the specifics of our proof-of-principle experiment, we first describe the magneto-optical trap and ultrahigh vacuum apparatus. The localization scheme described here depends on exciting a very small spatial extent of atoms and then, at some time later, imaging these atoms. A complication arising from this scheme is that the atoms will thermally diffuse before or during imaging. In order to minimize this complication, we perform this experiment within a cloud of ultracold atoms. In the ultracold regime, the atoms are generally 6 orders of magnitude cooler than in the vapor cell regime described earlier. This translates to 3 orders of magnitude reduction in diffusion.

This ultracold atom cloud is achieved using a magneto-optical trap (MOT). We begin with a 14-port stainless steel vacuum chamber pumped down to 10^{-9} torr. We use a pair of magnetic field coils in the anti-Helmholtz arrangement, 250 turns each with a current of 0.5 amps, to obtain a magnetic field gradient of 8 gauss/cm at the center of the chamber. A set of three retro-reflected beams, 100 mW in the direction transverse to the magnetic field, and 50 mW in the longitudinal direction, is directed at the center of the chamber. A few grams of solid rubidium is placed in a valve-controlled vacuum flange, filling the chamber with rubidium vapor. The lasers locked to a frequency to the red of the electronic resonance. This means the atoms will be inundated with radiation pressure by the lasers when they are moving at high velocity towards any of the lasers, until the atoms are slowed down. Upon optimization of the various parameters (see appendix chapter D), the final atomic temperature is 150 μK.

The MOT beams are derived from a single master oscillator locked to the $|F = 2\rangle \rightarrow |F' = 2\rangle$ and then shifted blue 120 MHz, leaving it optimally detuned from the cycling transition of ^{87}Rb ($|F = 2\rangle \rightarrow |F' = 3\rangle$) by 2Γ. Its amplified to 1 Watt with an optical power amplifier, and then coupled into three fibers, one for each axis. The hyperfine repumper is derived from a separate laser diode which is locked to the $|F = 1\rangle \rightarrow |F' = 1 - 2 \text{ crossover}\rangle$. It is then shifted ~ 80 MHz blue to resonate with the $|F = 1\rangle \rightarrow |F' = 2\rangle$ transition. This latter beam couples into a fiber and then combines with a MOT beam axis, resulting in about 5 mW hitting the atoms.
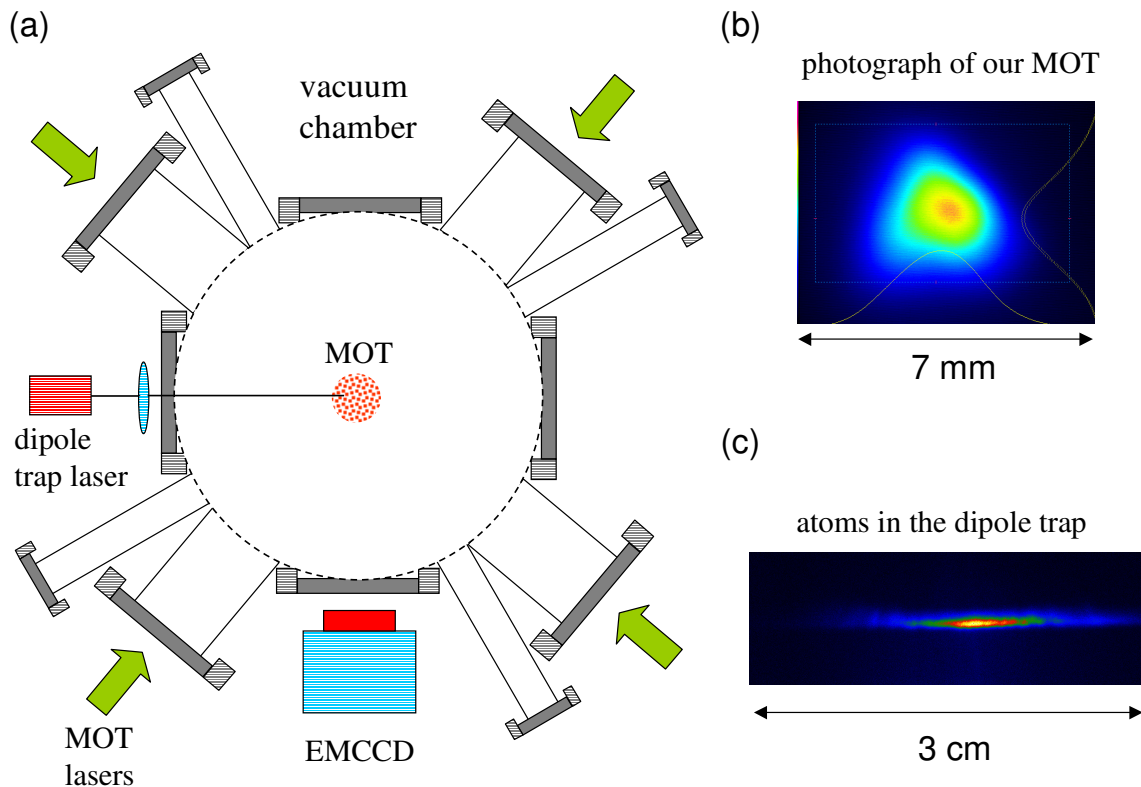
Figure 8.1 We use a stainless steel ultrahigh vacuum chamber for experiments shown here. The green arrows denote MOT beams. The localization experiments described here occur in the MOT. Our dipole trap measurements are discussed in the appendix.

8.3 Experimental setup

We next discuss the details of our experiment which can be viewed as a proof-of-principle demonstration of the suggestion by Lukin and colleagues [78]. The EIT beams are derived from a master diode laser which is saturated-absorption locked to the appropriate transition. The coupling laser beam is shifted by 6.8 GHz using high-frequency acousto-optic modulators and is amplified with a tapered amplifier [50]. As shown in Fig. 8.2, the probe and the coupling lasers are resonant with $|F = 1\rangle \rightarrow |F' = 2\rangle$ and $|F = 2\rangle \rightarrow |F' = 2\rangle$ transitions of the D_2 line, near a wavelength of 780 nm. The beams have the same circular polarization and the experiment works in three parallel m_F channels [94]. The coupling laser is split into two beams, which then reconverge at
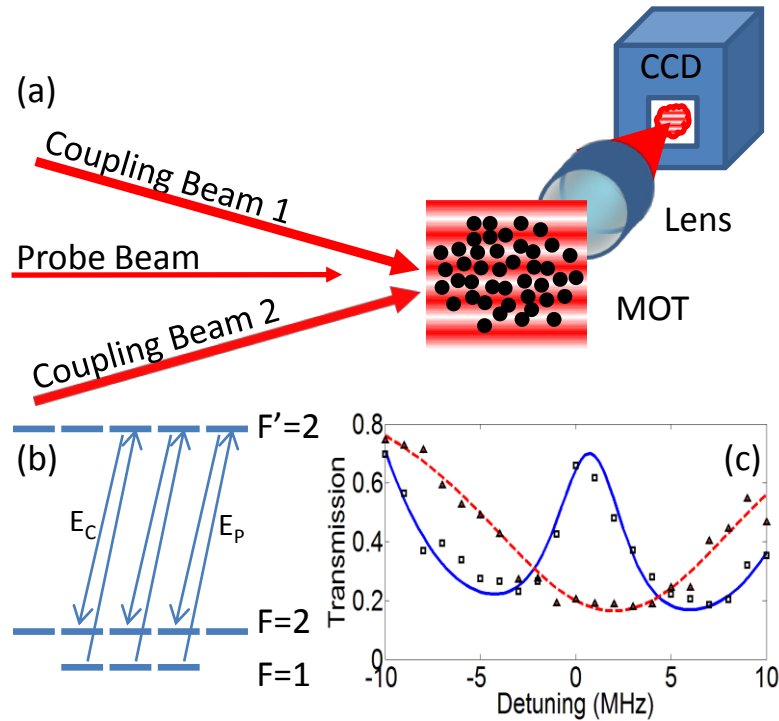
Figure 8.2 (Color online) (a) The schematic of our experiment. The experiment is performed in a magneto-optical trap (MOT) of ultracold ^{87}Rb atoms. With atoms starting in the $|F = 1\rangle$ hyperfine level, we drive the atoms to the dark state with a probe laser beam and a spatially-varying coupling laser beam. The spatial profile for the coupling laser is obtained by combining two identical beams at the MOT at an angle of 3 milliradians producing a vertical standing wave. The atomic localization is measured by taking fluorescence images with the CCD. (b) The relevant energy level diagram, with probe laser E$_P$ and coupling laser E$_C$. The experiment works with three parallel m_F channels. (c) Transmission of a weak probe beam ($\approx$ 100 nW power) through the cloud as a function of frequency with (solid blue line) and without (dashed red line) the coupling laser beam. We perform this measurement with Coupling Beam 1 at an intensity of 120 mW/cm^2 and do not use the standing-wave. The on-resonance transmission is about 70% demonstrating reasonably good EIT.

the MOT at an angle of 3 milliradians to form a vertical standing wave with a spatial period of $\Lambda = 600$ μm. We probe the localization by level-dependent fluorescence of the atomic cloud. The fluorescence signal is collected with a 2-inch achromatic-doublet outside of the vacuum chamber and is recorded with an electron-multiplying CCD camera.

Before proceeding further, we present a brief discussion of population localization using the dark state in the context of this experiment. Atoms distributed throughout the MOT will see different coupling laser intensities, based on where they are in the standing wave. Ignoring the complications due to parallel channels, the dark state of the atoms is given by [1, 70, 78]:

$$|\, \text{dark(x)}\rangle = \frac{\Omega_C(x)\, |F = 1\rangle - \Omega_P\, |F = 2\rangle}{\sqrt{\Omega_C(x)^2 + \Omega_P^2}}, \tag{8.1}$$

where Ω_P and Ω_C are the Rabi frequencies of the respective beams. Here, for simplicity, we assume the probe beam to be uniform. The atoms can be prepared in the dark state of Eq. (1) by using the well-known counter-intuitive pulse sequence with coupling laser turning on before the probe laser beam. Once the laser beams are turned on, they can be turned-off simultaneously preserving the ratio of the Rabi frequencies [70]. As a result, even after the laser pulses are turned-off, the atomic system is left in the state as determined by the probe and coupling laser Rabi frequencies at the temporal-peak of the pulses. Through this preparation, atoms will populate $|F = 2\rangle$ with a probability of $|\langle F = 2|\text{dark(x)}\rangle|^2 = \Omega_P^2 / [\Omega_C(x)^2 + \Omega_P^2]$. Due to the sensitive dependence to the coupling beam intensity, atoms located near a coupling field zero-crossing (intensity node) coherently transfer to $|F = 2\rangle$ with high probability. If we assume that $\Omega_C(x)$ is linear near a zero-crossing, then we expect the probability $|\langle F = 2|\text{dark(x)}\rangle|^2$ to be maximum at the coupling intensity node, and have an approximate spatial width of $\sim \Lambda \cdot \Omega_P/\Omega_{C0}$ where Ω_{C0} is the peak coupling laser Rabi frequency [70, 78]. As a result, with the probe laser intensity fixed, the population of level $|F = 2\rangle$ becomes more and more localized with increasing coupling beam power.

The experimental timing cycle is shown in Fig. 8.3. We begin the experiment by loading the MOT for one second and then turn off the MOT magnetic field gradient 50 ms prior to the EIT beams to reduce Zeeman splitting of the magnetic sublevels. All atoms are then initialized to $|F = 1\rangle$ by turning off the hyperfine repumping laser for the MOT. We drive the atoms to the dark state by using a 400 ns-long coupling laser and a 250 ns-long probe laser beam. After the EIT beams are turned-off, we probe the population of $|F = 2\rangle$ by fluorescing the atoms for 40 μs via the cycling transition ($|F = 2\rangle \rightarrow |F' = 3\rangle$). Due to sufficiently low atomic temperature, the motion of the atoms during fluorescence is negligible. In Fig. 8.3 we present two fluorescence
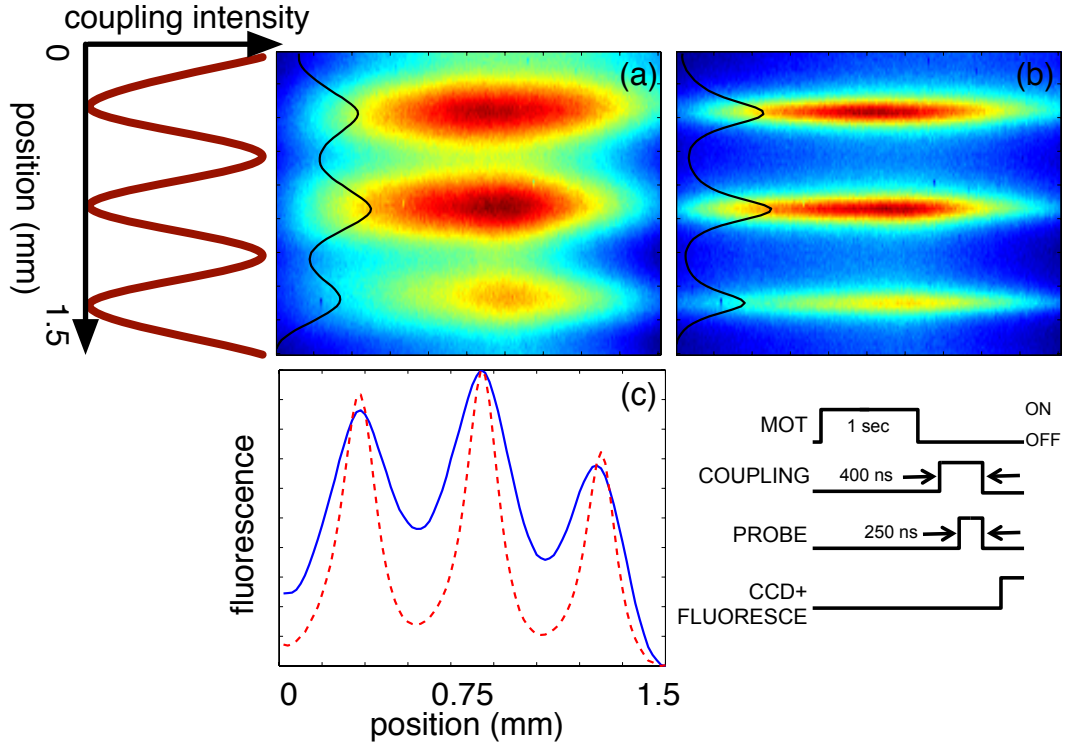
Figure 8.3 (Color online) Fluorescence images of the atomic cloud for (a) $I_{C0} \simeq 22 \times I_P$ and (b) $I_{C0} \simeq 418 \times I_P$. The images are obtained by fluorescing the $|F = 2\rangle$ level via the cycling transition after the EIT beams are turned-off. The fringes are confined to the intensity nodes of the coupling beam and become more localized as the intensity of the coupling laser increases. (c) shows horizontally-averaged line profiles of each fluorescence image for more direct comparison. The solid line is for part (a) and the dashed line is for part (b). The lower right diagram shows the experimental timing cycle.

images that show localization of the $|F = 2\rangle$ population as the coupling laser intensity is increased. Fig. 8.3(a) illustrates a case where we use a relatively weak coupling beam, where $I_{C0} \simeq 22 \times I_P$ (I_{C0} is the peak coupling intensity and I_P is the probe intensity). The fringes align with the nodes of the coupling beam intensity and have wide profiles in the vertical dimension. In Fig. 8.3(b), we use a nearly 20 times more intense coupling laser beam such that $I_{C0} \simeq 418 \times I_P$. We observe the fringes to be vertically much more tightly confined to the coupling beam nodes. Both pictures use a probe intensity of 3.9 mW/cm^2, and each picture is an average of 100 shots. Fig. 8.3(c) shows horizontally-averaged line profiles of each fluorescence image for more direct comparison.
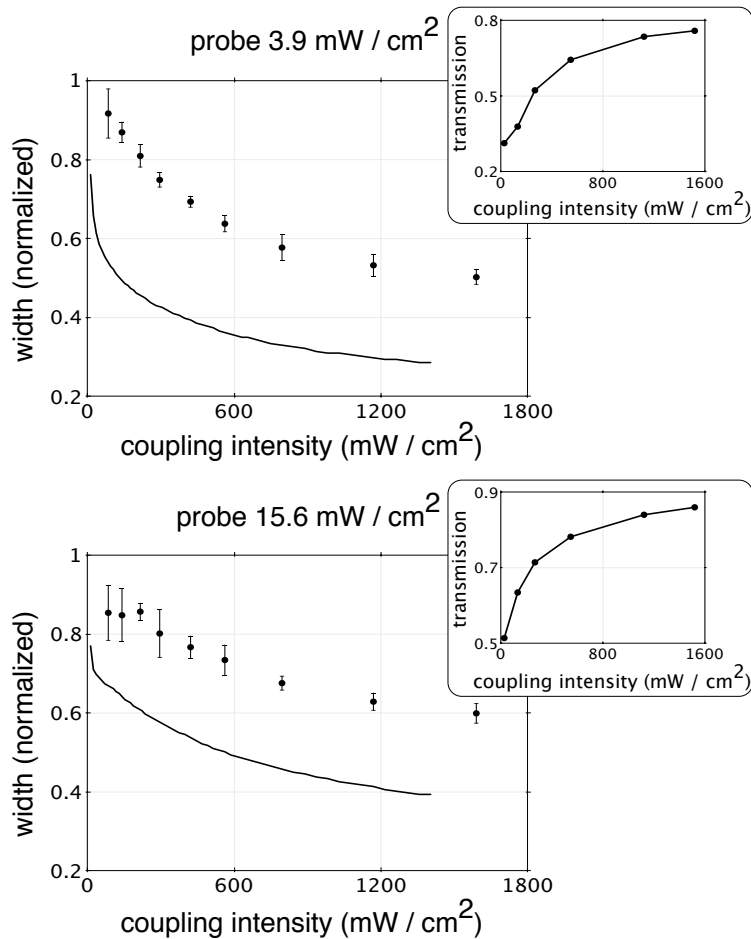
Figure 8.4 The width of the fringes as a function of peak coupling beam intensity for $I_P = 3.9$ mW/cm^2 and $I_P = 15.6$ mW/cm^2. The vertical scale is normalized such that one unit corresponds to a fringe width that equals half the spatial period (a sine wave). The population of $|F = 2\rangle$ becomes more tightly localized to the standing wave nodes with increasing coupling laser beam intensity. The data points are experimental observations and the solid lines are the result of a numerical simulation. We attribute the discrepancy between experiment and theory to various imperfections such as the mechanical jitter of the standing-wave pattern. See text for details. The insets show the integrated probe transmission through the cloud as the intensity of the coupling beam is increased. We observe increased transmission with increasing coupling intensity, demonstrating the presence EIT.

8.4   Experimental results

Figure 8.4 shows the normalized full-width-half-maximum (FWHM) of the fringes as the coupling beam intensity is varied for two values of probe laser intensity $I_P = 3.9$ mW/cm^2 and
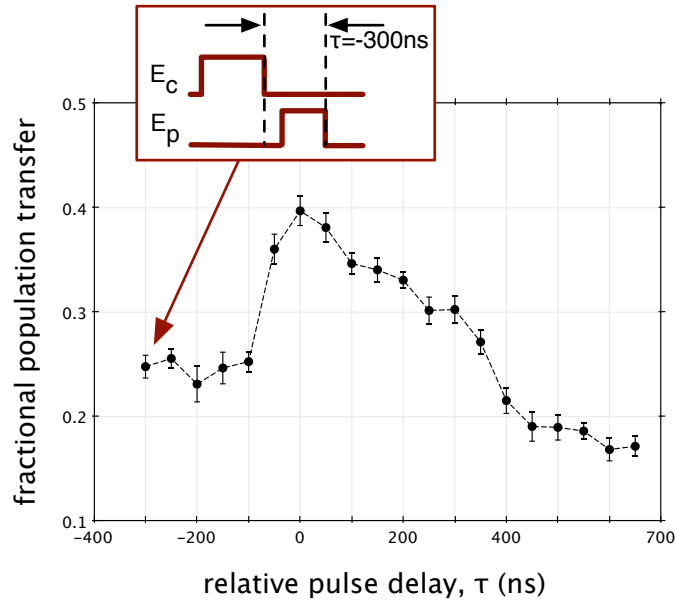
Figure 8.5 (Color online) Demonstration of stimulated Raman adiabatic passage (STIRAP). For this test, we initialize the atoms to level $|F = 1\rangle$ and probe the population of $|F = 2\rangle$ as the overlap between the EIT pulses is varied. We observe maximal population transfer to $|F = 2\rangle$ when the coupling and probe pulses completely overlap with coupling laser turning-on and turning-off before the probe laser beam.

$I_P = 15.6$ mW/cm^2. Each data point is an average of 100 images and the error bars show the standard deviation of each set. For $I_P = 3.9$ mW/cm^2, we observe the population of level $|F = 2\rangle$ to localize by about a factor of two as the coupling beam intensity is increased. The solid lines in Fig. 8.4 are the results of numerical calculations without any adjustable parameters (i. e. each parameter that goes into the simulations are experimentally measured). Here, we include all relevant magnetic sub-levels and numerically solve the time-domain density matrix equations for the conditions of our experiment. We have experimentally measured the standing-wave interference of the coupling laser beam to be slightly imperfect with intensity contrast of 98%. This imperfection is included in our numerical calculations. The disagreement between theory and experiment is likely a result of 1) mechanical and interferometric fluctuations of the standing-wave intensity profile of the coupling laser beam, and 2) the Zeeman shift of the magnetic-sublevels due to a residual background magnetic field.

8.5 Ground state coherence and STIRAP

We next discuss the coherent nature of population localization. The insets in Fig. 8.4 show the integrated probe transmission through the atomic cloud as the coupling beam intensity is increased. We see better probe transmission with increased coupling beam intensity, demonstrating EIT for the exact conditions of each localization experiment. Furthermore, we have the ability to probe excited state fluorescence during the EIT process by collecting scattered photons for the duration of the coupling laser beam. We observe a reduction in the excited state fluorescence as the coupling laser intensity is increased, complementing the probe transmission data of the insets of Fig. 8.4. We also observe a strong increase in the excited state fluorescence when the coupling laser beam is turned-off (probe laser propagating alone through the cloud). This further confirms that the atoms are driven to a dark state with a small population at the excited electronic level. We provide an expanded discussion of the mechanism behind localization in appendix chapter D.

To further test the coherent nature of the population transfer, we have also performed a stimulated Raman adiabatic passage (STIRAP) experiment [85]. We measure the population transfer to $|F = 2\rangle$ at the intensity peaks of the coupling laser using a pulse sequence similar to above, but by changing the relative temporal overlap between the EIT beams. Noting Fig. 4, as expected, the maximum transfer to $|F = 2\rangle$ occurs when the probe and coupling pulses overlap, with coupling laser turning-on and turning-off before the probe laser beam. We observe a 20% increase in population transfer when the two pulses overlap, consistent within a factor of two of our density-matrix calculations. Near the intensity nodes of the coupling laser, we observe approximately 10% increase in population transfer when the pulses overlap (not shown in Fig. 8.5). As mentioned earlier, there is a coupling beam intensity offset of 2% of the peak at the nodes due to an imperfect interference profile. To increase contrast, the STIRAP experiments of Fig. 4 use beams that are 12 MHz detuned to the blue of the excited state. The intensities of the two beams are $I_{C0} \approx I_P = 130$ mW/cm^2.

8.6   Conclusion

To summarize, we have demonstrated localization of level population using EIT. As mentioned before, because our imaging system cannot resolve sub-wavelength spatial scales, we have performed this experiment with a small-angle between the two coupling-laser beams and therefore with a large spatial period of the standing-wave interference pattern. Future work will include extending this technique to the sub-wavelength regime and possibly demonstrate nanometer scale localization and addressing of neutral atoms. Furthermore, by using more powerful laser beams, we aim to explore atomic localization at much faster time-scales. If successful, the ability to address atoms at sub-ns time-scales with sub-wavelength resolution may provide a powerful tool for many challenging problems including initialization and addressability of a neutral-atom quantum register [95, 96].

Chapter 9

Refractive index conditional phase-shifter in the far-off resonance regime[1]

9.1 Introduction and background

In this chapter, which is independent from the rest of this thesis, we suggest a conditional phase shifter that achieves a phase shift of π between two weak lasers with a total energy on the 1000-photon level. The two laser beams interact through the simple nonlinear technique of ac Stark shifting the common ground state of a V-type system. We analyze this system in the far-off resonance regime. We find that this switch can operate in the far-off resonant regime, with low absorption and high phase accumulation. Additionally, the bandwidth of this switch can be increased independently of energy requirement.

Interacting low-power laser beams is a subject of considerable attention in nonlinear and quantum optics [17, 98, 99]. Nonlinear interactions between weak beams can form optical switches with possible applications in all-optical information processing. Furthermore, if achieved at the single photon level, these interactions can also be used to entangle single photons, which may form the basis of a future photonic quantum computing device. In traditional nonlinear materials, the weakness of optical nonlinearities prohibit observing significant nonlinear effects between

---

[1]A variation of this chapter can be found in Ref. [97]. Additional details can be found at appendix chapter E.

weak beams. Over the last decade, suggestions involving EIT have generated much enthusiasm in this field [8, 10, 100–104]. Recent experiments have demonstrated optical switching at ~10 photons per atomic cross-section using EIT-based approaches [10, 105]. Additionally, switching with optical instabilities has been demonstrated in an atomic vapor at less than one photon per atomic cross-section [106].

As discussed earlier, it is well-known that an intense laser beam can modify the refractive index experienced by a weak co-propagating laser beam of a different frequency. If the two beams are tuned near the resonance of an atomic medium, the strong beam will modify the phase on the weak beam through the ac Stark shift [98, 99]. In this chapter, we consider the case where the two beams are far-off resonant and are at the 1000-photon level. We derive an expression that indicates a cross-phase modulation on the order of radians can be obtained with high bandwidth and low absorption. These findings indicate that the scheme detailed here could operate as a simple, fast all-optical switch. Despite its simplicity, an extensive review of the literature finds that an analysis of this scheme is missing.

Before describing the scheme in detail, we note the several advantages of this approach when compared to similar optical switches utilizing other approaches: 1) This scheme does not require a strong coupling laser as is required by EIT. As a result, the total energy requirement of our switch is at the 1000-photon level. 2) The bandwidth of our switch can be large and one can work with nanosecond time scale optical pulses. The bandwidth can be increased until the rotating-wave approximation breaks down at the expense of an increased density-length product. 3) For sufficiently large detuned beams, Doppler broadening becomes unimportant and as a result, our scheme is well suited for vapor cells. Due to these advantages, our approach may be particularly useful for constructing ultra-low power, high-bandwidth all-optical switches with possible applications in current fiber-optic networks.
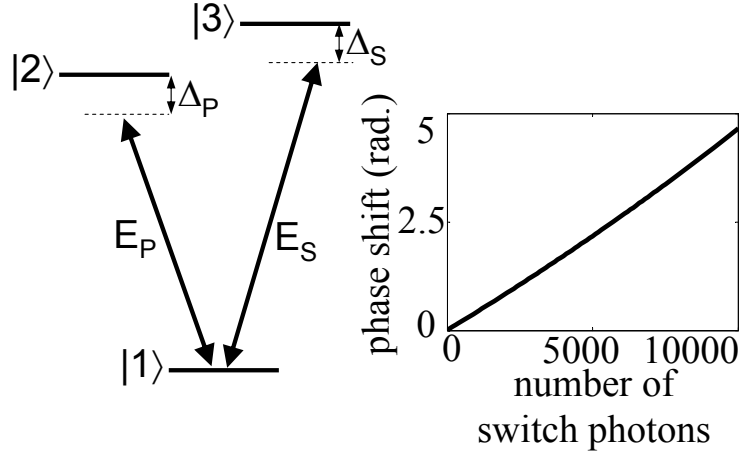
Figure 9.1 A switch beam, E_s, causes a nonlinear phase shift on a probe beam, E_p. The two beams travel collinearly through a V-type atomic medium. By itself, the probe accumulates phase based on the linear susceptibility of the atoms. When the switch beam is turned on, the common ground state $|1\rangle$ experiences an ac Stark shift, changing the effective detuning. The plot indicates that ~ 5000 switch photons are required for a phase shift of π radians on the probe.

9.2 Description of switch

As shown in Fig. 9.1, we begin with a neutral alkali atomic medium containing a ground state $|1\rangle$ and two excited states, $|2\rangle$ and $|3\rangle$. A probe beam, E_p, and a switch beam, E_s, are tuned far-off resonant from the $|1\rangle$–$|2\rangle$ and $|1\rangle$–$|3\rangle$ transitions, respectively[2]. Without the switch beam, the weak probe laser will experience phase accumulation and absorption as determined by the linear susceptibility of the atomic medium. These quantities depend on the probe's frequency detuning from the atomic resonance, Δ_p. When both the probe and switch propagate together through the medium, the detuning of the probe effectively changes. This is because the switch beam will ac Stark shift the common ground state $|1\rangle$. In the presence of the switch beam, the susceptibility of the medium is modified to give:

$$\chi_p = \frac{N\mu_{12}^2}{\hbar\epsilon_0} \frac{1}{2(\Delta_p + \delta_s) + i\Gamma}, \tag{9.1}$$

---

[2]In general, this phase-shifter scheme is not exclusive to V-systems. For example, one may tune both beams to the same lower and upper states in a two-level scheme. Then, the switch beam will ac Stark shift both the lower and upper states.

where $\delta_s = \frac{\Omega_s^2}{4\Delta_s}$ is the ac Stark shift of the ground state, Ω_s is the Rabi frequency of the switch beam, N is the atomic density, μ_{12} is the dipole matrix element between states $|1\rangle$ and $|2\rangle$, and Γ is the transition linewidth. In the perturbative limit where $\delta_s \ll \Delta_p$, the nonlinear interaction between the switch and the probe can be described with a third order $\chi^{(3)}$ susceptibility by expanding Eq. (9.1). The polarization of the atomic medium at the probe laser frequency is then $P_p = \epsilon_0 \chi^{(1)} E_p + \epsilon_0 \chi^{(3)} E_s^* E_s E_p$. In the ideal case of pure radiative broadening of the excited states, and in the limit where the detunings are much larger than the linewidth ($\Delta_p, \Delta_s \gg \Gamma$), the conditional phase shift (CPS) and absorption of the probe beam is:

$$\text{CPS} \simeq n_s \left(\frac{3}{8\pi}\right) \left(\frac{\lambda_s^2}{A}\right) \left(\frac{1}{\tau\Delta_s}\right) \left(\frac{\Gamma}{\Delta_p}\right) \phi^{(1)}$$

$$\text{absorption} \simeq \left(\frac{\Gamma}{\Delta_p}\right) \phi^{(1)}. \tag{9.2}$$

Here, n_s is the number of photons in the switch pulse and $\phi^{(1)} = \left(\frac{\omega_p}{2c}\right) N\Re(\chi^{(1)})L$ is the usual probe phase accumulation in the absence of the switch beam (L is the length of the medium). In Eqs. 9.2, λ_s is the wavelength of the switch field, A is the spatial cross-sectional area of the two beams, and τ is the pulse duration of the two beams (for simplicity we take the two beams to have the same temporal profile and assume them to be focused to the same size). To avoid significant reshaping of the beams, we must choose the bandwidth of the beams to be much smaller when compared with the detunings, $1/\tau \ll \Delta_p, \Delta_s$. From Eqs. 9.2, for a high transmission of $> 50\%$ and for the ideal case of $A \sim \lambda^2$, a CPS of π radians requires a few thousand photons.

9.3 Numerical examples

The plot in Fig. 9.1 shows a numerical example based on Eq. (9.1). Here we use parameters that are typical for alkali atoms: wavelength $\lambda = 780$ nm and decay rate $\Gamma = 2\pi \times 6$ MHz. We take $\Delta_p = \Delta_s = 160\Gamma$, $NL = 1.5 \times 10^{13}$ cm^{-2}, $\tau = 20$ ns, and assume the ideal case of $A = \lambda^2$. With such tight focusing, propagation over long distances can, for example, be accomplished inside a hollow photonic crystal fiber [107]. For these parameters, the transmission of the probe beam at the end of the medium is 60 %. We find a CPS of π radians on the probe beam for a switch pulse containing 5000 photons. As we will discuss below, exact numerical calculations verify
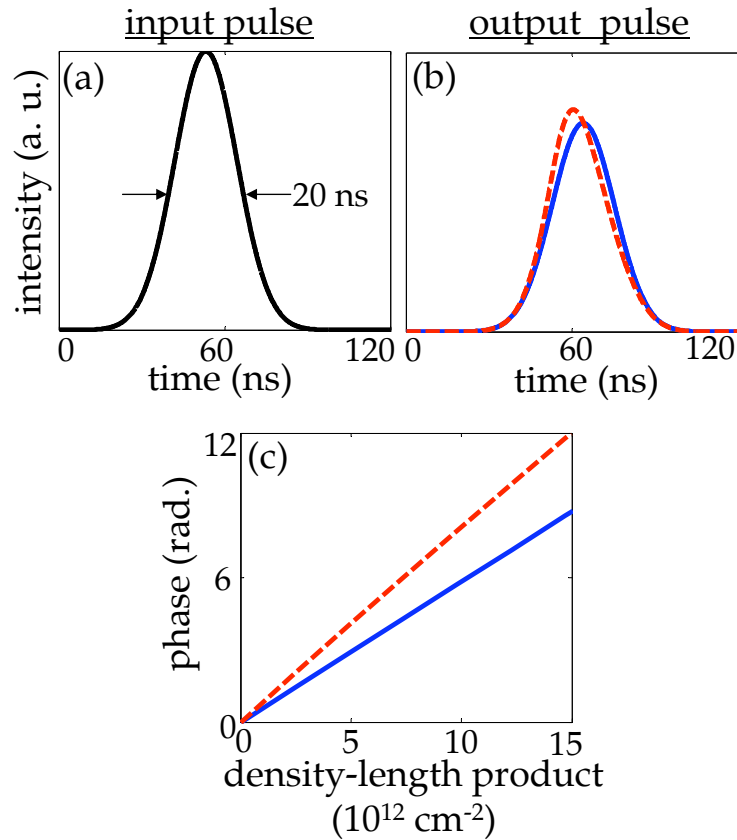
Figure 9.2 Numerical simulation of probe beam interacting with switch beam in an atomic medium. (a) shows the input probe pulse. (b) shows the resultant probe pulse in the case that the switch is off (blue, solid line) and on (red, dashed line). (c) shows the probe pulse phase accumulation as a function of distance both with the switch off (blue, solid line) and with the switch on (red, dashed line). The switch pulse (not shown here) has a matching pulse-shape and frequency detuning. This means the pulses stay matched throughout the interaction.

these results and demonstrate insignificant reshaping of the beams while propagating through the medium.

We proceed with a numerical study of the system. We neglect Doppler broadening and colli-sional effects and begin with a Hamiltonian describing a closed, three-level V-system in local time

$$t' = t - z/c$$

$$\mathcal{H} = \hbar \begin{pmatrix} 0 & -\frac{\Omega_p(z,t')}{2} & -\frac{\Omega_s(z,t')}{2} \\ -\frac{\Omega_p(z,t')^*}{2} & \Delta_p & 0 \\ -\frac{\Omega_s(z,t')^*}{2} & 0 & \Delta_s \end{pmatrix}. \tag{9.3}$$

We then use the commutator and anticommutator relations to find the equation of motion for the three-by-three density matrix ρ [17]:

$$\dot{\rho} = -\frac{i}{\hbar}[\mathcal{H}, \rho] - \frac{1}{2}\{\Gamma, \rho\}. \tag{9.4}$$

The values of ρ_{ij} calculated in Eq. (9.4) are used to numerically integrate the slowly varying envelope Maxwell's equations governing the propagation of the probe and switch fields,

$$\frac{\partial \Omega_p(z, t')}{\partial z} = -\frac{i}{\hbar}\eta\omega_p N\mu_{12}^2\rho_{12}(z, t')$$

$$\frac{\partial \Omega_s(z, t')}{\partial z} = -\frac{i}{\hbar}\eta\omega_s N\mu_{13}^2\rho_{13}(z, t'), \tag{9.5}$$

where $\eta = \sqrt{\mu_0/\epsilon_0}$ is the impedance of free space. We solve Eqs. (9.4) and (9.5) with the initial condition that all atoms are in ground state $|1\rangle$. At the start of the atomic medium ($z = 0$) we apply a boundary condition that the fields, and therefore the Rabi frequencies $\Omega_p(z = 0, t')$ and $\Omega_s(z = 0, t')$, are long Gaussian envelopes with a Gaussian width of τ. Eqs. (9.4) and (9.5) are then solved on the space-time grid using the method of lines.

The results are presented in Fig. 9.2 and demonstrate a phase-shift of 3.2 radians with 60% transmission. In this simulation, we use the same parameters as the plot in Fig. 9.1 and use $n_s = 5000$ photons in the switch beam. We observe smooth time-profiles at the end of the medium demonstrating negligible reshaping. Since the probe and the switch beam have identical detunings from the excited state, the switch pulse (not plotted) experiences near-identical absorption and reshaping. Furthermore, the two beams propagate with the same group velocity and therefore stay spatially and temporally well-matched while propagating through the medium. Despite the high beam intensity due to the tight focus, we point out that the atoms remain mostly in the ground state, and the perturbative condition is satisfied. This means that the saturation intensity is not a relevant figure.
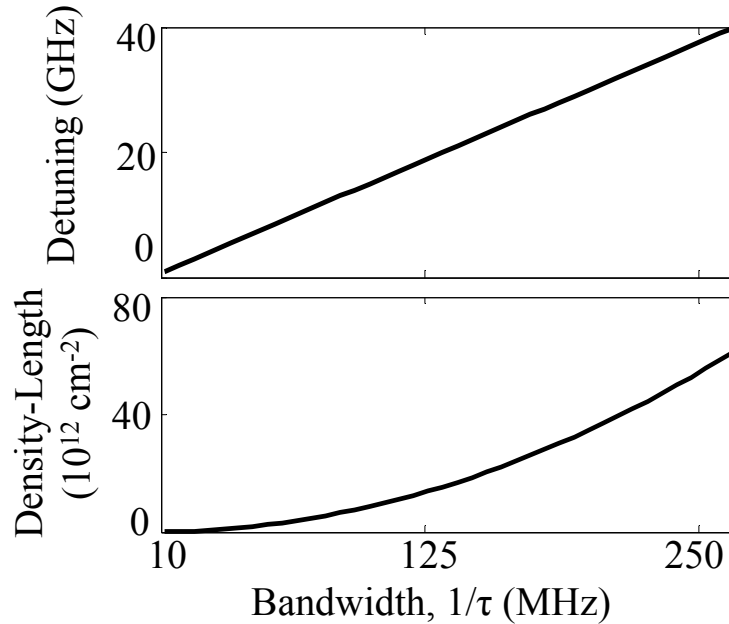
Figure 9.3 The probe and switch pulses can be made shorter, broadening the bandwidth, at the expense of density-length product. As the bandwidth is broadened, the detuning must increase to avoid near-resonant effects. If the density-length product is appropriately increased, identical results in transmission and phase-shift are obtained. Since faster pulses result in higher intensity for the same energy, the required number of switch beam photons does not change.

Finally, we note that the energy, or number of switch photons, required for this phase shifter is independent of bandwidth. Fig. 9.3 shows the required detuning and the density-length product for a given bandwidth that achieves the same performance as the numerical simulation of Fig. 9.2 (a CPS of $\sim \pi$ radians for $n_s = 5000$ switch photons). As the bandwidth broadens, both the probe and the switch must be appropriately detuned to avoid near-resonance effects. As noted in Eq. (9.2), the increased switch detuning is compensated by the shortened pulse duration (increased bandwidth), which means the switch pulse is more intense for the same energy. The increased probe detuning trades off with an increased density-length product to keep the probe transmission constant. The density-lengths required for a fast (>100 MHz) phase shifter in a typical alkali atom have been achieved in cold atom traps and optical fibers containing rubidium vapor [86, 107].

9.4 Conclusion

In summary, we suggested a far-off resonant scheme that supplies a conditional phase shift of π radians with energies at the 1000 photon level. To the best of our knowledge, the phase shifter presented here is among the simplest of those suggested in the literature. As mentioned before, a possible application of our suggestion is to all-optical information processing. With our approach, it should be possible to construct an all-optical switch with a switching time approaching 1 nanosecond at a total energy cost of less than 1 femtojoule per switching event. Furthermore, by using a cavity of a finesse of about 1000, our approach may achieve switching at the single photon level. If the switch beam can be supplied by a single photon, then the suggestion described here may be applicable as a single-photon controlled-NOT gate between the probe and the switch. This will be among our future investigations.

Chapter 10

Conclusions

The imaging problem is a major obstacle to researchers in fields across the scientific spectrum. But this problem is appears more surmountable with each passing decade. This thesis presents new experimental suggestions and results to contribute to solving this problem. In chapters 2-6, we describe and demonstrate new methods to manipulate the nonlinear index of refraction of rubidium vapor. A proof-of-principle experiment is described that achieves a refractive index of 10^{-5} in rubidium vapor, and we discuss potential routes to improve on this figure. In chapters 7 and 8 we suggest and experimentally demonstrate a new scheme to localize atoms, using EIT. We combine the propagation of light with the nonlinear response of atoms determined to double the traditional optical resolution. A major goal for both of these schemes is to image a sample such as a carbon nanotube with resolution better than the vacuum wavelength of the probing light.

In addition to contributions in imaging sciences, several of the experimental demonstrations described here are novel applications of nonlinear optics, advancing the current state of the art in the field. Nonlinear optical techniques such as electromagnetically induced transparency have been utilized for a wide range of applications. With this thesis we demonstrate the entirely new use of EIT for sub-diffraction limit imaging. As noted earlier, this has applications not only in biological sciences, but also in experimental physics where optical addressing and measurement with high spatial accuracy can be crucial.

Future extensions of this work will demonstrate new ways to utilize these tools. For example, it was recently suggested that an all-optical distributed Bragg reflector can be generated in a gas using refractive index enhancement [108]. This requires a periodic variation in the index of refraction of a gas (easily done with standing-wave control beams). For modest parameters in ultracold atoms, the predicted result is better than 99% reflection of the probe beam.

Equally exciting is the prospect producing a gas with negative refractive index at optical frequencies. The key idea is to combine our refractive index enhancement scheme, which enhances or suppresses the electric permittivity ϵ of a medium, with a method for manipulating the magnetic permeability μ [109]. Since this scheme allows for the probe laser to be far detuned from an electrical resonance (at the expense of control beam intensity), the probe may be tuned to a *magnetic* optical resonance. Such a scheme is among the most experimentally realizable methods to produce a gas exhibiting negative refractive index.

While numerous technical and theoretical challenges must be surmounted before such broad goals may be achieved, there are a number of major scientific milestones that will be reached along the way. Sometimes when a new scientific discovery is made, the way in which it will affect disciplines far and wide is unpredictable. Likewise, the most exciting part about the experiments and suggestions presented here the possibility that they will contribute to fields across physics and beyond.

Appendix A: Optical Setup Details

A.1   Introduction

In this chapter, we expand on the optical apparatus described in chapter 3 and discuss additional engineering details of the diode laser and tapered amplifier constructions.

A.2   Diode Laser

We have the most success using a relatively inexpensive ThorLabs laser diode (L785P100) which after feedback provides about 50 mW of output power. We combine this with an Edmund Optics diffraction grating to form a Littrow cavity that has a $\sim$1 MHz linewidth and 5 GHz mode-hop-free scanning range.

We have also experimented with Newport gratings as suggested in Ref. [64]. While these gratings were successful, they are about three times the cost of the Edmund Optics gratings, and in our experience tend to burn out laser diodes over a period of months. The actual working operation of them was about equal to the Edmund Optics gratings.

An eye towards the future suggests that we explore simple modifications that may provide kHz level linewidths, as outlined in Ref. [110]. This modified setup involves a grating-less optical cavity that includes a narrow bandpass interference filter to provide wavelength selection than a grating alone. Key questions that need to be explored include long-term stability and ease of providing active feedback.

A.3   Tapered amplifier

Fig. A.1 depicts the details of tapered amplifier housing. In the left picture, the two aluminum lens control pieces are shown. An aspherical lens (ThorLabs C230TME-B, f=4.51mm) is mounted on either side of the gain chip and the system is designed to provide micron-precision control of each asphere. The aluminum piece with larger outer-diameter is the Lens Control Mount. With coarse threads on the outside and very fine threads on the inside, this piece mates into the copper

block. It is held in place in the copper block by a set-screw. The asphere itself is mounted into the inside of the smaller-diameter piece, the Lens Control Handle; this piece is threaded to accept a ThorLabs mount. The Lens Control Handle is mated into the Lens Control Mount, and is twisted until its position is fine-tuned (see procedure, below). The fine threading on the outside of this piece is what makes the micron resolution possible. When the asphere positions are optimized, a set screw holds the piece in place (not seen in pictures; the set screw is located in the grip of the larger piece).

Procedure for optimizing optical coupling

1. Install the output-side asphere.

2. Approximately collimate the output ASE.

3. Install the input-side asphere, and seed the TA with 1mW of light.

4. Optimize the input-side asphere longitudinal position by twisting the Lens Control Handle and monitoring the output power. Note that some re-walking of the seed light might be necessary each time the longitudinal position is changed.

5. When finished, tighten the set screw located in the grip of the Lens Control Mount that clamps the body of the Lens Control Handle into place.

Finally, note that it is important to keep the tapered amplifier chip electrically isolated from aluminum heat sink. This is because current passes through the copper block, into the T.A. chip, then out through the chip's single lead. This diagram shows that the copper mount (top) is fastened to a copper baseplate with metal 8-32 screws. The baseplate sits on top of a TEC, and is fastened to the aluminum heat sink with plastic 8-32 screws. The TEC and the plastic screws electrically isolate the chip from the base.
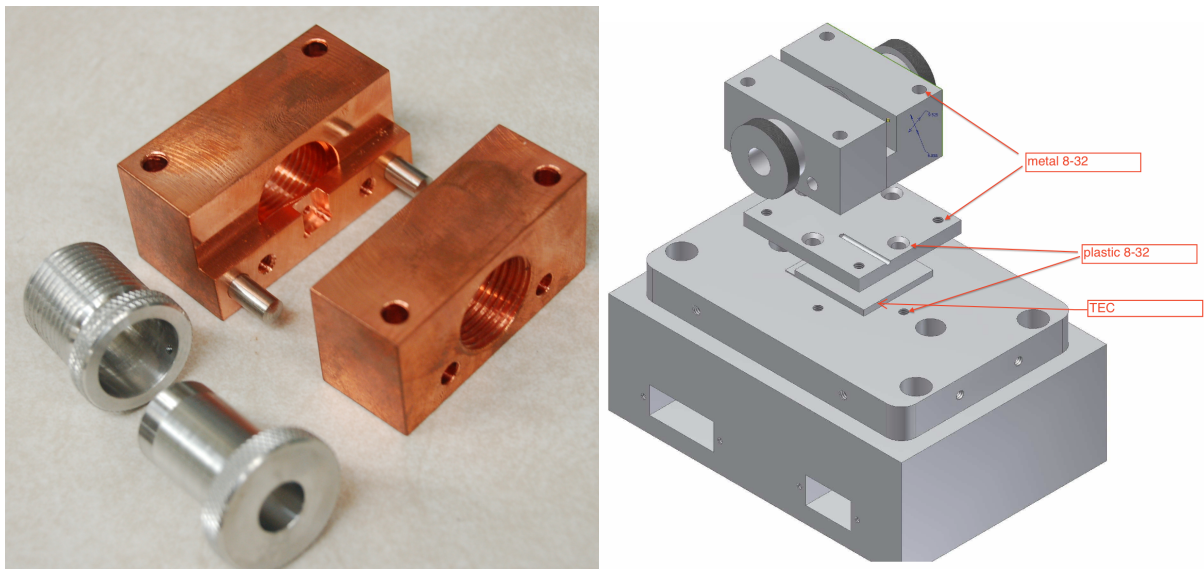
Figure A.1 Construction of the tapered amplifier housing. In the photograph (left), an asphere is installed in the lower aluminum collimation tube, which then mates with fine threading into the larger aluminum tube. The larger aluminum tube then coarsely mates into the copper piece. The fine threading provides control over the focusing of the seed light, and collimation of the output.

Appendix B: Refractive Index Enhancement Details

B.1   Introduction

Our efforts at achieving an enhanced refractive index are ongoing. Chapters 4 and 5 discuss our group's proof-of-principle experiment and continuing effort. In this appendix, we wish to highlight theoretical restrictions on how far the index of a gas can be enhanced. Additionally, we draw attention to the connection between our experiment and four-wave mixing.

B.2   Motivation of probe susceptibility in a Raman medium

In this section, we briefly motivate the susceptibility of a Raman medium, Eq. 2.4. Since a complete general derivation of refractive index enhancement is given in Ref. [13], here we will simply highlight useful relations, with approximations made that are in line with our experimental parameters. Considering Fig. B.1, we want to find the polarization of the probe beam in a system prepared with two strong control beams. The two strong control beams, E_{c1} and E_{c2} provide probe amplification and probe absorption, respectively, through two-photon Raman resonances. Since all beams are detuned far-off resonance, we ignore depletion of the ground state due to the strong control laser beams. Additionally, we ignore the single-photon susceptibility of the excited Raman levels, $|1\rangle$ and $|2\rangle$, to the probe field, since these levels are mostly unpopulated. We then write
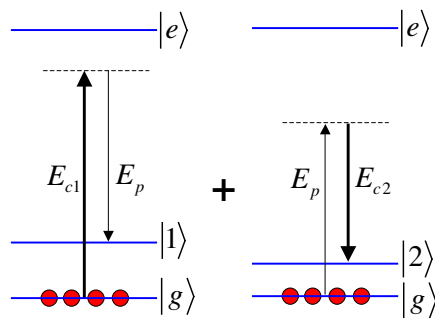

Figure B.1 General schematic of the refractive index enhancement scheme. The Raman transition to $|1\rangle$ through E_{c1} amplifies the probe beam. Similarly, the Raman transition to $|2\rangle$ through E_{c2} induces probe absorption.

down the polarization of the system at the probe frequency as

$$P_p = 2\hbar N(a_p|c_g|^2 E_p + b_1 c_g^* c_1 E_{c1} + b_2^* c_g c_2^* E_{c2}). \tag{B.1}$$

In the above equation, the variables are defined as follows (dropping the rotating terms):

$$
\begin{aligned}
a_p &= \frac{\mu_{ge}\mu_{ge}^*}{(\omega_e - \omega_g) - \omega_p - j\Gamma_e} \\
b_1 &= \frac{\mu_{ge}\mu_{1e}^*}{(\omega_e - \omega_g) - \omega_{c1} - j\Gamma_e} \\
b_2 &= \frac{\mu_{ge}\mu_{2e}^*}{(\omega_e - \omega_g) - \omega_{c2} - j\Gamma_e}
\end{aligned} \tag{B.2}
$$

We can find the probability amplitudes c_g, c_1, and c_2 by solving the differential equations,

$$
\begin{aligned}
\frac{\partial c_g}{\partial t} &= j\frac{B_1}{2}c_1 + j\frac{B_2}{2}c_2 \\
\frac{\partial c_1}{\partial t} + j\delta\omega_1 c_1 + \left[\gamma_1 + \frac{\mathfrak{J}(D_1)}{2}\right]c_1 &= j\frac{B_1^*}{2}c_g \\
\frac{\partial c_2}{\partial t} + j\delta\omega_2 c_2 + \left[\gamma_2 + \frac{\mathfrak{J}(D_2)}{2}\right]c_2 &= j\frac{B_2^*}{2}c_g
\end{aligned} \tag{B.3}
$$

where,

$$
\begin{aligned}
B_1 &= b_1 E_{c1} E_p^* \\
B_2 &= b_2 E_p^* E_{c2}
\end{aligned}
$$

$$\tag{B.4}$$

In Eqs. B.3, we have already incorporated ac Stark shifts due to the strong control beams into the two photon detunings from states $|1\rangle$ and $|2\rangle$, $\delta\omega_1$ and $\delta\omega_2$ respectively. Additionally, we drop terms which cause depletion of the ground state, which is negligible in our experimental regime. The terms $\mathfrak{J}(D_1)/2$ and $\mathfrak{J}(D_2)/2$ describe broadening of the energy levels due to a non-negligible imaginary part of the ac Stark shift. They place an upper limit on how intense we can make the control beams, as described in chapter 2.

We set $|c_g|^2 \approx 1$ and assume the steady-state approximation by setting the time derivatives to zero. We then solve for c_1 and c_2 and find that

$$
\begin{aligned}
c_1 &\approx \frac{B_1^*}{2\{\delta\omega_1 - j[\gamma_1 + \mathfrak{J}(D_1)/2]\}} \\
c_2 &\approx \frac{B_2^*}{2\{\delta\omega_2 + j[\gamma_2 + \mathfrak{J}(D_2)/2]\}}.
\end{aligned}
\tag{B.5}
$$

We can plug Eq. B.5 into Eq. B.1 and find the expression for the generated dipole moment at the probe frequency,

$$
\begin{aligned}
P_p = 2\hbar N \Bigg(a_p \ &+ \ \frac{|b_1|^2}{2[\delta\omega_1 - j(\gamma_1 + \mathfrak{J}(d_1)|E_{c1}|^2)]}|E_{c1}|^2 \\
&+ \ \frac{|b_2|^2}{2[\delta\omega_2 + j(\gamma_2 + \mathfrak{J}(d_2)|E_{c2}|^2)]}|E_{c2}|^2 \Bigg) E_p.
\end{aligned}
\tag{B.6}
$$

Using the definition of linear susceptibility, $P_p = \epsilon_0 \chi E_p$, we can then solve for Eq. 2.4.

B.3 Derivation of noise: a semiclassical approach

In order to utilize the refractive index enhancement scheme discussed here with an ultra-low probe intensity (less than L/λ_0 photons, where L is the length of the medium), we must first consider how much noise is added to the probe beam. Operating in such a regime could be useful for an ultra-low-intensity all-optical phase gate [111] or an all-optical distributed Bragg reflector [108].

The presence of an amplifying resonance leaves open the possibility of amplified spontaneous emission. The source of this noise can be derived using two different approaches. In the first approach, we take the electromagnetic fields to be quantized, and noise is generated when a vacuum fluctuation occurs whose mode is within the gain region of the susceptibility, becoming amplified. An analysis of noise approached by solving the Heisenberg equations of motion can be found in Ref. [112]. The result is that the number of noise photons added to the beam after traveling through the medium is

$$
n_{noise} = (n - 1)\left(\frac{2\pi}{\lambda_0}\right) L
\tag{B.7}
$$

Note that this is simply the phase accumulated by the probe beam due to index enhancement; in other words, the number of noise photons is simply equal to the number of radians accumulated. We define this phase to be Φ_{max}, since the system is optimized for maximum index enhancement.

The second approach considers how the atomic system responds to continuous-wave electromagnetic fields. We outline the derivation here as it is not discussed elsewhere.

Before going into detail, we outline the approach. We first find that some small fraction of ground-state atoms are excited to the excited state by the control beam. This fraction is small since the control beam, while intense, is far-detuned from the resonance. When excited atoms decay, photons will spontaneously emit into random directions with random polarizations. The fraction of photons that emit into the probe beam solid angle, with the probe polarization and frequency, are technically indistinguishable from the probe signal and are therefore treated as noise. This is the figure that we set out to find.

The excited state probability amplitude is c_e and population is $|c_e|^2$. The fraction of atoms excited by the coupling beam is

$$|c_e|^2 = \frac{|\Omega_c|^2}{|4\Delta_c|^2} \tag{B.8}$$

where Ω_C is the Rabi frequency of the couling beam, $\Omega_C = \mu_{ge}E_C/\hbar$ and Δ_C is the single-photon detuning of the coupling beam (not to be confused with Δ, the separation of the Raman resonances). The spontaneous emission rate is then

$$r \equiv \frac{|\Omega_c|^2}{|4\Delta_c|^2}\Gamma_e. \tag{B.9}$$

Next we want to understand how the spontaneous emission decay rate r is related to how much phase the probe beam accumulates due to the enhanced refractive index. Assuming $\Delta_c \gg \Gamma_e$, the coupling constants for either of the control beams, defined above in Eqs. B.2 simplify to

$$b = \frac{1}{2\hbar^2}\frac{\mu_{ge}^2}{\Delta_c}. \tag{B.10}$$

If the absorptive and amplifying resonances of the probe and control beam are separated by $\Delta = 2\gamma$, such that the enhancement of the index of refraction is maximized, then the phase accumulated

by the probe accumulated by the probe is Φ_{max}, and is equal to

$$\Phi_{max} = \frac{\hbar\omega}{2c\epsilon_0\gamma}|b|^2|E_C|^2NL \tag{B.11}$$

$$= \frac{\hbar\omega}{2c\epsilon_0\gamma}\left(\frac{\mu_{ge}^2}{2\hbar^2\Delta_C}\right)^2|E_C|^2NL \tag{B.12}$$

$$= \left(\omega\mu_{ge}^2\right)\left(\Omega_C^2\right)\left(\frac{NL}{2c\epsilon_0\gamma4\Delta_c^2\hbar}\right) \tag{B.13}$$

where ω is the angular frequency of the probe beam, and N and L are the density and length of the medium, respectively. By writing the prefactor $\left(\omega\mu_{ge}^2\right)$ in terms of the excited state linewidth using the Wigner-Weisskopf approximation and doing some algebra we find

$$\Phi_{max} = \left(\frac{3}{8\pi}\right)\left(\frac{\lambda^2}{\gamma}\right)\left(\frac{\Omega_c^2}{4\Delta_c^2}\Gamma_e\right)NL. \tag{B.14}$$

Therefore, the spontaneous emission decay rate is

$$r = \left(\frac{8\pi}{3}\right)\left(\frac{\gamma}{\lambda^2}\right)\left(\frac{1}{NL}\right)\Phi_{max}. \tag{B.15}$$

Note that r is merely the single atom decay rate. We define the total spontaneous emission rate of the entire sample as $R \equiv NALr$, where A is the cross-sectional area of the interaction region. We then find that the broadband spontaneous emission rate for the sample into all 4π steradians, with all polarizations is

$$R = \left(\frac{8\pi}{3}\right)\left(\frac{A}{\lambda^2}\right)\gamma\Phi_{max}. \tag{B.16}$$

.

If we focus the probe to an area A, then it diverges into an angle $\lambda/\sqrt{\pi A}$. Therefore we spatially filter the spontaneous emission photons by a fraction of $\lambda^2/\left(\pi^2 A\right)$ of the total 4π solid angle. Also, since we know the polarization of the probe, we can filter out the 50% of the noise in the wrong polarization. The spontaneous emission rate into the probe spatial mode and polarization is then

$$R_{probe} = \frac{\gamma\Phi_{max}}{3\pi} \tag{B.17}$$

Finally, we can filter out the probe using frequency information. If the probe is on for a time τ, then the probe frequency has a spectral bandwidth of approximately $1/\tau$. Since the spontaneously

emitted photons have spectral width γ, we can set up a cavity with a linewidth $1/\tau$ that filters out a fraction of $1/(\gamma\tau)$ of the noise. The number of noise photons emitted into the probe beam is then

$$n_{noise} = \Phi_{max}/(3\pi). \tag{B.18}$$

Note that using the Heisenberg-Langevin approach, as noted earlier, we find that $n_{noise} = \Phi$. The semiclassical approach differs by about a factor of 10, but also uses a number of approximations.

B.4 Four wave mixing

When the probe beam is tuned to the Raman resonance induced by a control beam, a coherence is set up between the two ground states. This allows for higher-order effects such as four-wave mixing. Here, the medium has a strong polarization at $\omega_{FWM} = 2\omega_C - \omega_P$, spontaneously generating a laser beam at this frequency. We consider four wave mixing an undesired side effect of the refractive index enhancement experiment but also note the generated beam is negligible in our usual experimental regime.

To calculate prominence of four-wave mixing in our experiment, first consider how much the probe beam is amplified as it propagates through the gas. If we assume a single amplifying Raman resonance, and the probe tuned to the two-photon resonance, then probe beam amplification is described by

$$\begin{aligned}
2ik\frac{\partial E_P}{\partial z} &= -\mu_0\omega^2 \cdot P \\
&= -\mu_0\omega^2 \cdot b^2 \frac{E_C^2}{2\delta\omega - i\gamma}E_P \\
\frac{\partial E_P}{\partial z} &= G \cdot E_P
\end{aligned} \tag{B.19}$$

We define the constant G as a gain coefficient. This coefficient is used to calculate both the amplification or absorption of the probe, and the power of the generated four wave mixing beam (we neglect the fact that the denominators in G are slightly different for the two scenarios). At the front of the vapor cell, the probe field has some strength E_{P0}, where the four-wave mixing beam is non-existent. The initial condition determines the applicable solution to the differential equation
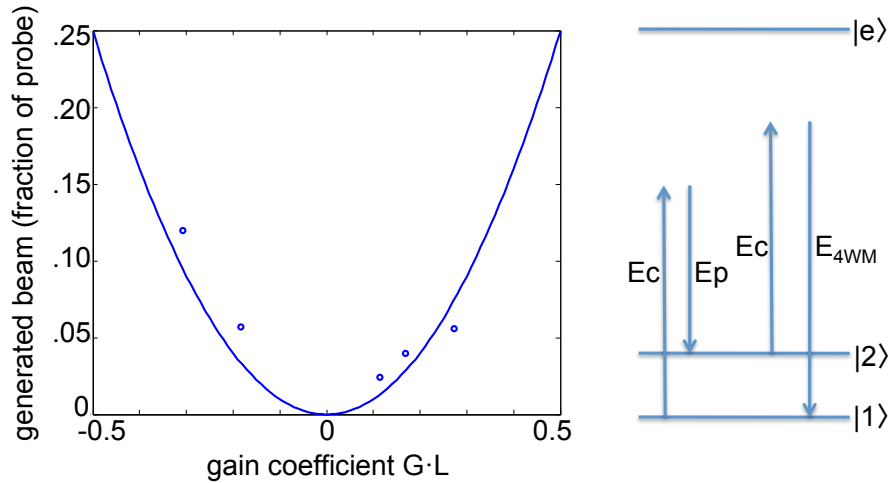
Figure B.2 Four-wave mixing in the vapor cell. We tune to a Raman resonance induced by the control beam, setting up a coherence between the ground states. The control beam then spontaneously generates a new beam.

above, Eq. B.19,

$$E_p(z) = E_{P,0} \cdot exp(Gz) \tag{B.20}$$

$$E_{FWM}(z) = G \cdot E_{P,0} \cdot z \tag{B.21}$$

Note that these solutions assume that the population of the initialized state is not depleted by the Raman process. We experimentally observe four-wave mixing effects to confirm our calculations. We use a vapor cell, 1 mm in length and 8×10^{13}/cm^3 in density. After the vapor cell, we direct the beams into a ramping Fabry-Perot in order to measure the frequency makeup of the output beams. We find $G \cdot L$ empirically by measuring the amplification/absorption of the probe after the vapor. Our results are presented in Fig. B.2 and demonstrate that the power in the generated beam goes like a fraction of the probe, $(G \cdot E_P \cdot L)^2$, as expected.

B.5   Temperature Control and Shielding

The rubidium vapor cell is magnetically shielded from the outside environment with four layers of μ-metal, each cylindrical in shape. The cell itself is held in a ceramic or brass mount inside the innermost cylinder, and has a thermocouple attached to its pinch-off tube. (Brass provides better

thermal conduction, and is preferable when the ultrathin cells must be heated to high densities.) As seen in Fig. B.3, this thermocouple leads directly to a high precision digital multimeter to get an accurate reading of the vapor cell temperature.

We wrap heating wire around the outside of the innermost μ-metal cylinder to heat up the vapor cell. The wire is insulated with fishspine beads and is twisted on itself to cancel magnetic fields. A thermocouple is attached to the outside of this μ-metal shield, just under the lip of the lid, to quickly provide temperature readings to the feedback loop. A different thermocouple is located on the cell itself and provides highly accurate temperature readings for calculating density. If adhesive or electrical insulation is needed, we use teflon tape as other adhesives burn off at the high temperatures.

The thermocouple on the μ-metal is connected directly to a Watlow 96 thermostat micropro-cessor. The output of the microprocessor plugs into a homemade gain/offset op-amp circuit with an opto-isolator (see Fig. B.4). Finally, the signal reaches a HP 6654A power supply, which turns on and off based on signals from the Watlow. The exact voltage and current setting for the "on" and "off" states are set with the front panel voltage and current knobs as the HP toggles back and forth.
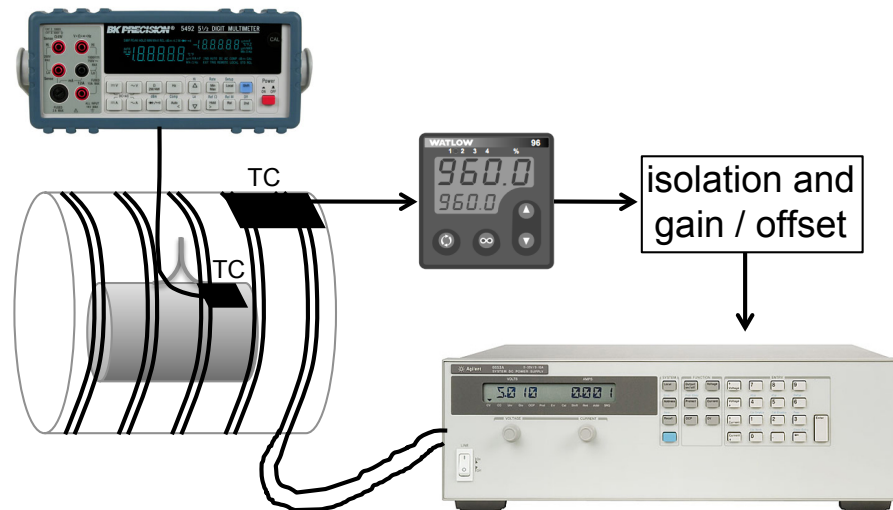
Figure B.3 The rubidium vapor cell is shielded from lab magnetic fields with four layers of μ-metal (only the innermost shield is shown here). We connect a thermocouple (TC) near the pinch-off tube, and read out the voltage on a high-precision voltmeter in order to provide precise density measurements. The innermost μ-metal shield is wrapped with twisted heating wire. A thermocouple on the shield provides input for a feedback loop.
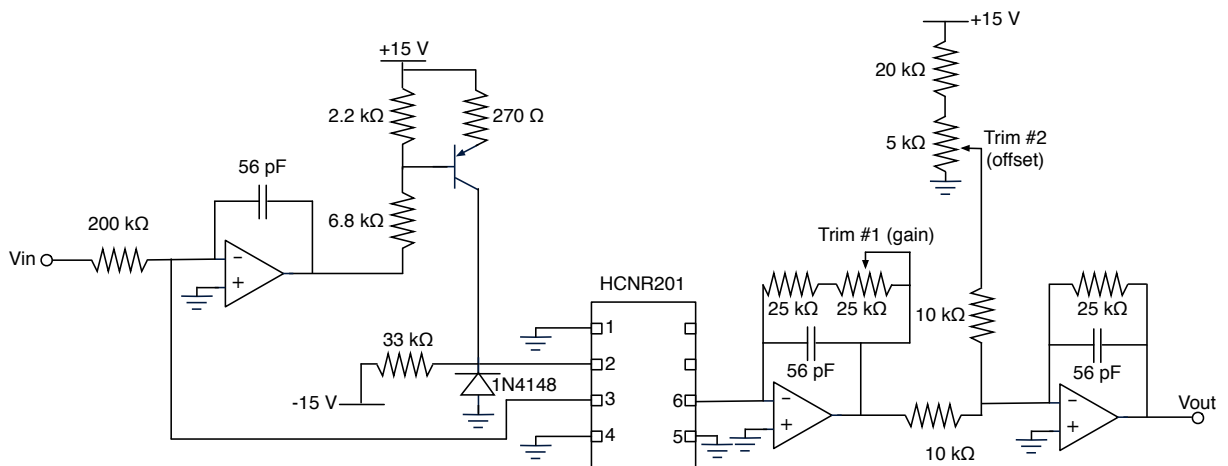

Figure B.4 The left half of this electronic circuit is stabilizes the optoisolator (see HCNR201 data sheet, Fig. 17). The right half takes the optoisolator output and adjusts the signal gain and offset. All op-amps here are TL074. Rail voltages are cleaned up through a 220 μH inductor, and a 0.2 μF capacitor to ground (not shown).

Appendix C: Vapor Cell Details

Broadening

The natural linewidth of the D_2 line of rubidium is $\Gamma = 2\pi 6$ MHz, and the excited state decays with a period of $1/\Gamma$ = 27 ns. In a vapor cell, there are a few key sources of homogenous and inhomogenous transition broadening, modifying the natural linewidth. In this section we analyze each source and discuss how it affects experimental results.

Doppler Broadening

The precise transition frequency of each atom appears shifted relative to the laser beam due to the atom's velocity component in the longitudinal direction. The velocity of each atom can be distinctly defined, making this a source of inhomogeneous broadening. Doppler broadening modifies the Lorentzian excited state line according to the temperature distribution of the atoms. The new line can be found by convolving the Lorentzian with a Gaussian whose full-width half-max comes from the relativistic Doppler effect:

$$\text{FWHM} = \sqrt{\frac{8ln(2)k_B T}{Mc^2}}(\omega_0)$$

$$\sigma = \sqrt{\frac{k_B T}{Mc^2}}(\omega_0)$$

We find that for $\omega_0 = 2\pi 384228$ GHz (λ = 780 nm) at room temperature, the new Doppler broadened profile is found by using a Gaussian with standard deviation $\sigma = 2\pi 217$ MHz. In far-off resonance two-photon experiments, the key figure is the Raman linewidth. This figure is much smaller than the excited state Doppler linewidth; using $\omega_0 = 2\pi 6.8$ GHz, we find that $\sigma = 2\pi 4$ kHz. This sets the lower limit on our experimental linewidth. (The two-photon linewidth of our laser is narrower, at ~ 1 Hz.)

Buffer gas collisions

The key purpose of buffer gas atoms and molecules is to keep the rubidium atoms in the interaction region. Even in relatively high densities, the vapor alone is sparse enough that its mean-free-path is longer than the typical cell diameter. Adding a buffer gas will keep the vapor from random-walking out of the laser interaction region during experimental pulse sequences. Typically we use 10 torr of a convenient closed-shell buffer gas such as neon to minimize resonant interactions (note that the rubidium pressure is on the order of millitorr). Using T=100°C and calculating the mean-free path,

$$\ell = \frac{k_{\mathrm{B}}T}{\sqrt{2}\pi d^2 p},$$

we find that the rubidium atoms collide with the buffer at a rate of 60 MHz.

The buffer gas collisions have additional consequences that are undesired in the context of our particular set of experiments. The rubidium excited state line suffers homogenous broadening due to dephasing. In the simplest picture, if a buffer gas collision occurs while an atom is emitting a photon, the phase of that photon will randomly reset. If this happens many times, then the emission line is significantly broadened. More precisely, the presence of the buffer gas near the rubidium atoms cause a van der Waals interaction which shifts and dephases the excited state (the ground state effects are negligible). With most buffer gas atoms, these effects occur at a rate Γ_{deph} = 29 MHz / torr [113, 114].

Wall collisions

In order to investigate effective optical pumping at very high densities, we use ultrashort vapor cells ($\sim$ 30 μm). This requires estimating how often an atom is dephased by a wall collision. In Fig. C.1, we use numerical simulations to find that atoms will on average collide with a wall every 330 ns. The simulations assume a temperature of 373 K, buffer gas pressure of 10 torr, and mean free path of about 6 μm.
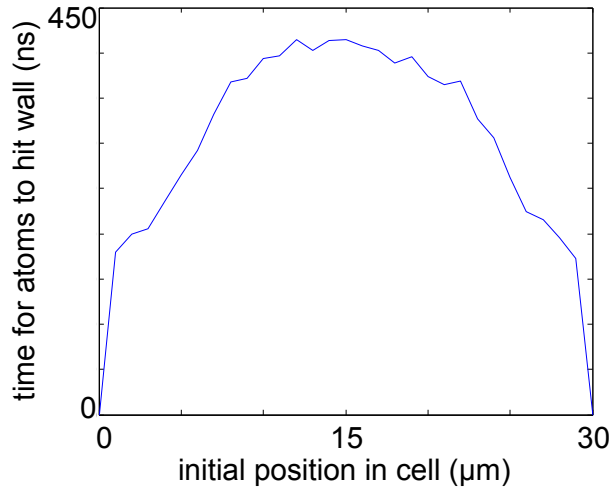
Figure C.1 The atoms diffuse to the vapor cell walls in about 400 ns. This sets an upper limit on the experimental timing schemes and Raman linewidths.

Radiation Quenching

Nitrogen serves as both a buffer gas to keep the rubidium atoms in the interaction region and to quench radiation trapping effects. When an atom is optically pumped by a laser and decays into an initialization state, the atom emits a photon. Radiation trapping occurs in dense gases when this emitted photon will likely be absorbed by a neighboring atom before escaping the vapor cell. Since the neighboring atom is necessarily already in the initialization state, this process works against the optical pumping rate but the presence of nitrogen mitigates this problem. When an excited atom collides with nitrogen molecules, it transfers the excitation energy to a vibrational molecular state, relaxing the rubidium without photon emission.

This means that the presence of nitrogen broadens the rubidium linewidth in two fashions. First, purely dephasing collisions occur at some rate Γ_{deph}, which is discussed above. Second, nitrogen further broadens the excited state line due to this resonantly-enhanced mechanism that relaxes the rubidium atom at an even faster rate.

Appendix D: Atom Localization Experiment Details

D.1 Introduction

In this appendix, we expand on the nanoscale localization experiment described in Chapter 8. We describe the experimental setup in more detail along with associated improvements and difficulties. Finally, we present results from alternate atomic schemes that are not included earlier.

D.2 Motivation

When a weak laser beam is tuned near an electronic dipole transition, the electric field of the beam drives the transition. The field suffers some absorption and accumulates positive or negative phase based on factors such as material density and frequency detuning. This can be modeled as a purely classical driven oscillator circuit.

If a second laser beam is turned on and tuned to the same excited state, a destructive quantum interference effect occurs at the excited state probability amplitude (see Ref. [1] for a conceptual review). The result is that the the two lasers drive the excited state probability amplitude exactly out of phase; neither laser interacts with the medium in the traditional way. Here, assume that a probe beam Ω_P connects state $|1\rangle$ to an excited state $|e\rangle$. Similarly, a coupling beam Ω_C connects ground state $|2\rangle$ to excited state $|e\rangle$. By writing down the Hamiltonian for a Λ-system with a probe and coupling laser (Fig. 8.2), and applying the appropriate unitary transformations, we find the so-called "dark state" Hamiltonian:

$$H = \begin{bmatrix} 0 & 0 & -\Omega_P/2 \\ 0 & \delta\omega & -\Omega_C/2 \\ -\Omega_P/2 & -\Omega_C/2 & -\Delta\omega - i\Gamma_e/2 \end{bmatrix}$$

where $\delta\omega$ is the two-photon detuning, $\Delta\omega_p$ is the probe single-photon detuning. We can then model this system by plugging the Hamiltonian into Schrodinger's equation and finding the probability

amplitudes:

$$\dot{c}_1 = -\Omega_P c_e \qquad (D.1)$$

$$\dot{c}_2 = \delta\omega c_2 - \Omega_C c_e \qquad (D.2)$$

$$\dot{c}_e = -\Omega_P c_1 - \Omega_C c_2 - (\Delta\omega + i\Gamma_e/2) c_e. \qquad (D.3)$$

Solving these equations simultaneously gives the time dynamics of this 3-state system, assuming that excited state spontaneous decay is to outside the system.

Using probability amplitudes, c_1, c_2, and c_e, we can find the linear susceptibility of the system by setting c_a=1, solving for c_e, and then finding the polarizability of the medium $P = \epsilon\chi E$, we find that $P = 2\mu_{1e}c_1 c_e$,

$$\chi = \frac{2|\mu_{1e}|^2 N}{-2\Delta\omega_p - i\Gamma_e + \frac{\Omega_c^2}{2\delta\omega}}. \qquad (D.4)$$

Probing the frequency response of a system requires a very weak beam that is turned on slowly compared to the width of the transparency window, $\Omega_C^2/(4\Gamma)$. For a typical linear susceptibility curve, see Fig. 8.2.

In the case of the localization experiment described in Chapter 8, we use a nonperturbative probe beam to introduce a different set of dynamics. As the probe turns on (with the coupling beam already on) the atoms evolve into the dark state, which in this regime is a superposition of ground states. This can be found by solving the steady state Schrodinger equation using D.4. Assuming $c_e = 0$ and $|c_1|^2 + |c_2|^2 = 1$ we find that $|c_1|^2 = \Omega_C^2/(\Omega_P^2 + \Omega_C^2)$ and $|c_2|^2 = \Omega_P^2/(\Omega_P^2 + \Omega_C^2)$ (see Eqn. 8.1).

D.3   Magneto-optical trap

We measure the number of atoms in the cloud by collecting light with a 2 inch lens and focusing it into an amplified photodiode. After back-calculating to find the power hitting the photodiode, and finding the solid angle subtended by the lens, we can find the amount of optical power emitted by the MOT into all angles. (Typically, we measure 0.5 mW emitted into 4π.) Next we find the

single-atom scattering rate to find the power emitted by a single atom,

$$\gamma_p = \frac{s_0 \cdot \gamma/2}{1 + s_0 + (2\delta/\gamma)^2}, \tag{D.5}$$

where $s_0 = I/I_{SAT}$, I_{SAT} is the intrinsic saturation intensity of the gas, and γ is the excited state decay rate [115]. The detuning δ is set to 2γ for optimal cooling. We can then use the power emitted by a single atom, $P_{atom} = \gamma_p \hbar \omega$ to find the number of atoms. We typically observe about one billion atoms in the MOT. The density is set by outward radiative pressure, where each atom is emitting photons that are then absorbed by nearby atoms.

The temperature of the MOT is found by measuring the average atom velocity using a release-recapture protocol. This requires us to first record the MOT fluorescence on a photodiode, usually with an iris in front of it so that we are measuring the central 30% of atoms. We then briefly turn off the MOT beams and allow the cloud to thermally expand. When we turn the MOT beams back on, we record the fluorescence at the turn-on, and therefore the fractional loss. After measuring this release-recapture process for a number of different release times, from 1 to 50 ms, we can then calculate the velocity of the atoms. In a standard MOT setup, the final atom temperature is Doppler-limited to $T_{dopp} = \hbar k/\gamma = 150 \mu K$.

Optimization

MOT characteristics such as temperature and number are a function of how well the beams and magnetic fields are aligned to each other. Shimming the MOT improperly can mean a significantly hotter cloud. We find that the following procedure below works well for balancing a large MOT such as ours:

1. Set up orthogonal cameras (such as a TV/CCD camera and the Andor camera).

2. Magnetically shim the MOT such that the optical molasses is approximately balanced. (When the MOT B-field is turned-off, but shims are left on, the atoms should not immediately disappear to one direction. They should expand symmetrically over the course of a few seconds.) While looking at molasses, also recenter the beam retroreflections so that they go back to their originating fibers.

3. Turn up the gradient B-field until the MOT is significantly compressed. Note its position; this is likely the magnetic-field zero.

4. If the uncompressed MOT is severely misaligned from the compressed MOT position, then adjust the MOT beams and retroreflections. For small misalignments, adjust the shim coils.

It is important to keep an eye on the overall MOT fluorescence to make sure that the MOT is not becoming more balanced at the expense of atom number. With that said, as the MOT is moved, the fluorescence collecting photodiode may need to be realigned.

D.4   Standing wave

We produce a coupling beam transverse standing wave at the atoms by splitting the coupling beam into two and combining it at a shallow angle. This is accomplished with a half waveplate and two polarizing beamcubes, one mounted just millimeters above the other. This produces a standing wave at the atoms with intensity period λ/θ. In order to achieve a relatively small angle of 5 milliradians, we split the beams 2 meters from the MOT. The long optical path makes the system susceptible to angular deflections due to convection gradients (common causes include overhead air ducts, computer fans, and RF amplifiers near the beam). Additionally, since our experimental protocol calls for averaging many pictures together and then measuring the size of the atom localization, we require that the intensity nodes remain stationary from picture-to-picture. Such movement widens the apparent size of the atom localization effect.

We emphasize that the shot-to-shot noise described above is movement of *both* coupling beams. Our experiment is insensitive to the more typical interferometric noise, caused by differential phase jitter of the individual arms. Phase differences between the two coupling beams caused by air currents is not detectable in the final pattern. With that said, we do have difficulty obtaining perfect zeros at the coupling beam nodes (i.e. the entire interference pattern has a DC offset). We measure these nodes to be 2% of the peak intensity, possibly a result of contamination of the beams by bad polarizations. This is measured both on a Newport CCD camera and by vertically translating a photodiode masked by a pinhole.

The interferometric purity is crucial to the success of this experiment. While our scheme is robust to many experimental errors (e. g. non-zero detunings, peak-intensity fluctuations, etc.), the scheme by definition depends very sensitively on any intensity at the standing wave nodes.

For two beams combining at an angle θ, an electric field standing wave pattern of period $\Lambda = 2\lambda/\theta$ is produced (or an intensity standing wave of period $\Lambda/2$). The full-width half-max of the localized population is $(\Omega_P/\Omega_{C0}) \cdot (\Lambda/2\pi)$. If the coupling beam intensity does not vanish at the standing wave nodes but rather only minimizes to some Rabi frequency δ, then we describe the localization population spatial width using the following modified equation:

$$FWHM = \left(\frac{\sqrt{\Omega_P^2 + \delta^2}}{\sqrt{\Omega_{C0}^2 + \delta^2}} \right) \cdot \left(\frac{\Lambda}{2\pi} \right). \tag{D.6}$$

As an example, the experimental results shown in Chapter 2 contain intensity impurity of 2%. For the case of the most localized data point in Fig. 8.4, where $I_{C0} = 1800$ mW/cm^2 ($\Omega_C = 7.7$ GHz) and $I_P = 4$ mW/cm^2 ($\Omega_P = 25$ MHz), the presence of a 2% impurity affects the theoretical FWHM by more than ten-fold.

D.5   Pulse timings

It is crucial that the probe and coupling beams are turned on in the counter-intuitive beam sequence. Additionally, the pulses must be turned-off simultaneously in order to preserve the coupling beam spatial information in the atoms. This ensures that the ratio $\Omega_C(z)/\Omega_P$ remains constant until the beams are completely off.

The probe and coupling beams are switched by 110 MHz and 120 MHz acousto-optic modulators, respectively. The 120 MHz AO (75% diffraction efficiency per pass) is centered closer to the driving frequency of 133 MHz, and is therefore used to switch the coupling beam. The 110 MHz AO (25% efficiency per pass) is used to switch the probe. Each AO has a different response to the driving frequency, causing a significant turn-on and turn-off disparity of about 2 μs. The optical rise-time/fall-time of each pulse is about 50 ns.

We use pulses on the 100 ns scale in order to reduce the potential for optically pumping the atoms. Note that the EIT only achieves 80% transmission due to dephasing and , and the probe is
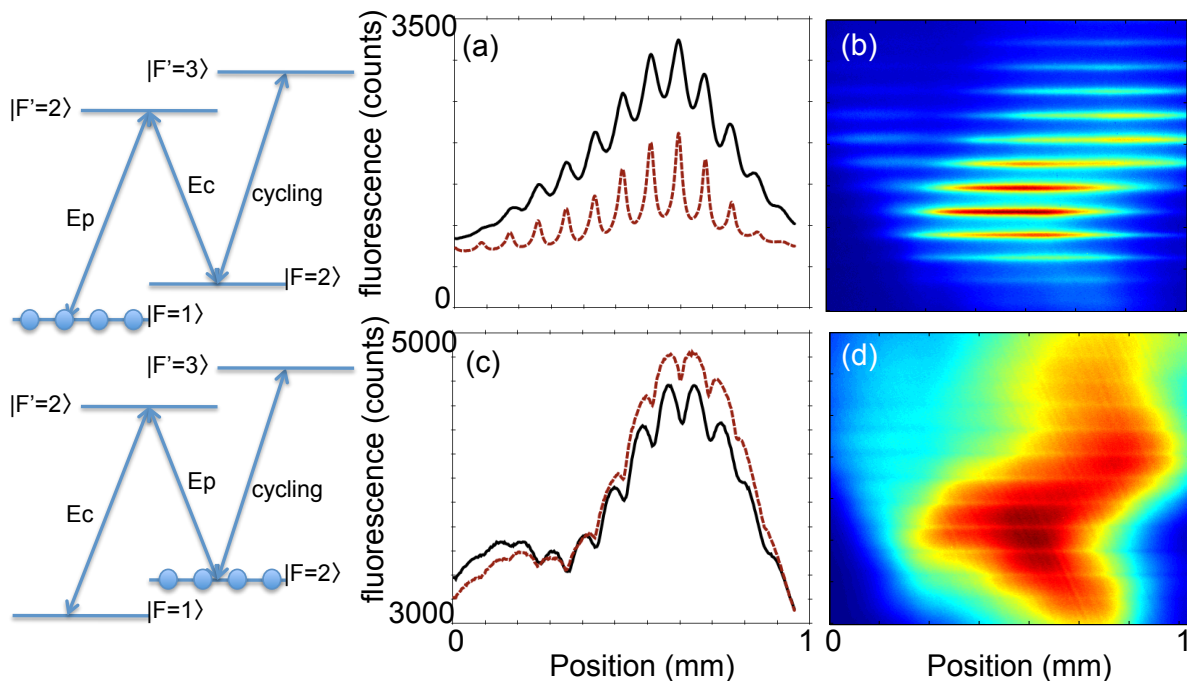
Figure D.1 Results from two different arrangements. In the top row, we use the standard configuration of fluorescing the coupling beam ground state. (a) depicts an unlocalized line profile (black, solid line) and a localized line profile (red, dashed line) where the coupling beam is more intense. The localized line profile is taken from the CCD picture depicted in (b). Plot (c) and picture (d) depict the same results, except that we fluoresce the probe beam ground state. Notice that here, the non-fluorescing atoms are localized, providing for worse signal-to-noise.

on the order of the rubidium saturation intensity. (In the absence of the coupling beam, the probe optically pumps 25% of the atoms.)

D.6   Energy Level Schemes

In the experiment presented in the body of this thesis, we set up a Λ-system using three parallel channels. There are a number of different configurations which would give us a three-state Λ scheme. In this section, we briefly summarize the benefits and drawbacks of the various configurations available.

Parallel Channels

Chapter 2 presents results using a parallel channel Λ scheme, with the probe resonant with $|F = 1\rangle$ and coupling beam resonant with $|F = 2\rangle$. There are three channels, each operating independently of the others and each resonant with different magnetic sublevels. We use collinear beams with the same polarization of circularly-polarized light. (Linear polarized light would include a forbidden transition where $\Delta F = 0$ and $m_F = m_{F'} = 0$.) There are several key advantages to this scheme: (1) each of the three probe channels is paired with a coupling-beam channel, minimizing probe absorption, (2) atoms that are excited will likely decay to an EIT channel or be pumped into one, (3) no bias field is necessary, unlike stretched state schemes (see below), and (4) our fluorescence lasers – the MOT beams – are tuned to $|F = 2\rangle$.

Expanding more on the final point above, it is beneficial to fluoresce the coupling beam's ground state (rather than the probe beam's ground state). Since this is not the initialized state, only atoms which transfer ground states will fluoresce. This means the experiment will image bright fringes of atoms that are tightly localized to particular spots in the cloud. If instead we fluoresce the probe ground state, then we will image localized dark fringes in a bright cloud. This introduces added complications such as reduced contrast (signal-to-noise) and also worse apparent localization, both due to spontaneous emission by atoms near the dark fringes. Figure D.1 illustrates each of these schemes[1].

Stretched State

In order to simplify the experiment, it is ideal to initialize the atoms to a stretched state, where the electronic spin-orbital state can only be written as a single hyperfine state, $|I = 3/2, S = 1/2\rangle \rightarrow |F = 2, m_F = 2\rangle$. Fig. D.2 illustrates how we initialize atoms to the stretched state. A circularly polarized optical pump beam resonant with $|F = 2\rangle \rightarrow |F' = 3\rangle$ pumps atoms from the ground state to an excited state with an additional unit of angular momentum, $\Delta m_F = +1$. Most excited state magnetic sublevels can decay to a ground state such that $\Delta m_F = -1, 0, +1$. When an

---

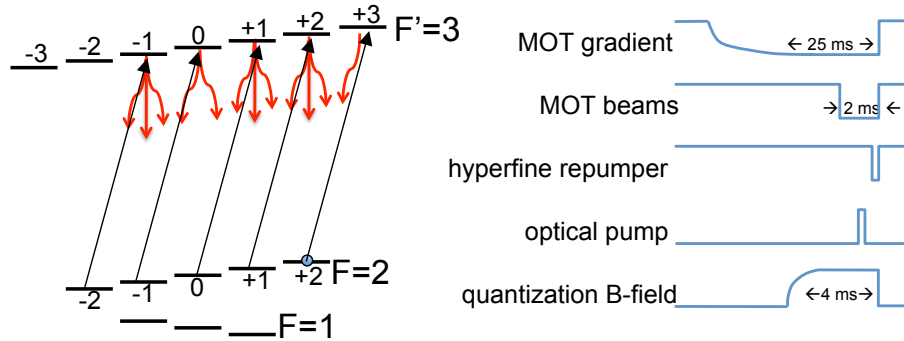[1]Fig. D.1 (a) depicts 10/15/2010 sets 1 and 9. (b) depicts 10/22/2010 sets 2 and 10.

Figure D.2 Stretched state optical pumping scheme. Atoms in any magnetic sublevel of $|F = 2\rangle$ are excited and will decay back to a ground state. The curved red arrows indicate whether m_F=-1, 0, and +1 transitions are allowed during decay. The key is that atoms initially in $|F = 2, m_F = 2\rangle$ will excite to $|F' = 3, m_F = 3\rangle$, a state whose only decay channel is back to $|F = 2, m_F = 2\rangle$. The hyperfine repumper ($|F = 2\rangle \rightarrow |F' = 3\rangle$) is not shown. The pulse sequence is shown on the right. It is crucial to keep the MOT beams off once the bias quantization B-field ramps up so that the atoms don't experience an unbalanced force.

atom eventually decays to $|F = 2\rangle$, it will excite to $|F' = 3\rangle$ where the only decay channel is back to $|F = 2\rangle$.

The pulse sequence is shown in Fig. D.2. After loading the MOT with atoms, we turn off the gradient magnetic field and wait for it to ring down. We then turn on the bias quantization field and wait for it to inductively ramp up. The MOT beams are turned off at this point to avoid applying a photon pressure to the atoms. We then run our experiment (whose pulse sequence is explained in detail elsewhere) before returning to normal MOT parameters.

The bias field is formed from a pair of coils, 50 turns each, running about 7 amps, supplying about 1 Gauss at the atoms. The purpose of this field is to ensure that the quantization axis of the atoms is well-defined in the direction parallel to the optical pump beam. Stray fields transverse to the quantization axis will torque the atoms, causing mixing as seen by the beams. This effect is mitigated by using a strong bias field such that the vector sum of all present fields is nearly parallel to the direction of the bias. Otherwise, as atoms are torqued out of the quantization axis, the beams will see a depopulation (mixing) of the stretched state to the other magnetic sublevels. Stray fields in the direction parallel to the quantization axis cause broadening of the transition, since the exact Zeeman splitting will be poorly defined.
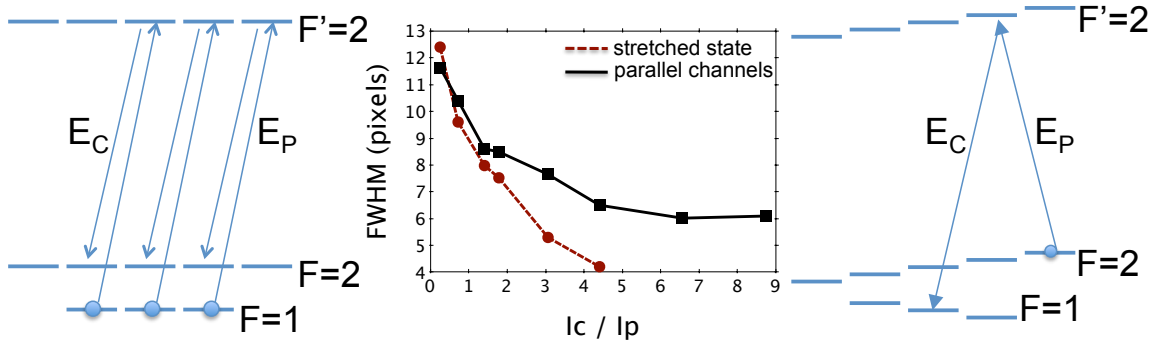
Figure D.3 Parallel channels (left) and stretched state (right) configurations result in different amounts of localization (center).

The optical pump beam itself illuminates the MOT for only about 100 μs. Since this beam cycles the stretched-state atoms rather than shelving them in a non-fluorescing state[2], it is crucial to use a short pulse and weak intensity, typically around I_{SAT}. The optical pump retroreflection is optimized by turning on the beam continuously and adjusting the retroreflector until the steady-state MOT fluorescence is maximized, usually to about 90% of the original value in the absence of the pump.

We can study the stretched state fractional population by using a very weak probe laser tuned to $|F = 2\rangle \rightarrow |F' = 2\rangle$. The probe and pump both have the same circular polarization and run nearly parallel to each other. After shutting off the optical pump, if the atoms are successfully loaded into the stretched state $|F = 2, m_F = 2\rangle$, then the probe will propagate without absorption. This results from the fact that the probe, in making a $\Delta m_F = +1$ transition is resonant with a dipole forbidden state, $|F = 2, m_F = +2\rangle \rightarrow |F' = 2, m_F = +3\rangle$. By studying probe absorption both in $\sigma+$ polarization as described, and $\sigma-$ polarization, we estimate that under the experimental parameters described above we achieve 75% stretched state population.

As noted earlier, the key advantage of using the stretched state is to perform an EIT experiment using a single channel. We begin by tuning the probe to the transition $|F = 2, m_F = 2\rangle \rightarrow |F' = 2, m_F = 1\rangle$ and the coupling beam to $|F = 2, m_F = 0\rangle \rightarrow |F' = 2, m_F = 1\rangle$. We probe

---

[2]Alternately, one can tune the optical pump to the $|F = 2\rangle \rightarrow |F' = 2\rangle$ transition. The drawback is a frequent decay to the $|F = 1\rangle$ ground state.
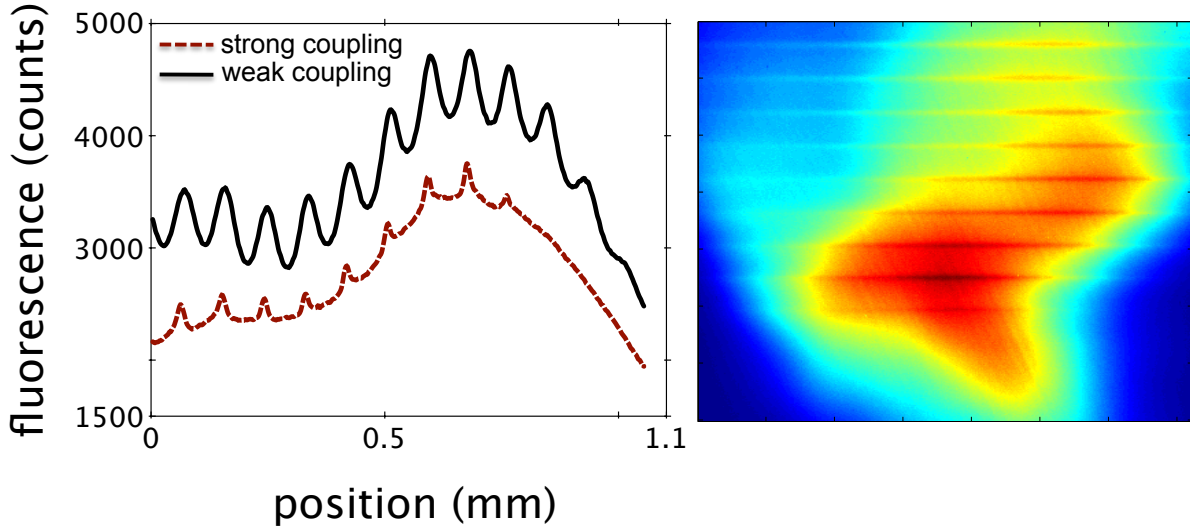
Figure D.4 Atoms are pumped to $|F = 2\rangle$ and a single, standing-wave optical pump laser pumps the atoms to $|F = 1\rangle$. Only atoms within very localized regions of the standing-wave nodes will remain in $|F = 2\rangle$.

the EIT response of the system and measure a curve similar to the parallel channels case, seen in Fig. 8.2. We face two major hurdles when attempting an EIT localization experiment starting with the stretched state: 1) MOT expansion and atom loss hinder sharp imaging of spatial localization, and 2) some spatial localization is due to optical pumping effects, as discussed in the following section.

D.7 Localization due to optical pumping

A legitimate criticism of this experiment is that the localization mechanism is not EIT but rather spatially dependent optical pumping. This scheme would work as follows: the probe transfers the atoms from $|F = 1\rangle$ to $|F = 2\rangle$, and the spatially dependent coupling beam pumps all the atoms back, except for those located at coupling beam nodes. The pumping rate goes linearly with the square root of coupling beam intensity up to the saturation intensity I_{SAT}. If a standing wave coupling beam is used whose peak intensity is many times I_{SAT}, then only atoms in tightly localized regions will experience a coupling beam too weak to pump ($I < I_{SAT}$). If we assume the probe essentially loads the atoms into $|F = 2\rangle$, and then we neglect it from the problem, we are

left with a simpler system of three levels with a pump (coupling) beam. This mechanism would then localize atoms to a spatial full-width half-max of

$$FWHM \approx \sqrt{\frac{2I_{SAT}}{I}} \frac{\Lambda}{2\pi} \cdot exp\left(\frac{-t\Gamma}{4}\right), \tag{D.7}$$

where I_{SAT} is the saturation intensity. Note that the above equation should be taken as a back-of-the-envelope approximation.

To respond to this criticism, we carefully study our experiment to understand the dominant mechanism of population transfer. The most straightforward measure involves simply tuning the probe frequency across the single-photon resonance and tracing out a typical EIT transmission curve. While this seems to indicate EIT as the dominant mechanism, it can still be argued that the on-resonance transmission is due to a mechanism other than EIT. Additionally, since we cannot record probe transmission in the case of a stronger probe beam, as is often used in the experiment, a secondary measure is necessary.

This measure requires triggering the CCD camera *during* the EIT experiment, rather than triggering it after the experiment while fluorescence lasers illuminate the atoms. We then use the camera to capture the magnitude and location of excited state spontaneous decay, a measure of excited state population. In the complete absence of EIT, atoms located at coupling beam antinodes will scatter many photons, as they are pumped back and forth by the probe and coupling beams. (Atoms located at coupling beam nodes will only scatter one or two probe photons, until they are shelved in $|F = 2\rangle$).

In the complete absence of incoherent optical pumping, such that EIT is the exclusive mechanism for population transfer, we expect to now observe minimal scatter at coupling beam *antinodes*. These atoms are most completely in the dark state with near-vanishing population at the excited state.

What we actually observe is illustrated in Fig. D.5. When the peak coupling beam is weak, we find that the spontaneous emission from the atoms results from those located at coupling beam antinodes. This means that any atom transfer taking place is a result of optical pumping. As the coupling intensity is turned up, the opposite happens – the spontaneous emission collected by the

camera is a result of atoms in the coupling beam nodes. This is a signature that the cloud is in the dark state and EIT is dominant. Remarkably, as we turn up the peak intensity of the coupling beam we witness the fringes of scattered photons actually invert (as shown in Fig. D.5). We call this "fringe inversion" and it indicates at what point EIT is the dominant mechanism of localization.

Using this fact, we can determine the minimum necessary peak coupling intensity to achieve EIT. This is partly determined by the scheme one chooses. In the center plot of Fig. D.3, the stretched state does not show signs of EIT, based on the scattering tests just described, until the coupling beam is at its maximum value (recording the final data point). In the same figure, localization due to parallel channels is plotted. In this case, we confirm that the atoms are evolving into the dark state for a much lower value, where Ic/Ip $\simeq$ 1.5.

Additionally, in Fig. D.6 we analyze at what control intensity the spontaneous emission is minimized in coupling beam antinodes by collecting photons from these areas in the picture and plotting it against coupling beam intensity. We do this for three different probe intensities, including parameters nearly identical to those of our experiments described in Ref. [92]. Those experiments initialize the atoms to $|F = 1\rangle$, and then use a probe resonant with $|F = 1\rangle \rightarrow |F' = 2\rangle$, and a coupling beam with parallel circular polarization resonant with $|F = 2\rangle \rightarrow |F' = 2\rangle$.

In Fig. D.7, using similar parameters, we again record spontaneous emission from the MOT during the EIT experiment in the absence of fluorescence lasers. What we find is that fluorescence is minimized when the lasers reach two-photon resonance. This suggests that the atoms in the dark state when the two-photon condition is met. We confirm this by doing a simple EIT experiment, shown in Fig. D.8, with a probe whose power is comparable to that of localization experiments (50 μW).

The fact that the parallel channels scheme works primarily with EIT as the underlying mechanism, unlike the stretched-state case, can be understood in terms of the nonzero excited state population. During any of our experiments, even with a strong coupling beam, the excited state will populate with some small probability. When this happens, the atom will decay to some sublevel. In the case of the parallel channels scheme, the chance that the atom decays to an EIT channel, or is pumped to one, is high. In the case of the stretched state scheme, though, the atoms

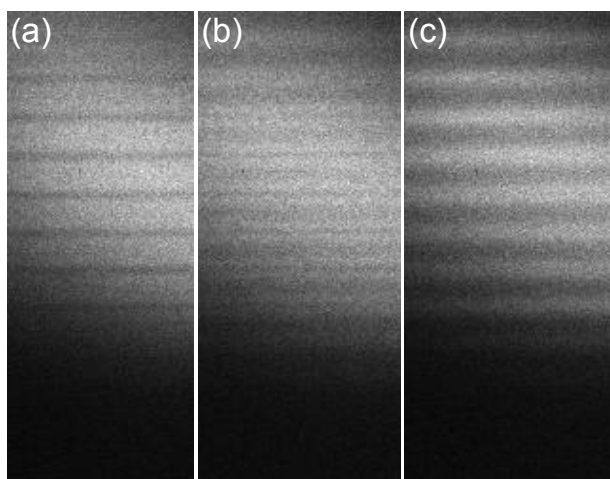most likely decay to outside the EIT system and will then be optically pumped back-and-forth by the beams.

Figure D.5 Picture of the MOT while illuminated by EIT beams for a (a) weak, (b) moderate, and (c) strong peak-intensity coupling beam. In picture (a), atoms located at coupling beam antinodes scatter the most light, since these atoms are pumped back and forth between ground states. In (c), only atoms located at coupling beam antinodes scatter light. The coupling beam intensity used in (a) is not strong enough to render the excited state dark, where in (c) it is.
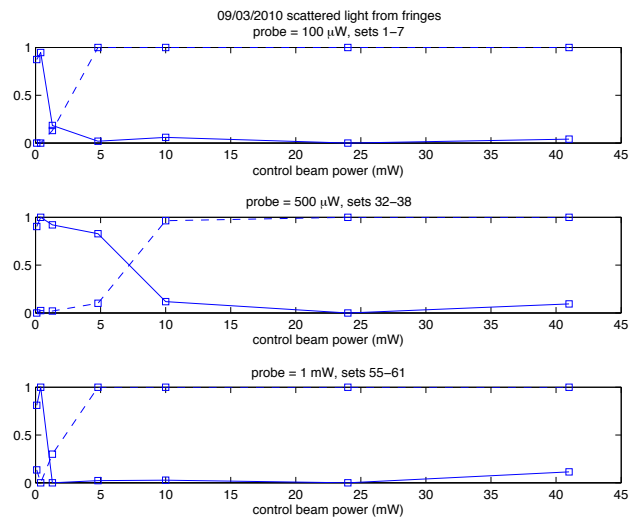
Figure D.6 Plots of spontaneous emission from the MOT while EIT beams are on, in the absence of fluorescence beams. The solid line indicates light collected from coupling beam antinodes, while the dashed line indicates light collected from coupling beam nodes. We use parameters nearly identical to those of Ref. [92].
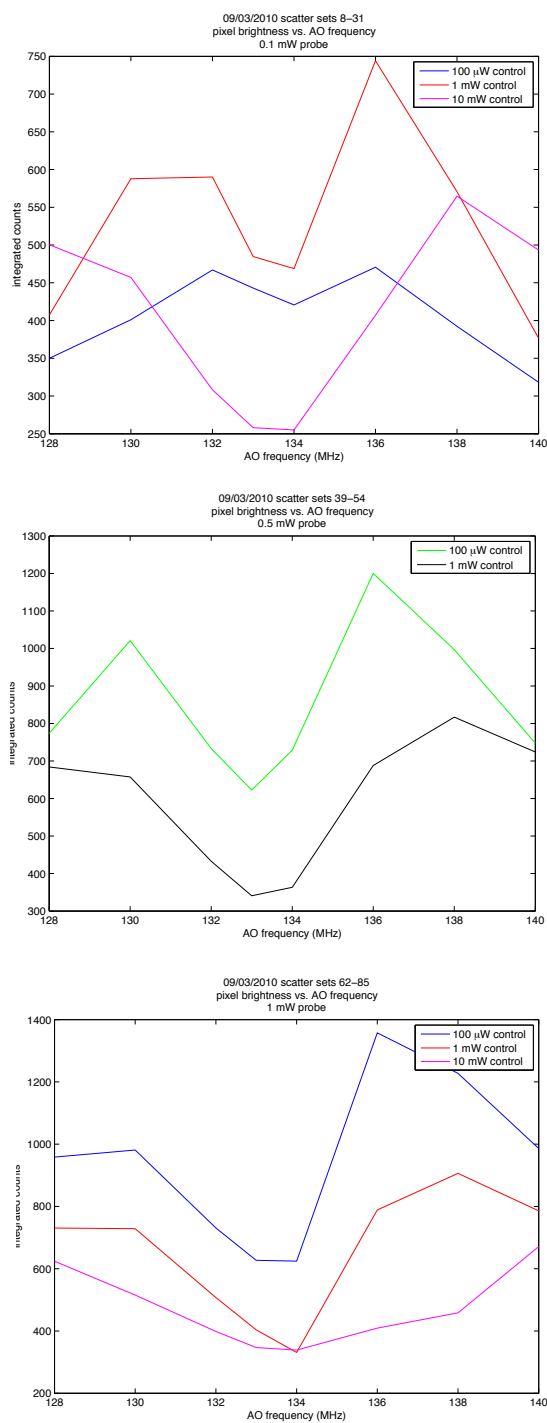
Figure D.7 Spontaneous emission vs. frequency of a double-passed AO. We integrate pixel counts in the region of the coupling beam antinodes, and find that spontaneous emission is suppressed when the probe and coupling beams are tuned to two-photon resonance. We use parameters nearly identical to those of Ref. [92].
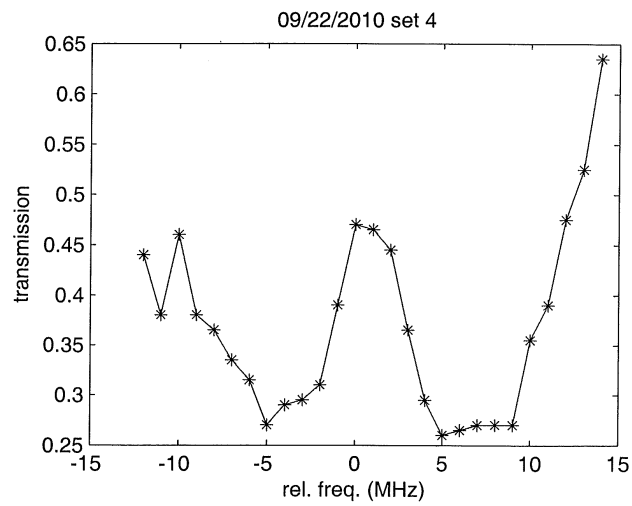
Figure D.8 Probe transmission in an EIT system, using a 50 μW probe. This measurement demonstrates that the atoms in the dark state, and therefore transparent to the on-resonant probe, using parameters typical of our localization experiments. We use parameters nearly identical to those of Ref. [92].

Appendix E: Noise considerations in all-optical switches

E.1 Introduction

In this appendix, we analyze the scheme presented in chapter 9 with respect to the amount of noise the switch adds to the probe beam. The scheme suggested earlier involves 50% absorption of probe photons. We wish to find out, how efficiently are the photons emitted back into the probe with random phase. We compare the fidelity of the V-type scheme presented here with a refractive index enhanced switch and a switch involving EIT.

E.2 Noise contribution in the V-type scheme

The transmission fraction of the probe wavepacket is described in chapter 9; it finds that the transmission goes like $\Gamma/\Delta \cdot \phi^{(1)}$, where $\phi^{(1)}$ is the first-order phase accumulation due to the propagation of the probe beam. In order to achieve a phase shift of π radians, with the probe transmission set to 50%, as described in the earlier chapter, 5000 photons are required in the switch beam. What is not addressed in the earlier chapter, though, is the fraction of absorbed probe photons will be emitted as noise into the probe beam. Using the same type of semiclassical argument introduced in appendix chapter B, we find that noise is emitted into the probe spatial mode at a rate of

$$R_{noise} \;\; = \;\; \left(\frac{n_p \Gamma}{\Delta_p \tau}\right) \left(\frac{\lambda^2}{8\pi^2 A}\right) \phi^{(1)}. \tag{E.1}$$

Using an optical cavity, we can filter out light in the probe beam that is outside of the signal bandwidth ($1/\tau$). Since the probe beam operates in the far-detuned regime, a cavity can nearly perfectly purify the beam from spontaneous emission which is centered around the resonance. After filtering out unwanted frequency modes, noise enters the probe at a rate of

$$R_{noise,cav} \;\; = \;\; \left(\frac{\Gamma}{\tau\Delta^2}\right) \left(\frac{n_p \Gamma}{\Delta_p \tau}\right) \left(\frac{\lambda^2}{8\pi^2 A}\right) \phi^{(1)}. \tag{E.2}$$

Plugging in numbers according to our suggestion in chapter 9, we find that the noise added to the probe spatial and frqeuency modes by our scheme is approximately zero ($10^{-8} \cdot n_p$).

E.3 Noise considerations in other schemes

The all-optical phase switch proposed by Sikes and Yavuz considers a very weak probe and switch beam propagating through an index-enhanced vapor [111]. The probe alone, whose frequency is exactly between the absorptive and amplifying Raman resonances, will accumulate phase due to the enhanced refractive index. When the switch beam is turned on, the absorptive and amplifying Raman resonances separate so that the probe no longer accumulates much phase. Since the probe frequency is still exactly between the two resonances, though, vanishing nonlinear absorption is still maintained. There are two constraints when this scheme is used in the weak beam limit. First, the energy equivalent of 40 photons in the switch beam is required to suitably modify the probe phase. Second, three photons of noise will be added to the probe beam in the event that it accumulates pi radians of phase [112]. While these constraints seem trivial, they eliminate the possibility that this switch be used as a single-photon phase gate.

An all-optical phase switch proposed by Imamaglu and Lukin has received much attention as a possible route to interact two single photons with good fidelity [102]. This involves propagating a probe photon at a slow group-velocity through a system in the dark state. When a switch photon travels with the probe, the probe dark state is modified such that the probe accumulates some phase. Since the switch photon velocity must match the probe, a second dark state system is set up. New results from the literature show that this scheme, much like all the others presented here, will suffer from noise due to spontaneous emission [116, 117]. The table below sums up these results.

Type of scheme	switch energy (photons)	noise (photons/radian)
V-type	1000	~ 0
refractive index enhancement	10	1
Double EIT system	1	1

Bibliography

[1] S. E. Harris, Phys. Today **50**, 36 (1997).

[2] O. Kocharovskaya and P. Mandel, Phys. Rev. A **42**, 523 (1990).

[3] A. Kasapi, M. Jain, G. Y. Yin, and S. E. Harris, Phys. Rev. Lett. **74**, 2447 (1995).

[4] L. V. Hau, S. E. Harris, Z. Dutton, and C. H. Behroozi, Nature **397**, 594 (1999).

[5] M. M. Kash *et al.*, Phys. Rev. Lett. **82**, 5229 (1999).

[6] J. L. Wang, A. Kuzmich, and A. Dogariu, Naure (London **406**, 277 (2000).

[7] G. M. Gehring, A. Schweinsberg, C. Barsi, N. Kostinski, and R. W. Boyd, Science **312**, 895 (2006).

[8] H. Schmidt and A. Imamoglu, Opt. Lett. **21**, 1936 (1996).

[9] S. E. Harris, J. E. Field, and A. Imamoğlu, Phys. Rev. Lett. **64**, 1107 (1990).

[10] H. Kang and Y. Zhu, Phys. Rev. Lett. **91**, 093601 (2003).

[11] M. O. Scully, Phys. Rev. Lett. **67**, 1855 (1991).

[12] A. S. Zibrov *et al.*, Phys. Rev. Lett. **76**, 3935 (1996).

[13] D. D. Yavuz, Phys. Rev. Lett. **95**, 223601 (2005).

[14] J. E. Thomas, Opt. Lett. **14**, 1186 (1989).

[15] J. R. Gardner, M. L. Marable, G. R. Welch, and J. E. Thomas, Phys. Rev. Lett. **70**, 3404 (1993).

[16] K. D. Stokes *et al.*, Phys. Rev. Lett. **67**, 1997 (1991).

[17] M. O. Scully and M. S. Zubairy, *Quantum Optics* (Cambridge University Press, 1997).

[18] M. O. Scully and M. Fleischhauer, Phys. Rev. Lett. **69**, 1360 (1992).

[19] M. Fleischhauer *et al.*, Phys. Rev. A **46**, 1468 (1992).

[20] U. Rathe, M. Fleischhauer, S.-Y. Zhu, T. W. Hänsch, and M. O. Scully, Phys. Rev. A **47**, 4994 (1993).

[21] M. Macovei and C. H. Keitel, Journal of Physics B: Atomic, Molecular and Optical Physics **38**, L315 (2005).

[22] A. S. Zibrov *et al.*, Phys. Rev. Lett. **76**, 3935 (1996).

[23] M. Fleischhauer and M. D. Lukin, Phys. Rev. Lett. **84**, 5094 (2000).

[24] D. F. Phillips, A. Fleischhauer, A. Mair, R. L. Walsworth, and M. D. Lukin, Phys. Rev. Lett. **86**, 783 (2001).

[25] C. Liu, Z. Dutton, C. H. Behroozi, and L. V. Hau, Nature **409**, 6819 (2001).

[26] P. Anisimov and O. Kocharovskays, 38th Winter Colloquium on Physics of Quantum Electronics, Snowbird, Utah, 2008. .

[27] S. E. Harris, Opt. Lett. **19**, 2018 (1994).

[28] S. E. Harris and A. V. Sokolov, Phys. Rev. A **55**, R4019 (1997).

[29] D. D. Yavuz, A. V. Sokolov, and S. E. Harris, Phys. Rev. Lett. **84**, 75 (2000).

[30] M. D. Lukin, Rev. Mod. Phys. **75**, 457 (2003).

[31] M. Fleischhauer, A. Imamoglu, and J. P. Marangos, Rev. Mod. Phys. **77**, 633 (2005).

[32] D. D. Yavuz, D. R. Walker, and M. Y. Shverdin, Phys. Rev. A **67**, 041803 (2003).

[33] M. Y. Shverdin, D. D. Yavuz, and D. R. Walker, Phys. Rev. A **69**, 031801 (2004).

[34] D. D. Yavuz, Phys. Rev. A **75**, 041802 (2007).

[35] G. I. Stegeman and M. Segev, Science **286**, 1518 (1999).

[36] S. Trillo and W. Torruellas, *Spatial Solitons* (Springer-Verlag, Berlin, 2001).

[37] D. R. Walker *et al.*, Opt. Lett. **27**, 2094 (2002).

[38] R. R. Moseley, S. Shepherd, D. J. Fulton, B. D. Sinclair, and M. H. Dunn, Phys. Rev. Lett. **74**, 670 (1995).

[39] R. R. Moseley, S. Shepherd, D. J. Fulton, B. D. Sinclair, and M. H. Dunn, Phys. Rev. A **53**, 408 (1996).

[40] A. G. Truscott, M. E. J. Friese, N. R. Heckenberg, and H. Rubinsztein-Dunlop, Phys. Rev. Lett. **82**, 1438 (1999).

[41] J. T. Manassah and B. Gross, Optics Communications **124**, 418 (1996).

[42] R. Kapoor and G. S. Agarwal, Phys. Rev. A **61**, 053818 (2000).

[43] T. Hong, Phys. Rev. Lett. **90**, 183901 (2003).

[44] H. Shpaisman, A. D. Wilson-Gordon, and H. Friedmann, Phys. Rev. A **71**, 043812 (2005).

[45] K. J. Jiang, L. Deng, and M. G. Payne, Phys. Rev. A **74**, 041803 (2006).

[46] J. E. Bjorkholm and A. A. Ashkin, Phys. Rev. Lett. **32**, 129 (1974).

[47] G. Grynberg, A. Maître, and A. Petrossian, Phys. Rev. Lett. **72**, 2379 (1994).

[48] R. S. Bennink *et al.*, Phys. Rev. Lett. **88**, 113901 (2002).

[49] B. Schapers, T. Ackermann, and W. Lange, IEEE J. Quantum Electron. **39**, 227 (2003).

[50] B. E. Unks, N. A. Proite, and D. D. Yavuz, Rev. Sci. Instrum. **78**, 083108 (2007).

[51] L. Essen and J. V. L. Parry, Nature **176**, 280 (1955).

[52] N. Schlosser, G. Reymond, I. Protsenko, and P. Grangier, Nature (London) **411**, 1024 (2001).

[53] D. Schrader *et al.*, Phys. Rev. Lett **93**, 150501 (2004).

[54] D. D. Yavuz *et al.*, Phys. Rev. Lett. **96**, 063001 (2006).

[55] M. P. A. Jones *et al.*, Phys. Rev. A **75**, 040301 (2007).

[56] P. N. Melentiev, Laser Phys. **15**, 1617 (2005).

[57] M. Bashkansky *et al.*, Phys. Rev. A **72**, 033819 (2005).

[58] Y.-F. Chen, Z.-H. Tsai, Y.-C. Liu, and I. A. Yu, Opt. Lett. **30**, 3207 (2005).

[59] E. Figueroa, F. Vewinger, J. Appel, and A. I. Lvovsky, Opt. Lett. **31**, 2625 (2006).

[60] A. Krishna, K. Pandey, A. Wasan, and V. Natarajan, EPL (Europhysics Letters) **72**, 221 (2005).

[61] F. B. J. Buchkremer, R. Dumke, C. Buggle, G. Birkl, and W. Ertmer, Rev. Sci. Instrum. **71**, 3306 (2000).

[62] A. S. Arnold, J. S. Wilson, and M. G. Boshier, Rev. Sci. Instrum. **69**, 1236 (1998).

[63] C. J. Hawthorn, K. P. Weber, and R. E. Scholten, Rev. Sci. Instrum. **72**, 4477 (2001).

[64] R. A. Nyman *et al.*, Rev. Sci. Instrum. **77**, 033105 (2006).

[65] D. Voight, Appl. Phys. B **B72**, 279 (2001).

[66] N. A. Proite, B. E. Unks, J. T. Green, and D. D. Yavuz, Phys. Rev. Lett. **101**, 147401 (2008).

[67] N. A. Proite, B. E. Unks, J. T. Green, and D. D. Yavuz, Phys. Rev. A **77**, 023819 (2008).

[68] S. E. Harris and A. V. Sokolov, Phys. Rev. Lett. **81**, 2894 (1998).

[69] D. A. Steck, Los Alamos National Laboratory Technical Report, 2001 (unpublished) .

[70] D. D. Yavuz and N. A. Proite, Phys. Rev. A **76**, 041802 (2007).

[71] F. Le Kien, G. Rempe, W. P. Schleich, and M. S. Zubairy, Phys. Rev. A **56**, 2972 (1997).

[72] S. Qamar, S.-Y. Zhu, and M. S. Zubairy, Phys. Rev. A **61**, 063806 (2000).

[73] M. Sahrai, H. Tajalli, K. T. Kapale, and M. S. Zubairy, Phys. Rev. A **72**, 013820 (2005).

[74] E. Paspalakis and P. L. Knight, Phys. Rev. A **63**, 065802 (2001).

[75] J. Xu and X. Hu, J. Phys. B: At. Mol. Opt. Phys. **40**, 1451 (2007).

[76] G. S. Agarwal and K. T. Kapale, J. Phys. B: At. Mol. Opt. Phys. **39**, 3437 (2006).

[77] S. W. Hell and J. Wichmann, Opt. Lett. **19**, 780 (1994).

[78] A. V. Gorshkov, L. Jiang, M. Greiner, P. Zoller, and M. D. Lukin, Phys. Rev. Lett. **100**, 093005 (2008).

[79] S. W. Hell, Science **316**, 1153 (2007).

[80] P. C. Maurer *et al.*, Nat. Phys. advanced online publication (2010).

[81] B. Richards and E. Wolf, Proc. R. Soc. London, Ser. A **253**, 358 (1959).

[82] L. Isenhower, W. Williams, A. Dally, and M. Saffman, Opt. Lett. **34**, 1159 (2009).

[83] J. Arlt and M. J. Padgett, Opt. Lett. **25**, 191 (2000).

[84] S. E. Harris and Z.-F. Luo, Phys. Rev. A **52**, R928 (1995).

[85] K. Bergmann, H. Theuer, and B. W. Shore, Rev. Mod. Phys. **70**, 1003 (1998).

[86] R. Newell, J. Sebby, and T. G. Walker, Opt. Lett. **28**, 1266 (2003).

[87] V. Sandoghdar, C. I. Sukenik, E. A. Hinds, and S. Haroche, Phys. Rev. Lett. **68**, 3432 (1992).

[88] J. D. Perreault and A. D. Cronin, Phys. Rev. Lett. **95**, 133201 (2005).

[89] A. O. Caride, G. L. Klimchitskaya, V. M. Mostepanenko, and S. I. Zanette, Phys. Rev. A **71**, 042901 (2005).

[90] K. P. Nayak *et. al.*, arxiv:quant-ph/0610136 (2006).

[91] K. S. Johnson *et al.*, Science **280**, 1583 (1998).

[92] N. A. Proite, Z. J. Simmons, and D. D. Yavuz, arXiv:1011.2754v1 [physics.atom-ph] .

[93] H. Li *et al.*, Phys. Rev. A **78**, 013803 (2008).

[94] D. A. Braje, V. Balić, G. Y. Yin, and S. E. Harris, Phys. Rev. A **68**, 041801 (2003).

[95] E. Urban *et al.*, Nat. Phys. **5**, 110 (2009).

[96] A. Gaetan *et al.*, Nat. Phys. **5**, 115 (2009).

[97] N. A. Proite and D. D. Yavuz, Opt. Comm. **282**, 3275 (2009).

[98] R. W. Boyd, *Nonlinear Optics*, 3 ed. (Academic Press, 2008).

[99] G. S. He and S. H. Liu, *Physics of Nonlinear Optics* (World Scientific, 1999).

[100] S. E. Harris and Y. Yamamoto, Phys. Rev. Lett. **81**, 3611 (1998).

[101] S. E. Harris and L. V. Hau, Phys. Rev. Lett. **82**, 4611 (1999).

[102] M. D. Lukin and A. Imamoğlu, Phys. Rev. Lett. **84**, 1419 (2000).

[103] H. Wang, D. Goorskey, and M. Xiao, Phys. Rev. Lett. **87**, 073601 (2001).

[104] C. Ottaviani, D. Vitali, M. Artoni, F. Cataliotti, and P. Tombesi, Phys. Rev. Lett. **90**, 197902 (2003).

[105] D. A. Braje, V. Balić, G. Y. Yin, and S. E. Harris, Phys. Rev. A **68**, 041801 (2003).

[106] A. M. C. Dawes, L. Illing, S. M. Clark, and D. J. Gauthier, Science **308**, 672 (2005).

[107] A. D. Slepkov, A. R. Bhagwat, V. Venkataraman, P. Londero, and A. L. Gaeta, Opt. Express **16**, 18976 (2008).

[108] D. D. Yavuz and D. E. Sikes, Phys. Rev. A **81**, 035804 (2010).

[109] D. E. Sikes and D. D. Yavuz, Phys. Rev. A **82**, 011806 (2010).

[110] J. W. Henry, Master's Thesis (2009).

[111] D. Sikes and D. Yavuz, Optics Communications **283**, 556 (2010).

[112] D. D. Yavuz and N. A. Proite, Phys. Rev. A **78**, 053811 (2008).

[113] M. A. Rosenberry, J. P. Reyes, D. Tupa, and T. J. Gay, Phys. Rev. A **75**, 023401 (2007).

[114] M. V. Romalis, E. Miron, and G. D. Cates, Phys. Rev. A **56**, 4569 (1997).

[115] H. Metcalf and P. van der Straten, *Laser Cooling and Trapping* (Springer, York, PA, 1999).

[116] J. Gea-Banacloche, Optics Communications **283**, 719 (2010).

[117] J. Gea-Banacloche, Phys. Rev. A **81**, 043823 (2010).